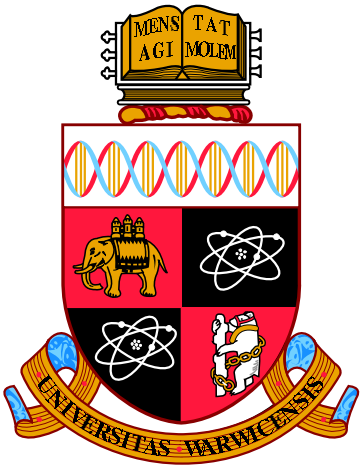

Functionalities at Ferroic Domain Walls

by

Alan Edward Brunier

Thesis

Submitted to the University of Warwick

for the degree of

Doctor of Philosophy

Department of Physics

August 2019

WARWICK
THE UNIVERSITY OF WARWICK

Contents

List of Figures

Declarations

I declare that this thesis contains an account of my research work carried out at the Department of Physics, University of Warwick, between October 2015 and August 2019 under the supervision of Prof. Marin Alexe. The research reported here has not been previously submitted, wholly or in part, at this or any other academic institution for admission to a higher degree.

All the work presented here was completed by myself, with the exception of:

- The sample growth of the $PbZr_{0.2}Ti_{0.8}O_3/SrRuO_3/SrTiO_3$ thin films studied in Chapter 4. These were prepared in the group of Prof. Marin Alexe at the Max Planck Insitute of Microstructure Physics, Germany.
- The synchrotron measurements of the $BaTiO_3$ thin film for which data is presented in Chapter 7. These were acquired by and analysed in collaboration with Matthias Rössle (Universität Potsdam and Helmholtz-Zentrum Berlin).

The following work was carried out in collaboration with other researchers:

- The dielectric measurements and analysis presented in Chapter 5 were carried out in collaboration with Caroline Borderon, Hartmut Gundel, Raphaël Renoud and Kevin Nadaud (Université de Nantes, France).
- The synchrotron measurements presented in Chapters 6 and 7 were acquired in collaboration with Christelle Kwamen, Matthias Rössle, Mathias Bargheer and Wolfram Leitenberger (Universität Potsdam and Helmholtz-Zentrum Berlin). Analysis was carried out in collaboration with Matthias Rössle.

- The transmission electron microscopy measurements presented in Chapter 8 were acquired by Jonathan Peters (University of Warwick). Analysis was carried out in collaboration with Jonathan Peters.
- Photoelectric measurements presented in Chapter 8 were acquired in collaboration with Affan Iqbal (University of Warwick).

The majority of the experimental data presented in Chapter 4 of this thesis has been published in C. Borderon, A. E. Brunier, K. Nadaud, R. Raphaël, M. Alexe and H. W. Gundel, *Scientific Reports* **7**, 3444 (2017) under the title "Domain wall motion in $Pb(Zr_{0.20}Ti_{0.80})O_3$ epitaxial thin films".

The following manuscripts consist of data presented in this thesis and are currently in preparation.

- Alan E. Brunier and Marin Alexe, "Electrical functionality of domain walls in $BiFeO_3$ capacitor devices".
- Alan E. Brunier, Christelle Kwamen, Matthias Rössle, Wolfram Leitenberger, Mathias Bargheer and Marin Alexe, "Time resolved ferroelectric switching in $BiFeO_3$".
- Alan E. Brunier, Jonathan J. P. Peters, Affan Iqbal and Ana M. Sanchez Marin Alexe, "Structural and photoelectric properties of tensile strained $BiFeO_3$".

Over this time period I have also had the chance to contribute to other scientific works, a number of which are currently being prepared for publication. These are

- Nicole Bein, Pamela Machado, Mariona Coll, Maja Makarovic, Tadej Rojac, Alan Brunier, Marin Alexe, Feng Chen, Heidemarie Schmidt and Andreas Klein, "The Fermi energy in $BiFeO_3$".
- Wen Dong, Fan Tian, Jolyon Aarons, Dequan Jiang, Qiushuo Sun, Samuel D. Seddon, Nicholas D. M. Hine, Zhengcai Xia, Alan E. Brunier, Emma Pickwell-MacPherson and Qiuyun Fu, "Defect induced dielectric and magnetic properties in doped metal oxides".

- Wen Dong, Jonathan J. P. Peters, Dorin Rusu, Daniela Emilia Dogaru, Michael Staniforth, Alan E. Brunier, James Lloyd-Hughes, Ana M. Sanchez and Marin Alexe, "Interfacial coupling in BFO/LSMO superlattices".

Acknowledgments

The present thesis would not have been possible without the help of many people who were involved, directly and indirectly, in this work. Here I would like to acknowledge all the support and encouragement I received from these people and also wish them success in their future endeavours.

First I would like to thank my supervisor Prof. Marin Alexe for offering me the opportunity to undertake a PhD in his research group and introducing me to the field of oxide electronics. I am especially grateful for the number of opportunities I have had to collaborate with other researchers, both within the University of Warwick and internationally. Over the course of my PhD I have grown both as a scientist and personally, and Prof. Alexe has played an instrumental role in this. The skills I have acquired and lessons I have learned will no doubt serve me well in my future career.

It is desirable when working in a research group for there to be a positive and proactive atmosphere. During my PhD I consider myself privileged to have worked alongside Dr. Akash Bhatnagar, Dr. Dong-Jik Kim, Dr. Geanina Apachitei, Dr. Mingmin Yang, Dr. Jonathan Peters, Dr. Wen (Albert) Dong, Dr. Yooun Heo, Daniela Dogaru, Dorin Rusu, Samuel Seddon, Hangbo Zhang, Affan Iqbal and Mike Crosbie.

I am particularly grateful to a number of staff at Warwick who allowed me the opportunity to undertake experimental work in their labs and assisted me where needed, especially Dr. Mark Crouch and Corinne Maltby (cleanroom facility), Dr. David Walker and Dr. Steven Huband (x-ray facility), Steve York and Steven Hindmarsh (electron microscopy facility), Dr. Martin Lees (low temperature

magnetic characterisation lab), Dr. Susan Burrows (powder processing lab) and Dr. James Lloyd-Hughes and Dr. Mick Staniforth (ultrafast optics lab). I am also grateful to Dr. Michele Failla, Dr. Akash Bhatnagar, Dr. Mingmin Yang and Dr. Jonathan Peters who helped provide me with training and supported me in my early work in some of these facilities.

I would also like to acknowledge support from various technical and administrative staff, in particular Mike Crosbie (group technician), Jeanette Chattaway (mechanical workshop), Bob Day (electrical workshop), David Greenshields (electrical workshop) and Dr. Tung Fai Yu (electrical workshop), Rosalind Johnstone (administrative) and Susan Tatlock (administrative).

I will forever be grateful to the research groups of Prof. Matias Bargheer (University of Potsdam and Helmholtz-Zentrum Berlin, Germany) and Prof. Hartmut Gundel (Université de Nantes, France) for welcoming me into their research groups on the occasions I visited. In particular I would like to thank Dr. Christelle Kwamen, Dr. Matthias Rössle, Dr. Wolfram Leitenberger, Dr. Caroline Borderon and Dr. Kevin Nadaud for my time visiting their groups pleasant as well as productive.

Throughout my time at the University of Warwick I consider myself privileged to have been surrounded by a circle of friends (both within and beyond the university) who consistently supported me when I needed it and provided welcome distractions throughout. I am particularly grateful to Samuel Gower and Dr. Oliver Vavasour, my housemates in the latter stages of my PhD, for their support and assistance in that crucial time.

Last, but definitely not least, I would like to express my love and gratitude to my family. They always have been, and will always be, a pillar of support and source of inspiration in my life.

Abstract

Over the last decade domain walls in ferroelectric and multiferroic materials have attracted significant research interest. This has been driven by the discovery that these interfaces can exhibit exotic functional properties, including but not limited to enhanced electrical conductivity, and has been enabled by the development of advanced experimental characterisation techniques including atomic-resolution transmission electron microscopy and polarisation-sensitive atomic force microscopy methods which enable the polarisation at these nanoscale interfaces to be effectively probed. Much of the early work focussed on determining the fundamental physical properties of domain walls, but now more research is being directed towards engineering useful devices where the domain walls are the active element. The recent demonstration that it is possible to manufacture prototype ferroelectric domain wall memory devices which are compatible with the requirements of industry has only furthered this.

The objective of this thesis is to further understanding of the properties of domain walls, most often directly using a device geometry, with the aim of obtaining information that can be used to engineer future novel devices. The materials studied here, multiferroic $BiFeO_3$ and ferroelectrics $PbZr_{0.2}Ti_{0.8}O_3$ and $BaTiO_3$, are among those that have attracted most research interest due to having properties which are especially attractive from the perspective of device engineering.

First the domain wall motion in $Pt/PbZr_{0.2}Ti_{0.8}O_3/SrRuO_3/SrTiO_3$ thin films is studied using piezoelectric force microscopy to probe nanoscale domain structure and an advanced low-field dielectric spectroscopy method to probe the bulk behaviour of capacitor devices. It has been demonstrated that this combined approach allows information about the mechanisms and energetics of the domain wall motion to be obtained. Values of these quantities for $PbZr_{0.2}Ti_{0.8}O_3$ are presented.

Next the evolution of the domain pattern and domain wall architecture in $BiFeO_3/SrRuO_3/DyScO_3$ capacitor devices during ferroelectric switching was studied. By correlating the composition of domain walls in the device with the low temperature electrical behaviour of the device it was possible to determine that the low temperature conductivity of 109° walls is higher than 71° domain walls. The effective resistivity of each type of domain wall was determined. This is the first report of through-electrode piezoelectric force microscopy being used to gain accurate information about the in-plane polarisation in capacitor devices, and demonstrates that this type of investigation offers a way to carry out electrical and magnetotransport characterisation of conductive nanoscale domain walls in systems which are too insulating to measure at low temperature with scanning probe microscopy or in-plane device geometries. Further than this, the findings in this work elucidate many observations which are already reported in the literature.

Following this, a time-resolved study of the electric field driven ferroelectric

switching in $(001)_{pc}$ oriented $BiFeO_3$ is presented. The process of ferroelectric switching was found to consist of two steps. First the polarisation rotates in-plane and is suppressed, before being flipped to its new orientation. This is a more complicated picture than the previous studies of switching in $BiFeO_3$ have predicted. Furthermore, it was shown that slow processes like the creep motion of domain walls and the collective motion of the extended oxygen octahedral structures have a key role in mediating the timescale of the switching process. These factors are highly dependent on the strain imposed on the ferroelectric $BiFeO_3$ layer by the substrate.

By similar time-resolved synchrotron methods it was found that it is possible to enhance the process of polarisation reversal in metal-ferroelectric-metal by generating an ultrashort compressive strain wave which propagates through the ferroelectric layer during ferroelectric switching. The compressive strain wave is launched by illuminating a conductive oxide electrode layer with an ultrashort infrared laser pulse. Improving the timescale of ferroelectric switching is an attractive goal for researchers who work to design devices for applications which require fast data processing. This method is demonstrated to be a possible method by which one can break the speed limit that domain wall velocity imposes on the ferroelectric switching process. This effect is showcased in both $BiFeO_3$ and $BaTiO_3$ capacitor devices.

Finally a structural investigation of a complex structure in a $BiFeO_3/NdScO_3$ thin film is presented. The structure stabilised here is unlike anything which has been reported for this system before, and is consistent with what can reasonably be expected near the predicted tensile strain-induced phase boundary in $BiFeO_3$. Detailed structural measurements by x-ray diffraction and transmission electron microscopy reveal that despite being dominated by the expected M_B phase (with mainly 109° stripe domains), the sample includes many regions where the polarisation has a significantly larger than expected in-plane component. This indicates the presence of an orthorhombic or orthorhombic-like phase. Even within domains there is a clear polarisation instability. Temperature dependant measurements of the photovoltaic effect in this sample show a behaviour which is different from that of phase pure and essentially unstrained 109° stripe domain $BiFeO_3$ stripe domain films and also predicts that a phase transition to a from a mixed phase to a single phase structure occurs at around 200 K.

"*God made solids, but surfaces were the work of the devil.*"

Wolfgang Pauli, quoted in Growth, Dissolution, and Pattern Formation in Geosystems (1999) by Bjørn Jamtveit and Paul Meakin, p. 291.

Chapter 1

Introduction

Over the last decade domain walls in ferroelectric and multiferroic materials have attracted significant research interest. This has been driven by the discovery that these interfaces can exhibit exotic functional properties [1, 2], including but not limited to enhanced electrical conductivity, and has been enabled by the development of advanced experimental characterisation techniques including atomic-resolution transmission electron microscopy and polarisation-sensitive atomic force microscopy methods which enable the polarisation at these nanoscale interfaces to be effectively probed [3–11]. Much of the early work focussed on determining the fundamental physical properties of domain walls, but now more research is being directed towards engineering useful devices where the domain walls are the active element. The recent demonstration that it is possible to manufacture prototype ferroelectric domain wall memory devices which are compatible with the requirements of industry has only furthered this [12, 13].

The objective of this thesis is to further understanding of the properties of domain walls, most often directly using a device geometry, with the aim of obtaining information that can be used to engineer future novel devices. The materials studied here, multiferroic $BiFeO_3$ and ferroelectrics $PbZr_{0.2}Ti_{0.8}O_3$ and $BaTiO_3$, are among those that have attracted most research interest due to having properties which are especially attractive from the perspective of device engineering.

In Chapter 2 the required background physics and materials used in this work are introduced. Chapter 3 goes on to describe the various experimental methods employed to both measure and fabricate the samples used here.

Chapter 4 details an investigation into the mobility of 90° domain walls in $PbZr_{0.2}Ti_{0.8}O_3/SrRuO_3/SrTiO_3$ epitaxial thin films. The domain wall behaviour was studied by comparing the response two samples with different domain structures to

AC electric field. One sample had a monodomain structure and the other contained both a and c domains, i.e. had a comparably high density of 90° domain walls. A combined investigation using piezoelectric force microscopy to probe the nanoscale structure and an advanced low-field dielectric spectroscopy method was used to probe the behaviour of capacitor devices with Pt top electrodes and quantitative information about the mechanism and energetics of the domain wall motion were obtained.

Chapter 5 details an investigation where the electrical properties of Pt/$BiFeO_3$/$SrRuO_3$/$DyScO_3$ capacitor devices were measured at various temperatures in a variety of switching states. Through-electrode piezoelectric force microscopy was used to directly map the nanoscale domain structure in each switching state, enabling the contribution of domain walls to the electrical measurements to be determined. This work made use of the fact that in capacitors with 2-variant 71° stripe domain $BiFeO_3$ switch in a repeatable manner. This is the first report of through-electrode piezoelectric force microscopy being used to gain accurate information about the in-plane polarisation in capacitor devices and demonstrates that the electrical properties in the system studied here are very much dominated by the 109° domain walls which are formed in the intermediate switching state.

Time-resolved measurements of electric field driven ferroelectric switching in $BiFeO_3$ capacitor devices are presented in Chapter 6. As devices were cycled with an applied voltage pulse sequence, the current response (related to the polarisation switching) was measured using standard electrical methods and the structural response of the ferroelectric layer was sampled with synchrotron x-rays. Electrical and structural data were simultaneously acquired enabling the structural response to be properly analysed at distinct stages of the ferroelectric switching process. Interestingly, it was found that i) unlike in Chapter 5 after electrical cycling the initial domain pattern in the device was erased, ii) that the 71° ferroelectric switching consists of two steps: an in-plane rotation followed by the polarisation flipping, iii) that during switching the magnitude of polarisation was suppressed. Further to this it was found that the piezoelectric response of a film on $SrRuO_3$/$SrTiO_3$ was dominated by creep and motion of the extended oxygen octahedral structure, unlike a similar film on $SrRuO_3$/$DyScO_3$ which does not show either of those slow processes. This indicates that the strain condition has a very significant effect on the polarisation reversal and accompanying domain wall motion.

Chapter 7 contains an investigation into whether it is possible to assist

electric field induced ferroelectric switching in metal-ferroelectric-metal capacitors by applying an ultrafast infrared laser pulse which generates an acoustic strain wave in one of the metallic electrodes that propagates through the ferroelectric layer during polarisation reversal. Improving the switching timescale, which is normally limited by the domain wall velocity, is an attractive goal for researchers who work to improve the device response time. For some applications, like those which require fast data processing, this is an important parameter. Results for both $BiFeO_3$ and $BaTiO_3$ devices are presented. The measurement setup was the same as used in Chapter 6, but with a pulsed infrared laser which could deliver ultrashort pulses added. The timing of applied voltage and laser pulses were synchronised to the the synchrotron enabling accurate time dependent measurements to be made.

In Chapter 8 a complex structure in a $BiFeO_3/NdScO_3$ thin film is studied in detail. This structure is unlike anything which has been reported for this system before and is consistent with what can reasonably be expected near the tensile strain-induced phase boundary in $BiFeO_3$. Detailed structural measurements by x-ray diffraction and transmission electron microscopy reveal that despite the sample being dominated by the expected M_B phase (with mainly 109° stripe domains) there are many regions where the polarisation appears to have a significantly larger than expected in-plane component, indicating an orthorhombic or orthorhombic-like phase. Even within domains there is a clear polarisation instability. Temperature dependant measurements of the photovoltaic effect in this sample show a behaviour which is distinct from that of 109° stripe domain $BiFeO_3$ stripe domain films on essentially unstrained substrates and also predicts a phase transition from a mixed phase to a single phase structure at around 200 K.

Finally, in Chapter 9 the results are summarised and possible future work is discussed.

Chapter 2

Background theory and materials

2.1 Ferroelectric and and multiferroic materials

2.1.1 Dielectrics

The dielectric susceptibility χ_e is a measure of the ability of a material to become polarised when an electric field is applied. It is defined by

$$P = \varepsilon_0 \chi_e E, \tag{2.1}$$

where P and E are electric polarisation and field respectively and ε_0 is the permittivity of free space [14]. It is one of the most basic material properties. Materials with high dielectric constants are needed as gate electrode materials [15–17] and are widely used in capacitors [18]. In contrast, materials with low dielectric constant are needed to insulate conductive components in microelectronic devices [19, 20], and highly field-tunable dielectrics are needed for radio frequency devices [21, 22]. The dielectric susceptibility is related to the relative dielectric constant ε_r by

$$\chi_e = \varepsilon_r - 1. \tag{2.2}$$

The quantity ε_r can equivalently considered a measure of the capacity of a material to store electrical energy compared to that of the vacuum [14]. This energy is stored in the form of dipoles which are induced and aligned by the applied electric field. The quantity ε_r is widely used to describe the polarisability of dielectric and ferroelectric materials in engineering and non-fundamental research as it is both simply defined and not easily confused with magnetic susceptibility. In ferroelectrics ε_r is an order parameter which diverges at phase transitions and is described by a Curie-Weiss law [14, 23].

2.1.2 Piezo-, pyro- and ferroelectrics

Of the thirty two crystallographic point groups twenty one lack an inversion centre, i.e. are non-centrosymmetric. Of these, twenty exhibit direct piezoelectricity; the appearance of electric polarisation caused by the redistribution of charge within the unit cell when a mechanical stress is applied. This effect is reversible and the coupling between the mechanical and electric fields is linear. The piezoelectric effect can be expressed as

$$P_i = d_{ijk} X_{kl} \tag{2.3}$$

where P_i is the induced polarisation, d_{ijk} is a third rank tensor which contains the piezoelectric coefficients and X_{kl} is a second rank tensor for stress [14, 23, 24]. The converse piezoelectric effect describes how an applied field E_k induces a strain ϵ_{ij} and may be expressed as

$$\epsilon_{ij} = d_{ijk} E_k. \tag{2.4}$$

Ten of the piezoelectric crystallographic point groups exhibit a spontaneous polarisation even when no mechanical stress is applied. These are referred to as polar. The origin of electric polarisation is a non-vanishing electric dipole moment at the unit cell level. The pyroelectric effect describes the temperature dependence of this polarisation and may be expressed as as

$$\Delta P_i = p_i \Delta T \tag{2.5}$$

where ΔP_i is the change in polarisation, p_i is the pyroelectric coefficient and ΔT is the temperature change [14, 23, 24].

Materials which exhibit ferroic order are characterised by a spontaneous order parameter that can be reversibly switched between at least two energetically equivalent states through application of an external field. Moreover, the orientational state should exhibit a hysteretic response as it is switched between states. Regions with uniform polarisation orientation are called domains. The interfaces separating domains with different polarisation orientation are called domain walls. Ferroelectric, ferromagnetic and ferroelastic materials are all characterised in this way as shown in Fig. 2.1 [14, 23].

The materials studied in this thesis are ferroelectric. In this case the order parameter is electric polarisation. Ferroelectrics are a subclass of pyroelectric and piezoelectric materials. Most ferroelectric materials exist in a paraelectric, generally centrosymmetric, phase at high temperature. This high symmetry phase exhibits

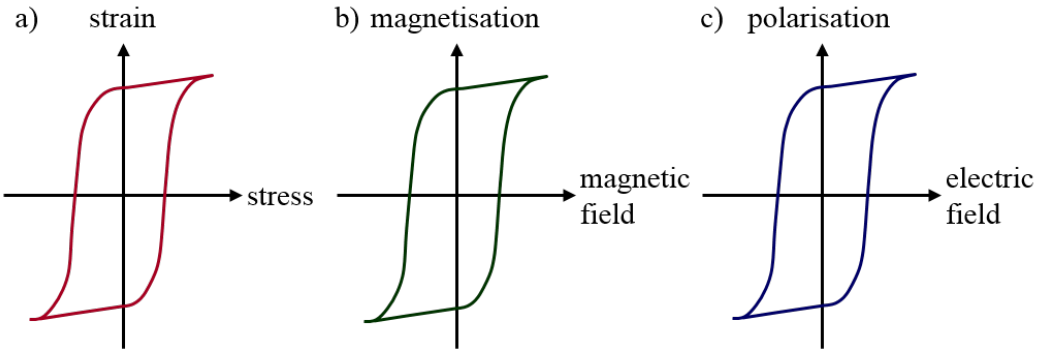

Figure 2.1: Schematic diagram showing the hysteretic behaviour of a) ferroelastic, b) ferromagnetic and c) ferroelectric materials.

a simple dielectric response to applied electric field. As they are cooled below the Curie temperature T_C a structural phase transition occurs which permits the appearance of a spontaneous polarisation as the inversion symmetry is lost [14, 23].

The most well studied and widely used ferroelectric materials are perovskite oxides with of the type ABO_3. A and B are metal cations, and are found at the corners and centre of the pseudocubic perovskite unit cell respectively. The oxygen atoms are located at face centres and form an octahedral cage around the B-site metal cation [23]. Simple examples of materials with this structure include $BaTiO_3$, $PbTiO_3$, $LiNbO_3$, $BiFeO_3$ and $SrTiO_3$. The mechanism responsible for the emergence of ferroelectricity in some of the materials in this family is different in different materials. For example, in some cases such as $BaTiO_3$ the polarisation primarily originates from the displacement of the B-site cation within the octahedral cage but in other materials such as $PbTiO_3$ the displacement of the A-site cations contribute significantly [23]. Fig. 2.2 shows prototypical cubic and tetragonal structures for a simple ferroelectric material where the ferroelectricity originates from the shift of the B-site metal cation below the Curie temperature.

2.1.3 Multiferroics

Multiferroic materials are materials in which more than one type of ferroic order is present. When this is the case these orderings are coupled. For example, in a material which is both ferroelectric and ferromagnetic, the magnetisation can be reversed by application of an electric field via the magnetoelectric effect. Similarly the polarisation can be switched by electric field. This specific effect, magnetoelectric coupling, has generated a large amount of interest in the oxide

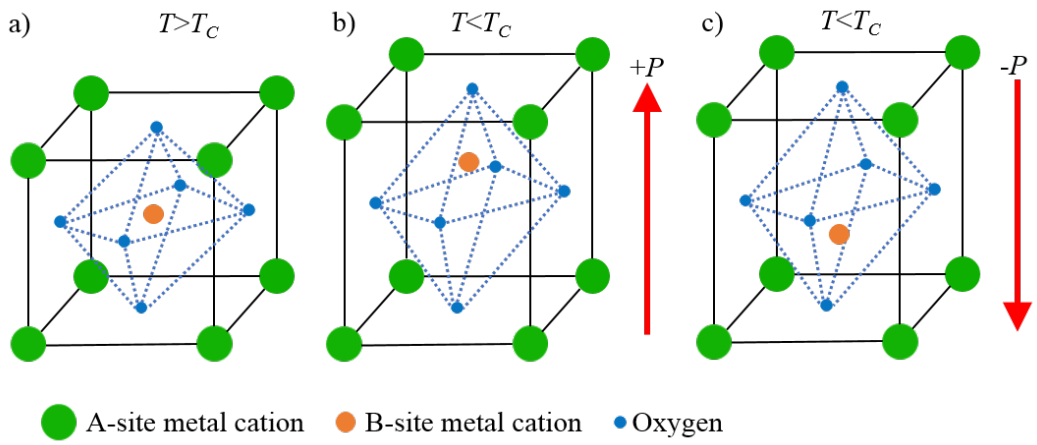

Figure 2.2: Schematic diagram showing a) cubic and b)-c) tetragonal unit cells for a simple ferroelectric material where the origin of the ferroelectricity comes from the shift of the B-site metal cation. Above T_C the structure is centrosymmetric and there is no net polarisation vector. Below T_C this symmetry is broken and two structures with oppositely oriented polarisation P are stable. The solid black lines mark the edges of the unit cell and the blue dotted lines show the structure of the oxygen octahedral cage.

electronics community in recent years [25]. The range of possible couplings between primary order parameters is shown in Fig. 2.3.

Despite this large interest, there are relatively few magnetic ferroelectrics. This is because the "classical" mechanisms for ferroelectric and magnetic order tend to be mutually exclusive in perovskites. Normally in sferroelectric perovskite materials the B site cation has no electrons in the d-shell, but in order for magnetic moments to be present it is necessary to have unpaired d-shell electrons present[26]. The effect of this is that multiferroic materials that avoid this conflict promote more unusual kinds of ferroelectricity. In some cases, this can yield interesting behaviour such as advanced performance and novel functionality located at domain walls or in domains. One result of the shortage of multiferroic materials is the expansion of the definition of the word multiferroic so it includes non-primary order parameters, such as antiferromagnetism or ferrimagnetism. The primary order-paremeters for multiferroic materials are shown in Fig. Fig. 2.3(b). The effect of this is including materials such as $BiFeO_3$ which is ferroelectric and antiferromagnetic.

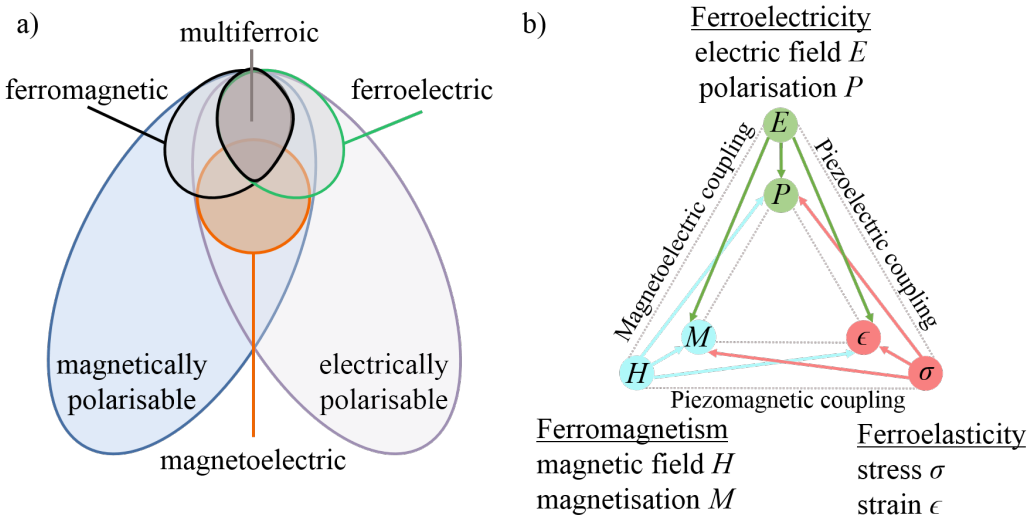

Figure 2.3: a) The relationship between magnetoelectric and multiferroic materials. b) Schematic illustrating different types of coupling present in materials. Much attention has been given to materials where electric and magnetic order is coupled. These materials are known as magnetoelectric materials.

2.2 Bulk and thin film perovskite ferroelectrics

While bulk ferroelectric perovskites have been widely used in piezoelectric transducers and sensors for decades, it is impossible to incorporate them into integrated circuits and micro-electro-mechanical systems (MEMS) due to their large macroscopic dimensions and very large external switching voltages. The development of ferroelectric thin films with nanoscale thickness and low power requirements has provided a pathway for integration of these materials in active devices [27] used in fields including electrocaloric cooling, room temperature magnetic-field detectors, phased-array radar, and three-dimensional trenched capacitors for dynamic random access memories [28]. With modern film growth methods it is possible to deposit high quality epitaxial films, heterostructures, and even superlattices with atomically sharp interfaces and thickness control at the atomic level. The systems that can be engineered using these methods present an excellent opportunity to advance understanding of the fundamental physics governing the behaviour in these systems [29].

It is often most convenient to describe the structure of these materials in terms of the pseudocubic (pc) perovskite unit cell shown in Fig. 2.2. Fig. 2.4 shows the stereographic projections of polarisation for a number of the most current structures along $(001)_{pc}$ and $(111)_{pc}$ viewing directions.

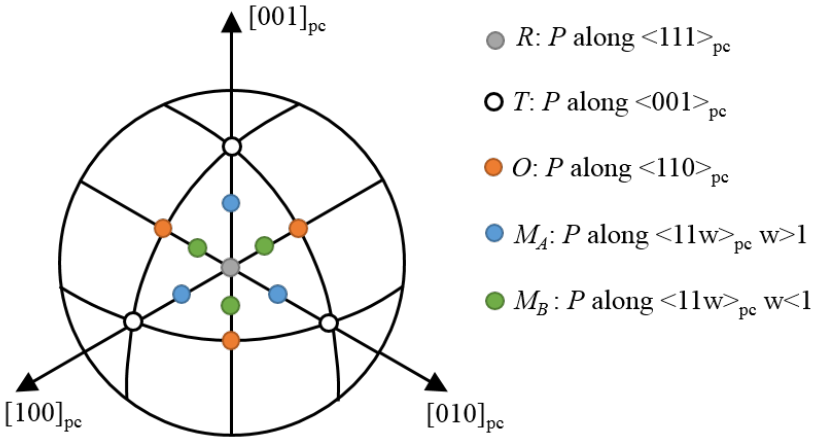

Figure 2.4: Stereographic projection for a perovskite ferroelectric viewed down a $[111]_{pc}$ pseudocubic direction. Polarisation directions for rhombohedral (R), tetragonal (T), orthorhombic (O) and monoclinic bridging phases (M_A and M_B) are shown. Polarisation for monoclinic phases is bound to lie in $\{110\}_{pc}$ mirror planes. For clarity, only the central region of the stereographic projection shown.

2.3 Domain formation and domain walls

One of the properties all ferroic materials have is the ability to form domains. Domain formation in ferroelectrics is driven by the system trying to minimise the electrostatic energy. Two competing energies determine whether a domain wall is formed: the energy gain for the system by formation of the domain and the energy cost of forming a domain wall. Domain walls are formed when the latter energy is smaller than the former [2, 30, 31]. By their very definition, domain walls are the interfaces between regions where the order parameter is different. The result of this symmetry breaking is that at domain walls the properties and structure differ from that of the bulk, opening the possibility for novel functionality to emerge [2]. The field of domain wall nanoelectronics has attracted particular attention due to the opportunity it presents to design electrical devices where domain walls are the active conductive element [2].

2.4 Ferroelectrics

2.4.1 Pb(Zr,Ti)O_3

Lead zirconate titanate, Pb(Zr,Ti)O_3 (PZT), was first developed in the 1950s at the Tokyo Institute of Technology and since then has attracted considerable

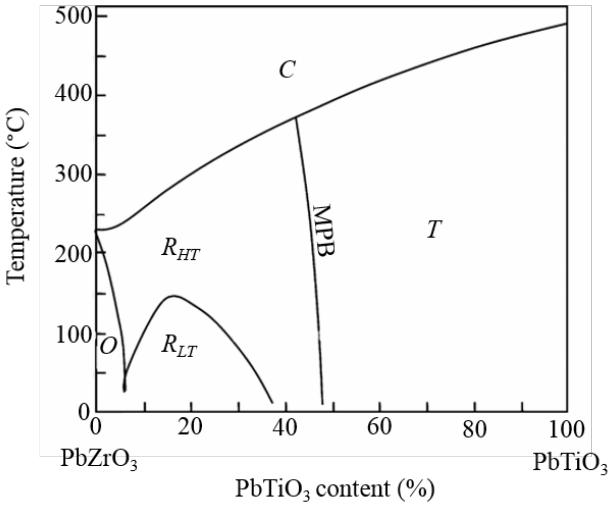

Figure 2.5: Compositional phase diagram of Pb(Zr,Ti)O_3 adapted from Ref. [34]. A number of phases are present, including the paraelectric cubic phase (C) and the ferroelectric tetragonal T, orthorhombic O and low and high temperature rhombohedral phases (R_{LT} and R_{HT}). The morphotropic phase boundary is labelled MPB.

attention due to its attractive properties. These properties include physical strength, chemical stability, tailorability, relatively inexpensive manufacture costs, robust ferroelectric and high temperature behaviour. It is one of the most used piezoelectric materials in industry [32, 33].

The compositional phase diagram for Pb(Zr,Ti)O_3 is shown in Fig. 2.5. At high temperatures Pb(Zr,Ti)O_3 has a cubic structure, but below T_C the structure it adopts depends on the temperature and chemical composition. Ti-rich compositions form a tetragonal ferroelectric phase, whereas Zr-rich compositions form a rhombohedral phase. Despite the end member $PbTiO_3$ having the largest value of electric polarisation, other properties such as the dielectric constant, electromechanical coupling constants and piezoelectric coefficients vary across the phase diagram and are actually maximised at the boundary between tetragonal and rhombohedral phases. At this compositional boundary near $PbZr_{0.48}Ti_{0.52}O_3$ there is a region of structural instability where the dielectric constant, electromechanical coupling constants and piezoelectric coefficients are large and relatively insensitive to temperature. This region of the phase diagram is called the morphotropic phase boundary [35, 36].

In the tetragonal phase the polarisation axes lie along the three possible $<001>_{pc}$ directions, i.e. connecting opposite face centres in the pseudocubic

perovskite unit cell. Therefore there are six allowed polarisation directions. The angle between polarisation vectors in neighbouring domains is constrained by the system geometry to be either 90° or 180°. The 180° domain walls are ferroelectric and not ferroelastic as the polarisation orientation each side of the wall is along the same axis. In contrast, 90° walls are ferroelastic as a strain is introduced as the polarisation vectors each side of the boundary do not lie along the same polar axis [23].

2.4.2 $BaTiO_3$

Barium titanate, $BaTiO_3$ (BTO), was discovered in the Second World War by independent teams based in Germany, Japan and the USA who were searching for new dielectrics for use in capacitors. This was driven by a shortage of mica, the most widely used dielectric at the time. It was initially found by doping TiO_2 with BaO and was found to have a relative permittivity of around 1000, an order of magnitude larger than any other material known at that time. It was the first perovskite ferroelectric discovered and even today it is used in a wide range of components, including multilayer ceramic capacitors, positive temperature coefficient thermistors, and various electro-optic devices. It is the most widely used ferroelectric material [37].

At room temperature bulk $BaTiO_3$ has a tetragonal structure with lattice constants $a = 3.9939$ Å and $c = 4.0343$ Å [38], and remnant polarisation $P_r = 27$ $\mu C/cm^2$ [39]. Above the Curie temperature of 120 °C $BaTiO_3$ has a cubic structure, but on cooling has three ferroelectric transitions: cubic to tetragonal at 120 °C, tetragonal to orthorhombic at 5 °C, and orthorhombic to rhombohedral at -90 °C [23]. These structures are shown in Fig. 2.6.

Its main advantage is that it is lead-free and therefore more environmentally friendly than $Pb(Zr,Ti)O_3$, however the comparably low Curie temperature of the bulk structure limits the operational temperature range of ceramic and single crystal $BaTiO_3$ based devices. It is of note that in 2004, Choi et al. demonstrated that just one percent of compressive strain in $BaTiO_3$ thin films can simultaneously enhance the ferroelectric polarisation and increase the Curie temperature by several hundred degrees [39]. This makes $BaTiO_3$ thin films a promising candidate for replacement of lead-based ferroelectric materials in several high temperature applications.

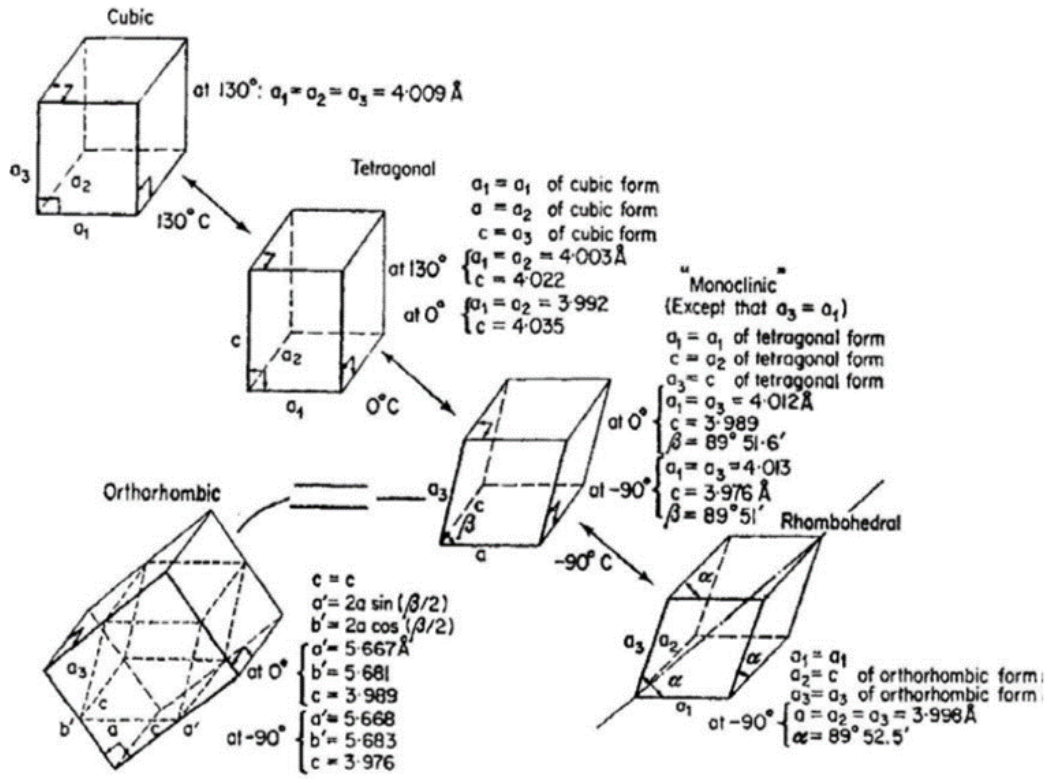

Figure 2.6: The different crystallographic structures of $BaTiO_3$. Figure from Ref. [40].

2.4.3 $BiFeO_3$

Bismuth ferrite, $BiFeO_3$ (BFO), is one of the few single phase room temperature multiferroic materials. It is a rhombohedrally distorted perovskite which exhibits antiferromagnetism and ferroelectricity. For this reason, along with its large ferroelectric polarisation and lead-free composition, it has been extensively studied over recent years and significant advances have been made towards understanding its ferroelectricity, magnetism, and the coupling between these order parameters in both bulk and single crystal forms.

The room temperature structure consists of two distorted perovskite blocks connected along their body diagonal, building a rhombohedral unit cell [41]. This state is stabilised due to hybridisation between the the lone pair of electrons in the Bi 6s shell with the the O^{2-} p orbitals. The result of this hybridisation is that the Bi^{3+} ion is driven to the off-centre position. This is the cause of most of the ferroelectricity in $BiFeO_3$ [26, 42]. The Fe^{3+} ions is also displaced, but that displacement is approximately four times less than that of the Bi^{3+}. Further to this the two oxygen octahedra, connected along the body diagonal direction, are rotated clockwise and anticlockwise by $\pm 13.8^\circ$ about the body diagonal. To accommodate these displacements the rhombohedral unit cell is slightly distorted with the rhombohedral angle α_{rh} taking a value of 59.348° as opposed to its ideal value of 60° [43, 44]. Due to the similarity of the rhombohedral unit cell of $BiFeO_3$ with the ideal perovskite structure it is possible to describe the structure as pseudocubic (pc) by considering one of the two perovskite blocks that make up the unit cell only. In this description the polarisation is allowed to point along the $<111>_{pc}$ directions, the lattice parameter a_{pc} is 3.965 Å [43]. Rhombohedral and pseudocubic representations of the structure of $BiFeO_3$ are shown in Fig. 2.7. For the rest of this thesis unless otherwise stated the pseudo-cubic description of the lattice is used.

$BiFeO_3$ has a large ferroelectric polarisation of around 90-100 $\mu C/cm^2$ and a Curie temperature of 830 °C. It also a G-type antiferromagnet and has a Néel temperature of 370 °C. In this antiferromagnetic structure each Fe^{3+} spin is surrounded by six other anti-parallel spins. In reality the spins are not perfectly anti-parallel but are slightly canted due to lack of inversion symmetry. These canted spins result in a net magnetic moment, however this is cancelled out due to a cycloid-like rotation of the canted spins which propagates along a $<110>_{pc}$ direction.

In rhombohedral ferroelectrics the polarisation lies along the $<111>_{pc}$ directions, meaning that eight polarisation directions are allowed. The possible

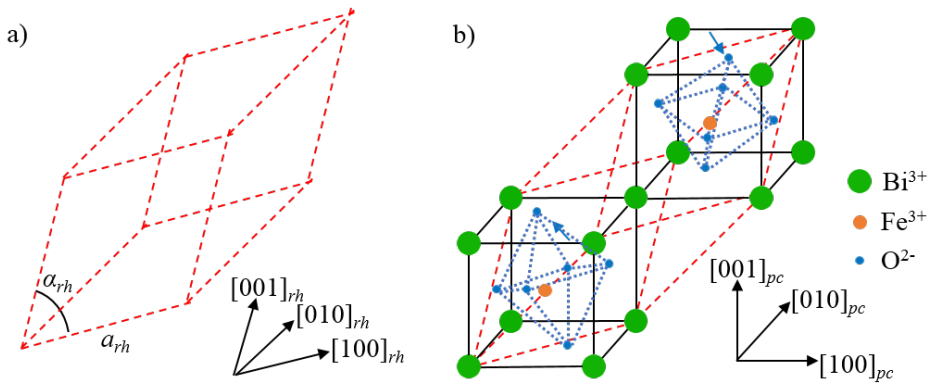

Figure 2.7: a) The rhombohedral unit cell of $BiFeO_3$. b) The rhombohedral unit cell of $BiFeO_3$ superimposed over two of its pseudocubic unit cells which are connected along the body diagonal. The blue arrows indicate the oppositely oriented distortion of the oxygen octahedra. Ionic shifts of the metal cations ions are shown.

angles between these are 71°, 109° and 180° [31]. The 71° and 109° domain walls are both ferroelectric and ferroelastic whereas 180° domain walls are purely ferroelectric. Fig. 2.8 shows this schematically. In the case of rhombohedrally distorted $BiFeO_3$ films on a cubic substrate, there are four possible ferroelastic variants r_i. For each of these there are two possible ferroelectric states $P_i^{\pm}$ with the $+$ denoting the polarisation points away from the substrate and the $-$ denoting it points towards the substrate [31].

Through strain engineering and control of electrostatic boundary conditions it is possible to create periodic domain structures in $BiFeO_3$ thin films. These structures provide an ideal system in which to study domain wall behaviour. Schematic diagrams of 71° and 109° domain walls are shown in Fig. 2.8.

2.5 Substrate materials

2.5.1 $SrTiO_3$

Strontium titanate, $SrTiO_3$ (STO), is widely used as a substrate material for perovskite oxide thin films due to its wide availability and the quality of crystals available [45, 46]. At room temperature is has a cubic structure and has a lattice parameter of 3.905 Å [47]. At low temperatures it approaches a ferroelectric phase transition but remains paraelectric as a result of quantum fluctuations [48].

In order to grow high quality epitaxial thin films it is common to use crystals which are polished with a slight miscut. The effect of this is to make it

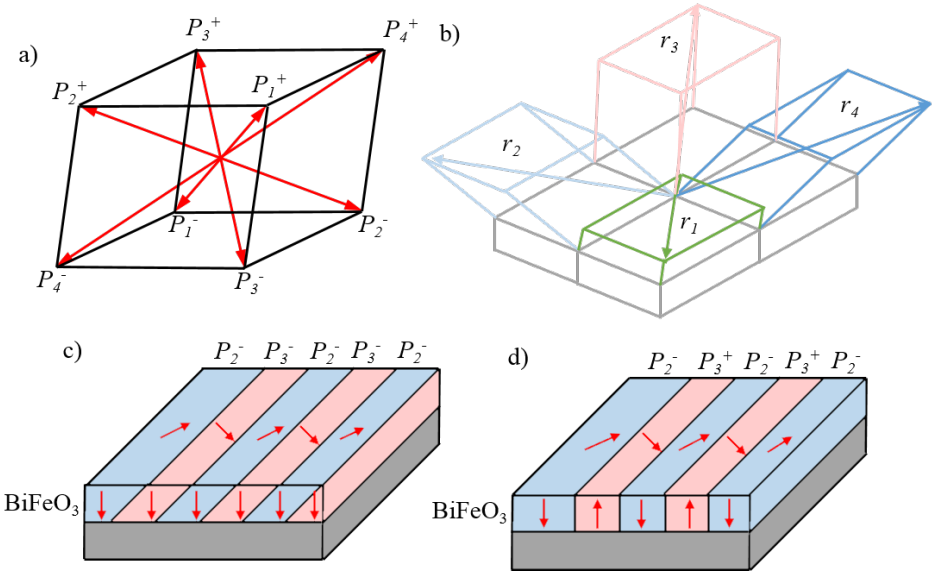

Figure 2.8: a) The eight polar orientations along the four polar axes in the pseudocubic unit cell of $BiFeO_3$. b) The four possible ferroelastic variants of $BiFeO_3$ (coloured) on a square mesh (grey). These are associated with the four polar axes. c) and d) Schematic diagrams showing 71° and 109° stripe domain patterns in a $BiFeO_3$ layer. The out-of-plane component of polarisation in each domain is shown in the cross section and in-plane component is shown on the top surface of the $BiFeO_3$ layer. The polarisation orientations of each domain and all ferroelastic distortions lie along the polar axes, i.e. the $<111>_{pc}$ directions.

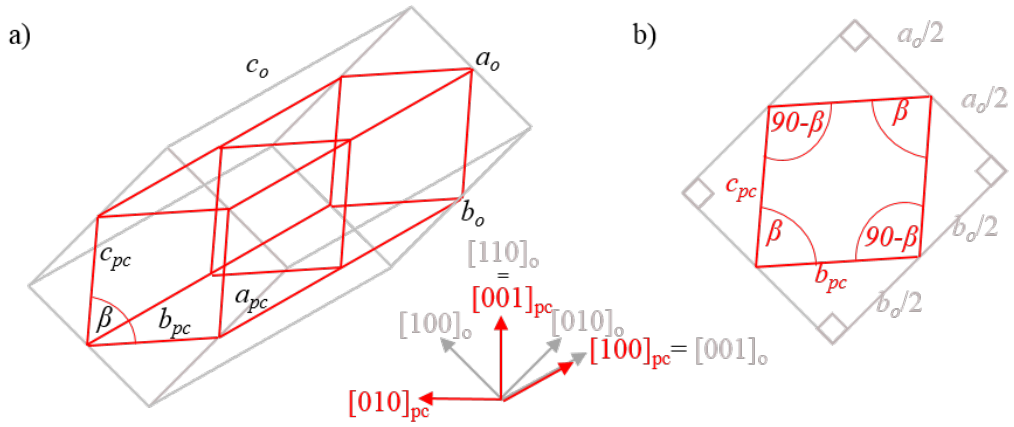

Figure 2.9: Schematic diagrams showing the orthorhombic (grey) $RE ScO_3$ unit cell and two of the four $(001)_{pc}$ oriented perovskite pseudocubes it can accommodate on its $(110)_o$ surface. a) shows the three-dimensional schematic and b) shows the projection of the unit cell along the $[001]_o$=$[100]_{pc}$ direction. Perovskite pseudocubes are monoclinically distorted by angle β in the $[010]_{pc}$ direction due to the difference in the a and b parameters of the orthorhombic unit cell.

possible to, through chemical or/and thermal treatment, reconstruct the surface so it exhibits a terraced structure with step heights of exactly one unit cell. This growth surface makes step-flow growth, a type of layer-by-layer growth, accessible given appropriate deposition conditions for a layer being deposited. Without this treatment island growth which is governed by nucleation on the substrate surface at arbitrary positions instead of step edges is typically expected to dominate. A number of treatments have been developed in order to realise these single terminated step terraces structures on miscut crystals [45, 49]. These are discussed in Chapter 3.

2.5.2 $DyScO_3$ and $NdScO_3$

Rare earth scandate, $RE ScO_3$ (RE=Nd-Dy), single crystals have a more complicated structure than $SrTiO_3$ but offer the advantage that the pseudocubic lattice parameters can be essentially selected as any value between 3.95 and 4.02 Åby simply choosing an appropriate RE element or combination of RE elements [50]. These materials are orthorhombic, insulating, have no phase transitions between 4 K and 300 K, and have thermal expansion coefficients similar to those of many commonly studied perovskite oxide materials. The structure is isomorphic to that of $GdFeO_3$ [51] and the $(110)_o$ surface of these crystals provides a rectangular mesh on which four pseudocubic unit cells of a $(001)_c$ oriented material can be accommodated. This is shown schematically in Fig. 2.9. The orthorhombic $[110]_o$

direction is equivalent to the $[001]_c$ direction. It is of note that the four pseudocubes accommodated on the orthorhombic unit cell are distorted from the ideal cubic perovskite unit cell by a monoclinic distortion which originates from the difference in the lengths of the orthorhombic lattice parameters a_o and b_o. Further to this, the in-plane pseudocubic lattice parameters also differ. From the schematics shown in Fig. 2.9 it is clear that it is possible to relate the pseudocubic lattice parameters and monoclinic distortion to the orthorhombic lattice parameters through

$$a_{pc} = \frac{c_o}{2}, \tag{2.6}$$

$$b_{pc} = c_{pc} = \sqrt{\left(\frac{a_o}{2}\right)^2 + \left(\frac{b_o}{2}\right)^2}, \tag{2.7}$$

$$\beta = 180^\circ - 2\text{arctan}\left(\frac{b_o}{a_o}\right). \tag{2.8}$$

The pseudocubic parameters of $DyScO_3$ (DSO) is especially well matched to that of $BiFeO_3$. For this case the in-plane lattice mismatch, defined as

$$m = \frac{a_{substrate} - a_{film}}{a_{substrate}}, \tag{2.9}$$

is around -0.3% [30].

As with $SrTiO_3$, a number of methods have been employed to obtain surfaces with a high quality step terrace structure enabling high quality growth. These are discussed in Chapter 3.

2.6 Electrode materials

The correct electrical description for the metal-ferroelectric-metal capacitor devices studied in this thesis is as two back-to-back Schottky diodes, where the DC leakage current is limited by the Schottky diode that is reverse biased. Even for symmetric device structures, e.g. SRO/PZT/SRO/STO, it is possible to have polarity-dependent electrical behaviour due to the effect of the polarisation on the barrier heights. In this device geometry, the choice of electrode material has a large effect on device characteristics including leakage current, fatigue and imprint [52]. These are key parameters which determine the electrical device characteristics.

2.6.1 $SrRuO_3$

Strontium ruthenate, $SrRuO_3$ (SRO), is one of the most widely used oxide electrodes due to its chemical and structural compatibility with perovskite oxide ferroelectrics and particularly good resistance to fatigue. It is a metallic conductor with a bulk resistivity of $\rho = 2.75 \times 10^{-4}$ Ωcm at room temperature [53]. Above 160 K it is paramagnetic, but below this temperature it orders ferromagnetically [54]. The room temperature lattice parameters are $a_o = 5.532$ Å, $b_o = 5.572$ Å, $c_o = 7.850$ Å and the monoclinic distortion $\beta = 89.6°$. The pseudocubic lattice parameter that corresponds to this is $a_{pc} = 3.926$ Å.

2.6.2 $La_{1-x}Sr_xMnO_3$

Lanthanum strontium manganite, $La_{1-x}Sr_xMnO_3$ (LSMO), can be considered as Sr doped $LaMnO_3$. $LaMnO_3$ is insulating and antiferromagnetic, with all the manganese ions in the Mn^{3+} state. For each La^{3+} ion which is substituted by a Sr^{2+} ion, one Mn^{3+} ion changes its valence state to Mn^{4+} resulting in both electrical conductivity and the emergence of ferromagnetic order [55]. For the composition used in this work, $La_{0.7}Sr_{0.3}MnO_3$, the room temperature resistivity is around $\rho = 8 \times 10^{-4}$ Ωcm [56] and magnetic Curie temperature is 369 K [57]. The bulk structure of LSMO is rhombohedral with lattice parameter a_{rh} =5.471 Å, however it is convenient to consider it as having a pseudocubic lattice parameter $a_{pc} = 3.88$ Å with a monoclinic distortion of 89.8°.

2.6.3 Metallic electrodes

Pt is the most used electrode material in this work. It is paramagnetic and has a room temperature resistivity of $\rho = 1.05 \times 10^{-5}$ Ωcm. It was chosen as it forms a good rectifying contact with all the ferroelectric materials used here and also has fairly good fatigue resistance compared to other metals (breakdown typically around 5×10^6 cycles for the Pt/BFO/SRO/DSO capacitor devices fabricated here). Further to this, due to its relatively large Young's modulus (168 GPa) and the possibility to deposit extremely thin (down to 3 nm) conductive layers which actually conserve the morphology of the surface it is deposited on, it is particularly suitable for through-electrode PFM measurements such as those presented in Chapter 5. It is also convenient that it is chemically unreactive, so no capping layer of another metal such as Au is needed.

For the photovoltaic characterisation Au electrodes were used. Gold is also paramagnetic and has a room temperature resistivity of $\rho = 2.2 \times 10^{-5}$ Ωcm. Unlike

Pt, it can be easily removed chemically using a solution of KI:I_2.

2.6.4 Metal-ferroelectric interfaces

The ferroelectric materials studied here can be considered at a first approximation to be wide-gap semiconductors at room temperature. The reported band gaps for $BaTiO_3$, $BiFeO_3$, and $Pb(Zr,Ti)O_3$ are around 3.2 eV [58], 2.7 eV [59], and 3.2-3.9 eV [60] respectively. Furthermore, at room temperature the conduction in these materials is thermally activated. Thus, a metal-ferroelectric contact is well described as a rectifying (Schottky) contact, and a metal-ferroelectric-metal structure may be regarded as two back-to-back Schottky diodes [61], one of which will be reverse biased irrespective of the polarity of applied voltage [60]. The screening of interface charge by ferroelectric polarisation causes the depletion width of metal-ferroelectric contacts to be smaller than those of similar interfaces where the semiconductor is non-ferroelectric. Typically the depletion width is no more than a few nm, which far less than the thickness of films used in this work [60]. The potential barrier at the metal-ferroelectric interface is the Schottky barrier height. This barrier height directly determines the leakage current, that is, the current that flows through the contact when it is reverse biased. It is non-trivial to model which metals form particularly rectifying Schottky contacts, however it has been observed in measurements on $Pb(Zr,Ti)O_3$ films [52] that:

1. metals with a completely filled d-shell form very good rectifying contacts,
2. metals with a mostly filled d-shell form good rectifying contacts,
3. metals with no or only a few electrons on the d-shell form Ohmic-like contacts, and
4. metals with high electrical conductivity show a lower leakage current.

It is therefore to be expected that similar behaviour should be shown for $BaTiO_3$ and $BiFeO_3$.

2.7 Strain engineering in epitaxial thin films

2.7.1 General discussion

A number of levers can be used to control the strain experienced by an epitaxial thin film. These include:

1. layer thickness. Below a critical thickness epitaxial thin films are coherently strained by the substrate, i.e. the in-plane lattice parameters of the layer and substrate are the same. Above this critical thickness films are able to relax through formation of misfit dislocations. An example of this can be seen in the films used in Chapter 4. There two PZT/SRO/STO thin films of different thickness are considered, one of which is monodomain (below the critical thickness) and the other of which has both a and c domains (above the critical thickness),

2. Misfit strain from the substrate. Using misfit strain it is possible to elastically strain oxide thin films far beyond the point at which they would crack in the bulk. Under such strains, the properties can be dramatically altered. It is possible to use this strain to transform materials that in their unstrained state show no ferroic order into ferroic or even multiferroic materials. One example of this is $EuTiO_3$. In the bulk this material is a relatively boring paraelectric antiferromagnetic insulator, however when deposited on $DyScO_3$ it is transformed into the strongest known ferroelectric ferromagnetic material [62]. Further to this, elastic strain can also be used to enhance the properties of known ferroic materials. Examples of this include the enhancement ferromagnetism in the constrained rhombohedral phase of $BiFeO_3$ on $LaAlO_3$ [63] and enhancement of ferroelectric properties in $BaTiO_3$ [39],

3. growing the film as a composite. Recently it has been found that super-tetragonal $PbTiO_3$ films with giant polarisation can be deposited on $SrTiO_3$ substrates by growing as a composite along with PbO. In these films the c/a ratio can be as high as 1.238 and polarisation is as high as 236.3 $\mu C/cm^{-2}$ [64]. The bulk values from measurements on $PbTiO_3$ single crystals are 1.065 and around 65 $\mu C/cm^{-2}$ respectively [23, 64],

4. biaxial strain from the substrate. By depositing films on substrates which present a growth surface with an anisotropy of the in-plane lattice parameters, for example $(110)_o$ $REScO_3$ substrates, it is possible to reduce the symmetry of a domain pattern from being four-fold to two-fold. For example, when $BiFeO_3$ is deposited on $DyScO_3$, as opposed to $SrTiO_3$, the number of ferroelastic variants that are allowed is two as opposed to four. This causes the resulting well ordered domain pattern to consist of stripes well aligned along one in-plane direction (i.e. two ferroelastic structural variants only) as opposed to bundles of stripes which may run along either in-plane direction, and

5. chemical pressure. By chemical substitution it is possible to tune the structure of materials in addition to (often dramatically) changing the properties. For example, by doping $BiFeO_3$ with La it is possible to turn it from a rhombohedral ferroelectric into an orthorhombic paraelectric [65]. Also, the ratio of Zr:Ti in $Pb(Zr_{1-x},Ti_x)O_3$ has a significant effect on the properties, especially near the morphotropic phase boundary [35, 36].

2.8 Domain wall motion

The large dielectric response of perovskite ferroelectrics has caused them to attract interest for application in capacitors and microelectro-mechanical systems (MEMS) [66]. There are two significant contributions to the large dielectric response in these materials. The first of these is the intrinsic contribution which is the averaged crystallographic response from the ferroelectric domains [67]. The second is the extrinsic contribution which is mainly from the motion of domain walls and phase boundaries. In perovskite ferroelectrics domain walls can be moved by electric fields, mechanical stresses, or combinations of these. Indeed, polarisation switching itself is mediated by domain wall motion. It is significant to note that the extrinsic contributions can be responsible for up to 75% of the dielectric and piezoelectric response of some ferroelectric ceramic devices [68].

As domain walls are driven to move they experience the periodic potential landscape that the lattice provides. Real materials contain defects, which provide deeper potential wells than the ideal periodic potential landscape of the lattice offers, at which domain walls can be pinned. The result of this is that the domain wall motion is hysteretic and nonlinear.

When designing devices for application, in bulk or thin film form, it is valuable to understand and as a result be able to tune the contribution of domain wall motion to the dielectric response of the sample to applied field.

2.9 Domain wall conductivity

One of the founding fathers of the field of domain wall nanoelectronics, Ekhard Salje, inspired a lot of the early work after offering the realisation that domain walls offer extremely thin and topologically-protected percolative paths for charge transport, with the additional functionality that their positioning can be controlled [1]. It is interesting to note that even though multiferroic properties

have been described since 1966 [69] in the last ten years that the research interest in this topic has dramatically increased.

The first experimental evidence for enhanced electrical conductivity at domain walls was in fact from Aird and Salje in 1998 [70], where they reproducibly generated sheet superconductivity on domain walls in Na-doped WO_{3-x}. It is only much more recently, in 2009, that Seidel et al. directly observed the enhanced conductivity of artificially written domain walls in epitaxial thin films of $BiFeO_3$ [3]. This is perhaps the paper which is most responsible for generating research interest. Subsequently in 2011, Chiu et al. showed that enhanced conductivity is found not just at artificially written domain walls but also at as-grown domain walls in $BiFeO_3$ [4]. In the same year Farokhipoor and Noheda reported the same finding and additionally showed that the domain wall conductivity in $BiFeO_3$ not significantly dependent on the type of domain wall (71° or 109°) - instead it is dependent on defect content [5]. This is consistent with the work of Rojac et al. in 2017 that demonstrated that conductivity of various domain walls in ceramic $BiFeO_3$ can be controlled by post-annealing in nitrogen (reducing) and oxygen (oxidising) atmospheres. This study reveals that defect chemistry and processing conditions heavily affect the conduction behaviour at domain walls [71].

Although much of the work on domain wall conductivity has focussed on $BiFeO_3$ it is interesting that it in fact appears to be a fairly common effect; enhanced domain wall conductivity has also been reported in $PbZr_{0.2}Ti_{0.8}O_3$ [6] and $TbMnO_3$ [7] thin films, and $BaTiO_3$ [8], $ErMnO_3$ [9], $HoMnO_3$ [10] and $LiNbO_3$ [11] single crystals.

As can reasonably be expected, domain walls exhibiting enhanced electrical conductivity can have interesting responses to applied magnetic fields. There have been relatively few studies on this in $BiFeO_3$ and questions remain to be answered. A more detailed discussion of this topic can be found at the start of Chapter 5.

2.10 Ferroelectric polarisation switching

The direction of the ferroelectric polarisation can be switched by application of an electric field. Possible switching pathways are labelled by the angle between old and new polarisation directions. For simple tetragonal ferroelectric materials where polarisation is oriented along the $<001>_{cubic}$ directions two types of switching are available; 90° switching and 180° switching [23]. In rhombohedral ferroelectrics where polarisation is oriented along $<111>_{pc}$ direction three types of switching are available; 71° switching, 109° switching and 180° switching [72].

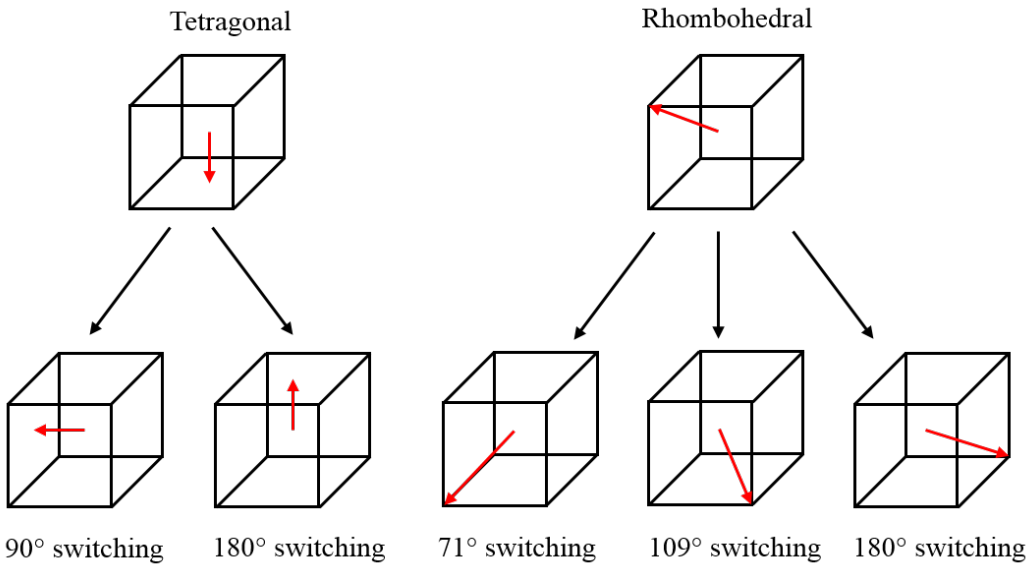

Figure 2.10: Available switching pathways tetragonal and rhombohedral ferroelectrics. The cubes represent the $(001)_{pc}$ oriented pseudocubic unit cell.

These are shown in Fig. 2.10. Since the direction of polarisation is coupled with a structural distortion a ferroelectric switching by any angle other than 180° will be accompanied by a ferroelastic switching.

It is of note that polarisation switching can proceed in a stepwise manner. For example, in the case of a tetragonal ferroelectric material, the polarisation may be switched through an angle of 180° by two 90° steps or one 180° step. Due to the number of switching pathways available in materials with more complicated structures, it is difficult to fully control the route through which switching proceeds. [72]. In addition to crystallographic structure and the energy cost of moving the polarisation through a given switching pathway, factors such as the magnitude of the applied electric field driving the switching can also have an effect.

For the case of materials such as $BiFeO_3$, which are antiferromagnetic, switching by 71° or 109° causes the antiferromagnetic planes and therefore the magnetic easy plane of the canted moment to be rotated. This is because of the coupling to the ferroelectricity and structural distortion. In this way it possible to say that $BiFeO_3$ exhibits magnetoelectric coupling, and this has been demonstrated experimentally [73].

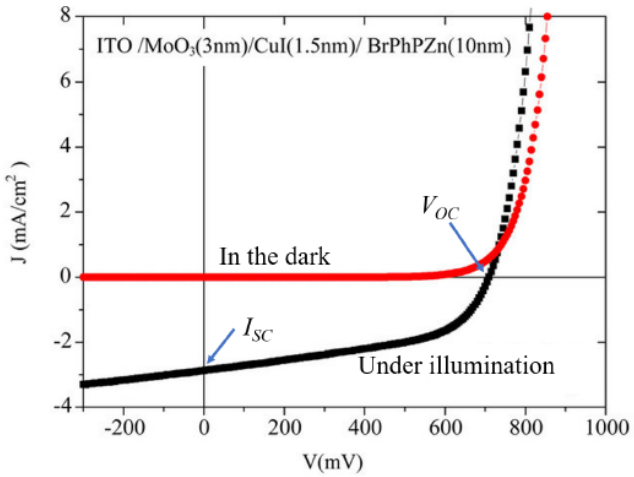

Figure 2.11: Typical current-voltage characteristics of a solar cell. Figure from Ref. [74].

2.11 Photovoltaic effect

The photovoltaic effect arises through two steps. The first of these is the above-band gap light-induced excitation of charge carriers from the valence band to the conduction band. The second of these is the separation of these electrons and holes. The former effect occurs in every semiconducting material under illumination, but the latter step requires some kind of asymmetry.

In most solar cells the asymmetry is achieved by the formation of a p-n junction. An electron rich n-type semiconductor has a higher Fermi level than a hole rich p-type semiconductor. When they form a junction the difference in the Fermi levels induces a built-in field at the interface which opposes diffusion of electrons into the p-type region and holes into the n-type region. The net result of this in a system with short-circuit boundary conditions (i.e. a complete circuit) is that a photovoltaic current is generated. On the other hand, open circuit boundary conditions (i.e. a broken circuit) generate a potential difference, called the open circuit voltage.. The magnitude of the open circuit voltage depends on the photovoltaic current. This is the mechanism by which p-n junctions can be used to generate electricity under illumination. Solar cells made of junctions of two different semiconductors can be called junction solar cells.

Currently the most widely used solar cells are based on p-n junctions and make use of semiconducting materials such as Si and GaAs. Fig. 2.11 shows a typical current-voltage curve of a typical solar cell. As the structure of a solar cell is identical to that of a p-n junction, the current-voltage characteristics are the same

as that of a diode; however once the semiconductor is illuminated a finite current at zero voltage (i.e. no potential difference between the two electrodes) appears. This is called the short-circuit photocurrent I_{sc}. The voltage which blocks the short circuit completely is called the open-circuit voltage V_{oc}.

Ferroelectric materials have an inherent asymmetry due to their noncentrosymmetric structure and exhibit a peculiar photovoltaic effect which is different to that of junction solar cells. The mechanism describing this is called the bulk photovoltaic effect. Unlike the case of junction solar cells, in the framework the bulk photovoltaic effect provides i) the power conversion efficiency is not limited by the Shockley-Queisser limit of 33.7% (the fundamental limit of power conversion efficiency for a single-junction solar cell with optimum band gap of 1.34 eV) and ii) the maximum possible open circuit voltage is not limited by the band gap. Aspects of the bulk photovoltaic effect regarding the roles of domains and domain walls are still under debate, but it is the most likely mechanism to explain the photovoltaic effect in ferroelectric semiconductors because i) a monodomain ferroelectric thin film shows the bulk photovoltaic effect [75] and ii) observed open circuit voltages are too large to be induced electrostatically [76]. A detailed phenomenological description of the bulk photovoltaic effect can be found in the theses of Akash Bhatnagar [77] and Mingmin Yang [78]. It is not included here as it is beyond the scope of what is required for discussion of the photovoltaic data presented towards the end of Chapter 8.

Chapter 3

Experimental methods and sample fabrication

3.1 Atomic force microscopy

Atomic force microscopy (AFM) is a widely used experimental technique due to its high versatility and comparative ease of use. The atomic force microscope was invented by Binning, Quate and Gerber in 1986 and was originally invented for measuring the surface morphology of samples down to atomic resolution [79, 80]. Since then a multitude of variants on this technique have been developed enabling physical properties including electrical conductivity [81], electric charge [82], surface elasticity [83] and magnetic forces [84] to be mapped locally at the nanoscale. The most widely used variant of this technique used in the field of ferroelectrics is piezoelectric force microscopy (PFM) as it enables the ferroelectric domain pattern to be spatially mapped. [85].

3.1.1 Operational principle

In "contact mode" atomic force microscopy, a sharp probe (tip radius typically less than 10 nm) mounted to a cantilever is scanned over a sample surface and the measured signal is compared with a set value with a feedback loop. The output of the feedback loop is applied to a piezoelectric actuator that ensures that the distance between sample and probe is kept constant. In addition to this, the output of the feedback loop can be interpreted directly as a measure of the surface morphology. This is shown schematically in Fig. 3.1. Variations in the surface morphology cause the cantilever to be deformed as it is scanned over the surface. By reflecting a laser spot off the back of the cantilever onto a four quadrant photodetector it is possible

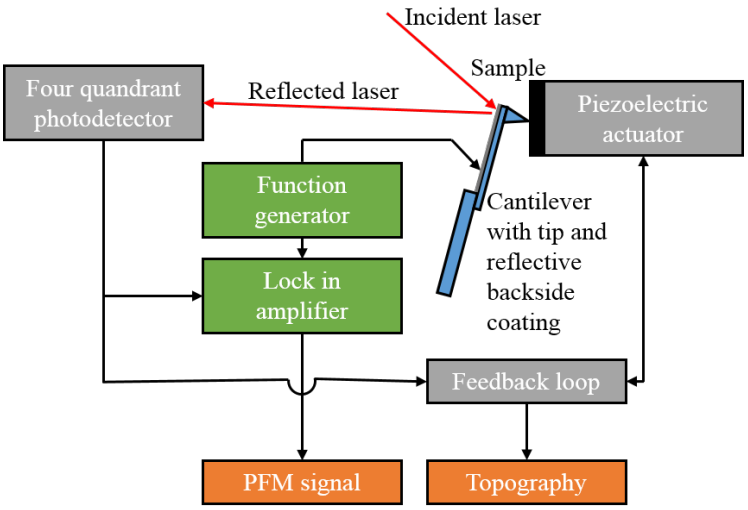

Figure 3.1: Schematic illustrating the basic working principle of the atomic force microscope. The additional components required for PFM are shown in green. Output signals are shown in orange.

to use the cantilever as an optical lever and obtain very sensitive measurements of displacement. The cantilever deflection is made up of contributions from three orthogonal three forces:

1. a force normal to the surface F_N which causes the cantilever to deflect upwards or downwards such that the laser spot moves vertically on the photodetector,

2. an in-plane force F_B which runs parallel to the long side of the cantilever. This results in the cantilever buckling and the laser spot moving vertically on the photodetector, and

3. an in-plane force F_T which acts perpendicular to the long side of the cantilever. This leads to a torsion of the cantilever and horizontal movement on the laser spot.

By comparing measured intensities in each quadrant of the photodetector it is possible to extract the lateral and vertical signals, however it is important to note that F_N and F_B cannot be separated.

While in contact with the surface the tip can be described as experiencing a Lennard-Jones potential of the form

$$V(z) = 4\epsilon \left[\left(\frac{\sigma}{z}\right)^{12} - \left(\frac{\sigma}{z}\right)^{6} \right], \tag{3.1}$$

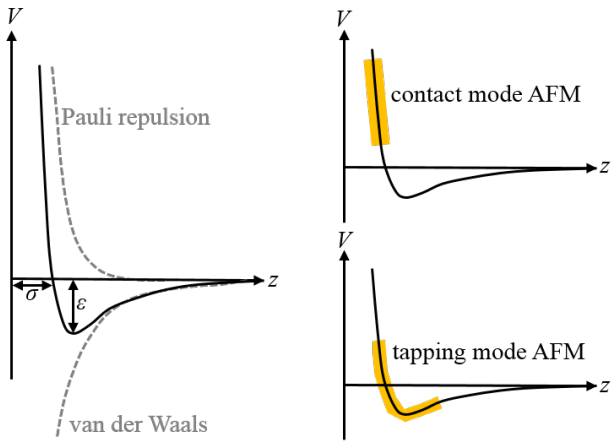

Figure 3.2: Left: the tip-sample distance dependence of the Lennard-Jones potential and its two contributions. Right: force regimes for tapping and contact mode.

where V is the potential, z is the distance between atoms, ϵ is the depth of the potential and σ the distance for which $V(z) = 0$. The two forces described by this potential are the relatively long range (<100 nm) attractive van der Waals forces and the relatively short range (<1 nm) forces from Pauli repulsion. This is shown schematically in Fig. 3.2.

The vertical resolution of AFM is determined by the photodetector sensitivity. Using this approach it common to achieve a resolution of around 0.1 Å. In contrast, the lateral resolution is limited by the tip radius. In fact, the reconstructed image is actually the convolution of the tip and the sample surface, so any damage to the tip can distort the image. For this reason in addition to the contact mode of AFM introduced already, where the steep front part of the potential is used to control a fixed cantilever deflection, it is also possible to operate in a "tapping mode". In that mode of operation the cantilever is subjected to a vibration close to but not at its resonant frequency and the vibration amplitude is taken as the feedback signal. Force regimes for each of these modes are indicated on Fig. 3.2. All AFM characterisation in this thesis was carried out in contact mode and the tapping mode of operation is not discussed further. This was possible as smooth sample surfaces meant that tip damage was not a significant problem.

3.1.2 Piezoelectric force microscopy

Piezoelectric force microscopy is a variant of AFM which is widely used for visualising domain structures in ferroelectric materials. It is a contact mode

technique. The operation of PFM is based on the converse piezoelectric effect, which couples strain and applied electric field. As introduced in section 2.1.1, all ferroelectric materials are also piezoelectric. In PFM, an AC voltage is applied to a conductive tip as it is scanned over the surface of a material, causing the surface of the material under the tip to expand or contract by the converse piezoelectric effect. This deformation is detected by the tip. The measurements of out-of-plane and in-plane tip deflection made by the photodetector are input to two different lock-in amplifiers. The AC voltage applied to the tip is also input to the lock-in amplifiers and is used as the reference signal. It is possible to extract the net piezoelectric response by comparing the reference signal with the deflection signal. This method allows for simultaneous acquisition of the amplitude and phase of both the out-of-plane and in-plane piezoelectric response for a given scan area. As the amplitude and phase of the local piezoelectric response in a ferroelectric is influenced by the polarisation, it is valid to use PFM images as a maps of the of the ferroelectric domain structure.

3.1.3 Piezoelectric force microscopy on rhombohedral $BiFeO_3$

In ferroelectric materials the piezoresponse sampled by PFM is dominated by the expansion and contraction along the direction of the spontaneous polarisation. In $BiFeO_3$ there are eight polarisation variants which point along four polar axes, aligned with the $<111>_{pc}$ family of directions. One result of this is that for $(001)_{pc}$ oriented films there are both out-of-plane and in-plane signals for all areas of the sample. The out-of-plane and in-plane PFM signals consist of vertical and horizontal projections of polarisation respectively. This is in contrast to tetragonal materials where the polarisation for $(001)_{pc}$ oriented films is either purely out-of-plane or in-plane, making it easy to directly map the relative orientations of polarisation in different domains. For the case of rhombohedral ferroelectrics it is possible to extract the types of domains present by comparing PFM data taken for two different sample rotations, separated by 90°. The framework enabling this is shown in Fig. 3.3. The direction of the out-of-plane piezoelectric response can be simply obtained by measuring the out-of-plane deflection. This is independent of sample orientation and scanning direction. In contrast, the in-plane PFM measurement does depend on the orientation of the sample relative to the tip. When the cantilever is oriented along $[010]_{pc}$ only, the polarisation variants that have in-plane projections along $[100]_{pc}$ or $[\bar{1}00]_{pc}$ will be seen, since the torsional force the cantilever experiences is determined by this component of polarisation. Similarly when the cantilever is oriented along $[100]_{pc}$ only, polarisation variants

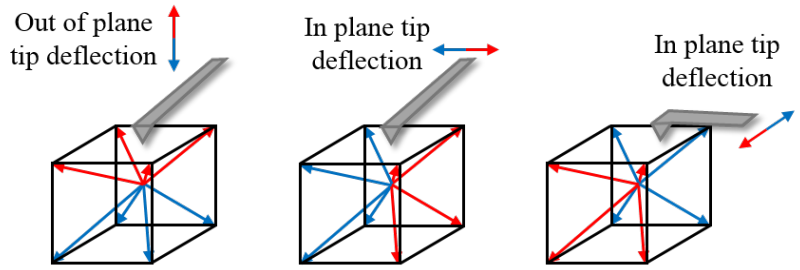

Figure 3.3: Schematic diagram showing two possible scanning orientations for the pseudocubic perovskite unit cell of rhombohedral $BiFeO_3$. It is possible to distinguish between the different in-plane polarisation variants in one scan area by scanning along both $[100]_{pc}$ and $[010]_{pc}$ directions.

with projections along $[010]_{pc}$ or $[0\bar{1}0]_{pc}$ can be distinguished. By combining scans of the same area for these two relative orientations it is possible to reconstruct a picture of the domain structure [86, 87]. When scanning samples at other angles all polarisation variants may be seen in the in-plane PFM images, but the relative orientations of polarisation in each domain cannot be mapped purely from that image.

3.1.4 Through-electrode piezoelectric force microscopy

In conventional PFM the electrical excitation which generates the piezoelectric response of the sample is applied through the tip which is scanned over the sample surface. This allows for high-resolution imaging of the domain structure and also local spectroscopy measurements. In this geometry the electric field generated by the tip is very inhomogeneous which makes analysis of field-induced signals difficult. In other words, PFM measurements of this type collect signal from a surface layer of unknown thickness that is a function of both the contact conditions and also the dielectric permittivity. It is only when the diameter of the tip-sample contact area is on the same order of magnitude as the sample thickness that the field can be treated as approximately homogenous. For standard cantilevers this means that for thicknesses above 20 nm, the field has to be considered inhomogeneous. For experiments which consider ferroelectric switching on samples thicker than this, like those in Chapter 5, this is not ideal.

It is possible to work around the issue of inhomogeneous fields by adopting an approach where the excitation is applied between top and bottom electrodes of a metal-ferroelectric-metal capacitor. Here the excitation is applied to the ferroelectric layer globally instead of locally as it is applied to the whole device area. The cost

of this measurement is that the lateral resolution is lower due to the effect of the top electrode smearing the surface response. The excitation voltage can be applied by either contacting the top electrode with a probe needle or directly with the tip. For both cases the piezoelectric surface response is detected locally with the tip that scanned over the surface of the top electrode. In this configuration the electric field the ferroelectric layer is homogenous, which allows for controlled measurements of the polarisation reversal process and associated domain wall changes in these capacitors to be made [88].

3.2 Dielectric characterisation

The extent to which a dielectric material can be polarised by an applied electric field is one of its most basic and important properties. Different applications require dielectric materials with different properties. To illustrate this: materials with particularly large, small and field-tunable dielectric responses are extensively used as gate electrode materials and insulating layers between conductive components in microelectronic devices, and tunable radio frequency devices respectively [28]. Because of the wide range of applications of dielectric materials there has been a significant research interest in learning how to control and tune the dielectric properties. On a more fundamental level, it is possible to distinguish and systematically investigate the different contributions to overall permittivity (which is directly connected to the polarisability) by changing the magnitude and frequency of the excitation voltage. This kind of systematic study can yield useful insight into the various physical processes present that in turn determine device behaviour.

3.2.1 Basics

In dielectric spectroscopy, the current response of a sample to an applied AC voltage is measured using an impedance analyser, most often as a function of frequency. From this raw data it is possible to calculate the complex permittivity by asserting that the test device is well approximated by an electronic circuit. The simplest model for a dielectric material (far away from any resonance) is an electronic circuit consisting of a capacitor and a resistor connected in parallel. This effectively describes a leaky capacitor. From the measured current and voltage signals and the system dimensions it is possible to calculate the parallel capacitance C_p and the loss tangent tan(δ). Here δ is the phase difference of the

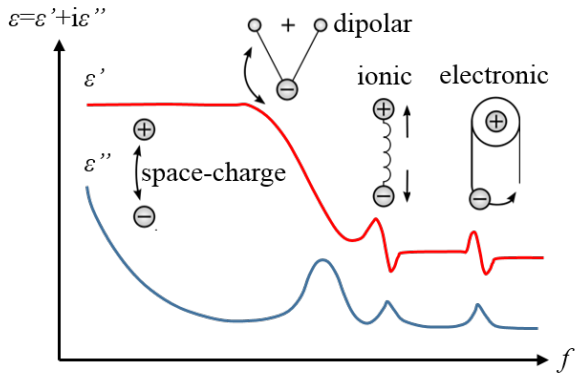

Figure 3.4: Schematic showing the dielectric permittivity spectrum over a wide range of frequencies. Both real (ε') and imaginary (ε'') parts of permittivity. The various contributions, which drop off at different frequencies, are labelled.

current response of the device under test from that of an ideal capacitor. For an ideal capacitor the current response leads the voltage signal by $90°$. In contrast, for an ideal resistor the current response is perfectly in phase with the voltage. For non-ideal capacitors the current response leads the voltage signal by a little less than $90°$. From the values of C_p and $\tan(\delta)$ is possible to directly calculate the real part of relative permittivity ε'_r as

$$\varepsilon'_r = \frac{C_P d}{\varepsilon_0 A} \tag{3.2}$$

where ε_0 is the permittivity of free space and d and A are the distance across and cross sectional areas of the volume where AC voltage is applied. The imaginary part of relative permittivity ε''_r can be calculated directly as

$$\varepsilon''_r = \varepsilon'_r \tan(\delta). \tag{3.3}$$

For the case of a parallel plate capacitor it is trivial to calculate the amplitude of the electric field E_0 by dividing the amplitude of the applied AC voltage by the distance d.

The broadband permittivity spectrum is a useful picture to have in mind when considering the frequency dependence of dielectric permittivity. This is shown in Fig. 3.4. There are four different dielectric mechanisms: space-charge, dipolar, ionic and electronic polarisation. Each of these has a characteristic relaxation frequency above which it its contribution drops off. For ferroelectric materials with a good hysteresis loop, the contribution of space-charge polarisation is very small

and can be neglected. Dipolar polarisation is caused by the temporary induced dipoles between atoms aligning with the applied field. In the absence of an applied field these dipole moments are randomly aligned and there is no resulting net polarisation. Ionic polarisation occurs when neighbouring positive and negative ions within the nucleus of atoms "stretch" under an applied electric field. Electronic polarisation occurs in neutral atoms when an electric field displaces the nucleus with respect to the electrons that surround it. Both electronic and atomic polarisation create induced moments depending on the inherent polarisability of the atoms or molecules.

3.2.2 Rayleigh law

In ferroelectric materials the magnitude of the dielectric response is sensitive to frequency, temperature, and AC electric field amplitude. In addition to the dielectric mechanisms that are present for all dielectric materials, there is also a contribution originating from domain wall motion, which is often significant. Domain walls interact with lattice defects such as vacancies, charged defects, or dislocations. On application of an electric field the domain walls move and several types of displacements can be observed. When a domain wall is trapped at a pinning point it can "jump" to another pinning centre only if the electric field is sufficiently high. Since the domain wall does not return to its initial position, this induces a variation in the global polarisation. In contrast if the field is too weak, the domain wall simply vibrates around its equilibrium position just like a harmonic oscillator. Both these processes contribute to the value of permittivity [89] which, according to the Rayleigh law, varies linearly with the amplitude of the electric field

$$\varepsilon_r(E_0) = \varepsilon_r(0) + \alpha_r E_0. \tag{3.4}$$

Here E_0 is the amplitude of the applied AC electric field, $\varepsilon_r(0)$ is the permittivity at $E_0 = 0$, and α_r is the linear coefficient of E_0. The quantity $\varepsilon_r(0)$ represents the intrinsic lattice and domain wall vibrational contributions to permittivity. It related to reversible processes and can be considered a measure of domain wall mobility. In contrast, the parameter α_r represents domain wall pinning/unpinning and is related to an irreversible modification of the local polarisation. Both parameters depend on crystal structure but α_r is also affected by the presence of impurities, defects and dopants.

The Rayleigh law is only valid in the case of a perfectly random distribution of pinning centres and for a field of higher than the threshold field $E_{th-Rayleigh}$.

If the electric field is too weak ($E_0 < E_{th-Rayleigh}$), the only contribution to permittivity from domain walls is the domain wall vibration, and that permittivity is independent of the field amplitude. Although $E_{th-Rayleigh}$ is a measure of the degree of pinning in the material, this field is not clearly defined and often only the linear and high field regimes are considered. In real ferroelectrics the pinning centres are not randomly distributed. This means that the Rayleigh law is sometimes generalised by expressing it as a power law of the form
$\varepsilon_r(E_0) = \varepsilon_r(0) + \alpha_r \varepsilon_r E_0 + \beta_0^2 E_0^2 + ...$ This generalised description does not include a threshold field.

3.2.3 Hyperbolic law

In 2011 Borderon et al. [89] proposed a hyperbolic law for expressing the permittivity as a function of electric field in the low field regime, where domain wall density is constant. This generalisation of the Rayleigh law enables the contributions to the permittivity from the lattice and each type of domain wall motion, reversible domain wall vibration and irreversible domain wall jump, to be distinguished.

Derivation

The change in polarisation $\Delta P_{(i)}$ due to the displacement of the ith domain wall is given by

$$\Delta P_{(i)} = f_0 P_s \frac{L_i}{L}. \tag{3.5}$$

Here P_s is saturation polarisation and f_0 is a geometrical factor which depends on the direction of the electric field E_0 with respect to the domain wall normal. L is the maximum displacement the domain wall can undertake and $L_{(i)}$ is the total movement of the domain wall. The variation in polarisation is correlated with the relative permittivity as

$$\varepsilon_{r(i)} = \frac{\Delta P_{(i)}}{\varepsilon_0 E_0} = \frac{f_0 P_s}{\varepsilon_0 E_0} \frac{L_{(i)}}{L}. \tag{3.6}$$

In order to obtain the change in polarisation ΔP it is necessary to sum up the contributions of all domain walls giving

$$\Delta P = \sum_i \Delta P_{(i)} = n_D f_0 P_s \frac{\overline{L_{tot}}}{L}, \tag{3.7}$$

where n_D is the number of domain walls in the sample. Let us consider the average total distance $\overline{L_{tot}}$ a domain wall is displaced by as

$$\overline{L_{tot}} = \frac{\sqrt{\sum_i (n_{(i)} L_{(i)})^2}}{n_D} = \frac{\sqrt{(n_{rev} L_{rev})^2 + (n_{irrev} L_{irrev})^2}}{n_D}. \tag{3.8}$$

This corresponds to the quadratic average of the displacement. n_{rev} and n_{irrev} are the number of walls which have, respectively, reversible or irreversible displacement $n_D = n_{rev} + n_{irrev}$. L_{rev} and L_{irrev} are the reversible and irreversible displacement and have already been calculated by Boser [90]. The total relative permittivity due to domain wall motions is thus

$$\varepsilon_{rw} = \frac{f_0 P_s}{\varepsilon_0 E_0} \frac{\sqrt{(n_{rev} L_{rev})^2 + (n_{irrev} L_{irrev})^2}}{n_D L^3} = \sqrt{\varepsilon_{r-rev}^2 + \varepsilon_{r-irrev}^2}. \tag{3.9}$$

In this expression ε_{r-rev} corresponds to the relative permittivity due to reversible domain wall motions. These can be associated with harmonic oscillations and are field independent. This permittivity is similar to the initial dielectric permittivity obtained by Boser. $\varepsilon_{r-irrev}$ is the relative permittivity due to irreversible displacements of the walls and varies linearly with the applied electric field. Hence the contribution of domain wall motions to the permittivity can be expressed as

$$\varepsilon_{rw} = \sqrt{\varepsilon_{r-rev}^2 + (\alpha_r E_0)^2} \tag{3.10}$$

where α_r is the same parameter as in the Rayleigh approach. In order to obtain an expression for the total permittivity ε_r, it is necessary to add the contribution of the polarisation state and intrinsic lattice ε_{rl}. This leads to the hyperbolic law, expressed by

$$\varepsilon_r = \varepsilon_{rl} + \varepsilon_{rw} = \varepsilon_{rl} + \sqrt{\varepsilon_{r-rev}^2 + (\alpha_r E_0)^2} \tag{3.11}$$

The new initial permittivity $\varepsilon_r(E = 0)$ at zero electric field is now the sum of two parts: the coefficient ε_{r-rev} which corresponds to reversible domain wall vibrations and ε_{rl} which is due to the intrinsic lattice.

The Hyperbolic law has two asymptotes: $\varepsilon_r = \varepsilon_{rl} + \alpha_r E_0$ and $\varepsilon_r(E = 0)$. It is straightforward to define the threshold field E_{th} as the point of intersection of these:

$$E_{th} = \frac{\varepsilon_{r-rev}}{\alpha_r}. \tag{3.12}$$

This field corresponds to the ratio between the contributions of each type of domain wall motion and represents the extent of wall pinning in the material.

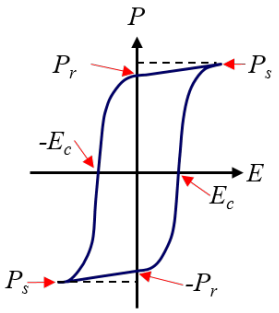

Figure 3.5: Schematic of ferroelectric hysteresis loop. Saturation and remnant polarisations P_s and P_r and critical electric fields E_c are labelled.

It is of note that for hard ferroelectrics, the threshold field is low and the hyperbolic law is well approximated by the first asymptote, which is similar to the Rayleigh law.

$$\varepsilon \approx \varepsilon_{rl} + \alpha_r E_0. \tag{3.13}$$

3.3 Ferroelectric characterisation

Ferroelectric materials are characterised by their polarisation and coercive fields. On application of a triangular voltage pulse to a capacitor device, a current is generated. This current is a combination of drift currents and displacement currents. Sources of drift current include leakage and trapped charges. The current associated with the movement of charges during ferroelectric switching is displacive, as it is time – equivalently frequency – dependent. By measuring at high frequencies (to minimise the effect of leakage), integrating this measured current as a function of time yields a good estimate of the amount of charge that is moved during switching. From this it is simple to calculate the spontaneous polarisation. This can be summarised in the equation

$$P_s = \frac{\int (I_{drift} + I_{displacive})\, dt}{A}, \tag{3.14}$$

where P_s is spontaneous polarisation, I_{drift} and $I_{displacive}$ are drift and displacement currents respectively, and A is the cross sectional area of the capacitor. A schematic of a ferroelectric hysteresis loop is shown in Fig. 3.5.

3.4 Temperature dependent transport measurements

Temperature dependent transport measurements between 80 K and 300 K were carried out using a cryogenic probe station (Lake Shore Ltd.). During electrical measurements, the bottom electrode was contacted to the copper sample holder and Pt top electrodes were contacted with a tungsten probe needle. In all electronic measurements, positive voltages were applied to top electrodes. Transport measurements were acquired using an electrometer (6517A, Keithley) and switching measurements were carried out using a ferroelectric testing system (aixAACT TF2000E).

3.5 Laboratory x-ray diffraction

X-ray diffraction (XRD) provides a means of probing the structure of materials. Many advanced variants of this technique exist, especially at x-ray synchrotrons, but with conventional laboratory diffractometers it is relatively straightforward to obtain precise information about sample composition, thickness, phase purity, and strain relaxation. In this thesis two types of laboratory x-ray measurements were used: simple 2θ-ω scans to probe sample phase purity, thickness and quality, and reciprocal space mapping (RSM) which provides information about the 3-dimensional structure and strain in the film.

There are two types of x-ray scattering. A photon is described as elastically scattered when its incident wavelength is the same as its scattered wavelength, and inelastically scattered when it is not. Elastically scattered photons contain information about the material structure whereas inelastically scattered photons contain information about processes where energy is transferred to/from the material.

Bragg's law states that when an x-ray beam is incident onto a lattice, the angle of incidence θ will elastically reflect back with the same angle of scattering θ when the following condition is fulfilled:

$$n\lambda = 2d\sin(\theta)\,. \tag{3.15}$$

Here the integer n represents the order of diffraction, λ is the wavelength of the incident x-ray and d is the interplanar lattice spacing. From this expression it can be seen that in order to allow for Bragg diffraction, $\lambda < 2d$.

In this work, laboratory based XRD measurements were carried out in Panalytical X'Pert Pro MRD diffractometers with a Cu $K_{\alpha 1}$ hybrid monochromator

as the incident beam optics. The wavelength of Cu $K_{\alpha 1}$ x-rays is 1.5405980 Å.

3.5.1 2θ-ω scan

In 2θ-ω scans the sample is tilted by angle $\delta(\omega)$ as the x-ray detector is simultaneously moved by twice that amount so that $\delta(2\theta) = 2(\delta(\omega))$. This means that different inter-planar spacings are probed and the orientation of planes is kept fixed [91]. From the information this type of scan provides it is simple to calculate the out-of-plane lattice parameter for all materials in the system and also detect impurity phases which may also be present, like Bi_2O_3 and Fe_2O_3 in the case of $BiFeO_3$ thin films [92].

Before making a 2θ-ω scan it is necessary to align the sample. This is done by finding a strong peak, such as the $(002)_{pc}$ $DyScO_3$ or (002) $SrTiO_3$ substrate peak, and tuning geometric parameters, mostly the vertical tilt χ and the horizontal tilt ω, for the calculated value of 2θ where a peak is expected such that the intensity of the Bragg peak is maximised [91].

It is often possible to estimate layer thicknesses in high quality films from the Laue oscillations about layer peaks [91, 93].

3.5.2 Reciprocal space mapping

One limitation of 2θ-ω scans is that they normally only give information for the component of the lattice normal to the surface, i.e. the out-of-plane component. In order to have a complete knowledge of the structure it is important to probe the in-plane components too. Reciprocal space mapping is the most convenient way to do this for thin films.

Unlike 2θ-ω scans, a reciprocal space map samples a measures a range of inter-planar spacings and multiple plane orientations are scanned. This is done out by aligning to a peak then making a number of 2θ-ω scans at different values of $(\theta - \omega)$. Measured peak positions with interplanar spacing d and "offset" $(\theta - \omega)$ can be decomposed into parts parallel and perpendicular to the sample surface and the reciprocal lattice vector q can be represented as

$$q = (q_{\parallel}, q_{\perp}) = \frac{2\pi}{\lambda}(\cos(\theta) - \cos(\omega), \sin(\theta) + \sin(\omega)). \tag{3.16}$$

Here ω is the incident x-ray angle, θ is the scattered x-ray angle and λ is the x-ray wavelength. The centre of mass of the out-of-plane component of the (hkl)

reflection in the RSM, $q_{hkl\perp}$ is related to the lattice spacing d_{hkl} by

$$d_{hkl} = \frac{2\pi n}{q_{hkl\perp}} \tag{3.17}$$

where n is the order of the diffraction peak. The in-plane component $q_{\perp}$ contains information about crystallographic tilting, scattering off of periodic nanostructures and mosaicity [91].

For the case of materials where the structure is more complicated due to an in-plane distortion of the unit cell, such as $BiFeO_3$, the extracted value of the out-of-plane lattice parameter depends on crystal orientation. This is in contrast to the in-plane components which do not vary. By measuring reflections with different crystal orientations it is possible to extract information about the direction of distortion and determine the full three dimensional structure. For samples with a domain structure this offers an opportunity, as within a domain the distortion is aligned with the polarisation direction. This means that the splitting shown about a peak in a RSM may contain information about the periodic ferroelastic domain structure. For example, the $(002)_{pc}$ RSM for a $BiFeO_3$ sample with a two variant 109° stripe domain pattern (say r_1^-/r_4^+) will show the $BiFeO_3$ peak split in two for the geometry where the in-plane component of the incident beam is aligned with the net polarisation and unsplit for the geometry when it is perpendicular [94].

3.6 Simultaneous time resolved x-ray diffraction and electrical characterisation

Time resolved structural and electrical characterisation of ferroelectric capacitor devices were carried out at the KMC-3 XPP end station at the BESSY II x-ray synchrotron, Berlin, Germany.

3.6.1 Electrical characterisation

In these experiments voltage pulse sequences are generated with a function generator (Keithley 3390) and the output was recorded with an oscilloscope (Agilent DSO9404A). With this setup, Positive-Up-Negative-Down (PUND) pulse sequence were applied. The electrical data for this is shown schematically in Fig. 3.6. Rectangular voltage pulses, all of equal magnitude, are applied in pairs with each pair having the opposite polarity to the last. In both pulses of a pair, there are a variety of contributions to the current such as leakage and capacitative charging.

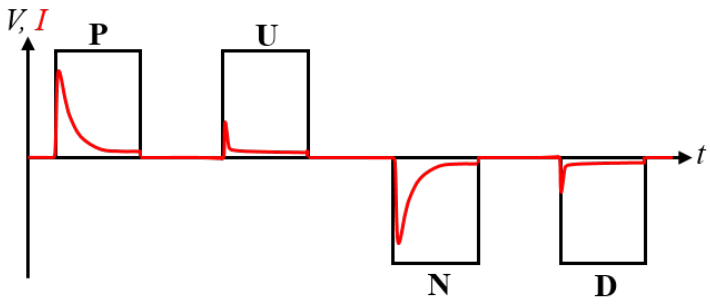

Figure 3.6: Schematic showing the applied voltage (black) and current response (red) of a sample probed with a rectangular PUND sequence.

However, the first pulse in a pair also forces the reversal of the polarisation, creating a contribution to the current that does not occur on the second pulse. Hence, by subtracting the current response of the second pulse from the first pulse it is possible to extract the displacement current associated with the polarisation switching. By integrating the current response of a capacitor device with respect to time it is possible to track the charge flow within the device.

The sample itself is mounted on a four circle goniometer that allows for diffraction in Bragg geometry, with diffracted x-rays being collected by an x-ray detector. The top electrode of the device under test was contacted from the top with a tungsten needle with a contact diameter of around 5 μm. The conductive bottom electrode was contacted with conductive silver paste. The sample is mounted on an XY stage enabling different devices to be contacted easily while keeping the needle position fixed. Both the needle and metallic sample stage were connected to the electrical setup enabling voltage to be applied across the device and the current response measured. All x-ray measurements here were made at room temperature (around 300 K) and atmospheric pressure.

3.6.2 Time resolved XRD

Overview

BESSY II is a user facility that provides high brilliance photon pulses with wavelengths ranging from THz to hard x-rays. For the work carried out at BESSY II presented in Chapters 6 and 7 the energy of photons in the incident beam was selected as 9 keV. The corresponding wavelength of around 1.38 Å is similar to the Cu $K_{\alpha 1}$ radiation used in laboratory diffractometers. Selecting a wavelength in this range ensured that the x-rays probed all layers in the device structures used.

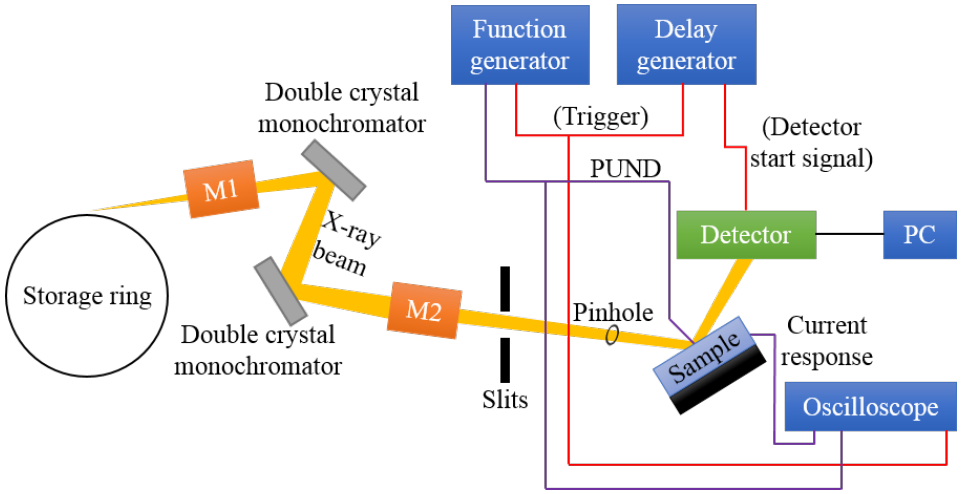

Figure 3.7: Simplified schematic of the time resolved experimental setup. M1 and M2 are toroidal x-ray mirrors. Trigger signals are sent along red lines. Purple lines are used for the electrical characterisation.

In addition, strong anomalous scattering of x-rays around this wavelength in the diffracted signal allows the polarisation state of the sample to be obtained [95]. A schematic for the setup used for time resolved measurements at the KMC-3 XPP end station is shown in Fig. 3.7. Electron bunches of 1.7 GeV are accelerated and injected into the storage ring, producing photon bunches of 5-70 ps duration, depending on the operation mode. In the standard multi-bunch mode (used here) there are typically 350 equal packets in the ring, each with a time distance of 2 ns. Other modes of operation, with shorter bunches and lower intensity, are possible but were not used here. The high photon flux in the multi-bunch mode allows for detection of lattice changes down to one part in 10^6 [96]. The spatial resolution of measurements is set by tuning the beam size. This is done by putting x-ray slits in front of mirror M2 and right in front of the sample. Using this method it is possible to reduce the diameter of the x-ray spot to 15 μm, however in the experiments carried out here an x-ray spot of nominal area 300×150 μm^2 was typically used. This is similar to the dimensions of the devices under test.

Detectors, connections, and synchronisation

To obtain reciprocal space maps, a two-dimensional area detector (Pilatus hybrid pixel detector 100k, Dectris) was used. This detector consists of a silicon module with a 195×487 pixel charge readout array. The size of each pixel is 172 μm square and the readout time is a few milliseconds. Each pixel works as a single

photon counter. In order to obtain time resolved data, a measurement window for the detector is defined such that only x-rays arriving within a set time interval are recorded. This neglects a significant proportion of the x-ray flux. The detector gate can be shifted relative to the electrical pulse onset using a delay generator (Stanford Research DG645). After the measurements RSMs are calculated using a Python script using the library xrayutilities [97]. The time resolution of measurements with this detector are determined by the scintillator crystal in the detector which has a decay time of 1 ns.

To obtain measurements of the structural changes with nanosecond time resolution a home made one-dimensional point detector was used. This consists of a fast x-ray scintillator with a rise time less than 0.5 ps and a decay time of around 1 ns. It converts incoming x-rays into optical photons that are then detected by a photomultiplier tube (Hamamatsu). With this detector, a single 8.9 keV photon generates around 100 optical photons, which are subsequently detected by the photomultiplier tube. The output signal of the photomultiplier tube is sent to a time-correlated single photon counting module (PicoHarp300, PicoQuant) via a current amplifier. The x-ray photon flux per bunch is sufficiently small to prevent counting multiple x-ray photons as a single event. Similarly to the area detector, the time window probed can be tuned using a delay generator. The time resolution using this detector is limited by the PicoHarp counting module: the shortest time channel is 4 ps

In both of these schemes the field is applied hundreds of times to record a complete Bragg peak at each time bin in the voltage pulse sequence.

Sample alignment and spatial overlap

In order to align samples and devices with the incident beam the following procedure is used:

1. To align the sample surface to the direct beam, perform a half cut scan.

2. To determine the lattice constant of layers accurately, put the direct beam onto the area detector to determine the pixel of zero angular position, then align the Bragg peak of the substrate to it.

3. To align the x-ray beam to the contacted device, first move the incident beam close to the needle tip and measure a Bragg peak of the ferroelectric layer without any excitation. Then apply a high enough voltage to cause some significant piezoelectric displacement and measure the Bragg peak under the

field. A comparison of the two measurements gives an idea how far the beam is from the position where it has best spatial overlap, since the difference is greatest when this condition is fulfilled. By tuning the in position of the sample in X and Y, this parameter can be optimised.

Once this process is complete time resolved measurement can start.

Laser assisted switching

The spontaneous polarisation of ferroelectrics is most commonly reversed through application of an external electric field, however in principle it is possible to assist this process in capacitor devices by applying a laser pulse during the ferroelectric switching event, which launches an acoustic strain wave (compressive) from a metallic electrode layer. This effect is studied in Chapter 7.

A 1028 nm amplifier based laser system (LightConversion Pharos) was used to deliver pulses at a frequency of 2.6022 kHz which were synchronised to the detector and the pulse generator. With this system the pulse duration is controllable. Upon reaching the device under test the laser pulse has a range of possible effects, including sample heating, creation of hot electrons in the conducting electrode layers, and the formation of a compressive acoustic strain wave, starting in the bottom electrode oxide layer and propagating through the ferroelectric layer. This energy of this illumination is far below the band gap of $BiFeO_3$ (3.5-3.7 eV) and $BaTiO_3$ (3.2 eV) so should not generate hot carriers in the ferroelectric layers. The transient change in the polarisation switching is expected to be apparent in both the electronic and structural time-resolved responses of the sample even when a sub-coercive field is applied. The experimental setup used for this measurement is the same as that shown in Fig. 3.7, just with the laser and associated electrical connections added.

Data processing

The recorded data from the two-dimensional Pilatus area detector is in terms of 2θ and ω angles. From this it is convenient to plot data series collected at different delays as reciprocal space maps. With the data in this format it is possible to fit the peaks and extract the time dependence. From this process the following parameters are output:

1. the centre of mass of the peak. From this the out-of-plane lattice parameter c can be calculated. Sometimes it is clearer to frame the change in c as an induced strain $\epsilon = \Delta c/c$,

2. the maximum intensity of the peak,

3. the full width at half maximum of the peak in each of $q_\perp$ and $q_\parallel$. These parameters describe structural disorder, and

4. the integrated peak area. This parameter is proportional to the square of the structure factor.

Similarly, the recorded data from the one-dimensional point detector yield 2θ and ω angles. At each voltage delay a single 2θ-ω scan is carried out. The curves of intensity as a function of ω at different time delays are then fitted, enabling the time dependence of the following structural parameters to be extracted:

1. the centre of mass of the peak,

2. the maximum intensity of the peak,

3. the full width at half maximum of the peak in ω, and

4. the integrated peak area.

The main difference between these sets of parameters is that the point detector does not allow to the contributions of the in-plane $q_\parallel$ and out-of-plane $q_\perp$ dynamics to be be distinguished.

Voigt functions were used order to fit the peaks in the raw data. This was done using the LMFIT package in Python [98]. Voigt functions were chosen to fit the raw data as they were found to yield better fits than pseudo-Voight, Gaussian or Lorentzian functions.

Sometimes in time-resolved measurements such as this it is helpful to look at the differences in datasets instead of the raw data. As an example, for the process of electric field driven polarisation reversal it is clearest to compare the peak widths relative to the value when no field is applied, i.e. $w_\perp(t)/w_\perp(t=0, V=0)$. This is possible because the intrinsic peak width of the ferroelectric layer depends on so many parameters like strain, defect density, layer thickness, etc., which are practically not affected by the ferroelectric switching process. Hence the relative changes as function of time are often the quantities of most interest. When this normalisation is done in Chapters 6 and 7 a tilde is placed above the parameter symbol, e.g. $\widetilde{w}_\perp$, and specific details of how the normalisation was carried out is given.

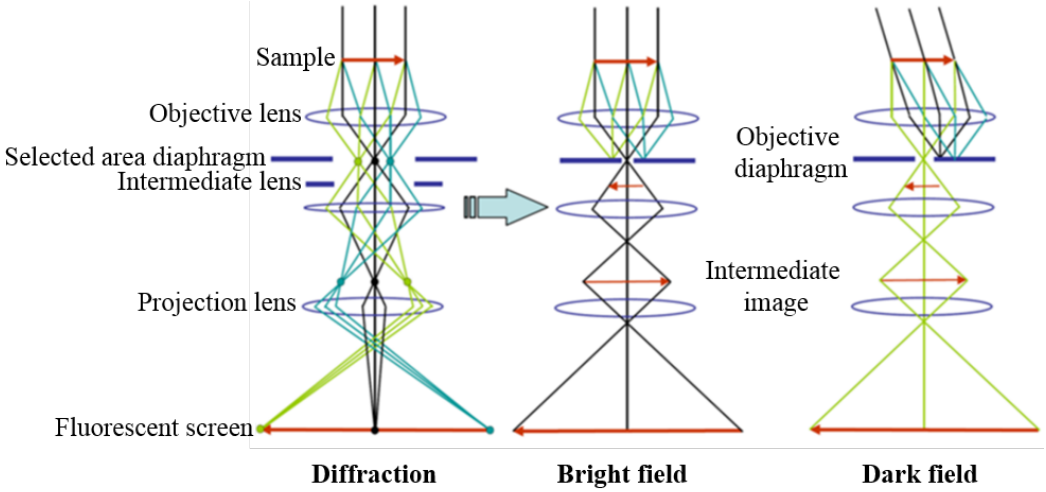

Figure 3.8: Electron path in TEM for diffraction, bright field and dark field modes. Figure adapted from Ref. [99].

3.7 Transmission electron microscopy

Unlike XRD and AFM, transmission electron microscopy (TEM) enables the structure of materials to be directly studied with atomic resolution. This technique involves imaging the projection of very thin cross sections of samples (<100 nm) using an homogenous mono-energetic electron beam.

Three modes of TEM are shown in Fig. 3.8. The first of these is conventional TEM, i.e. diffraction mode, where the intermediate lens focuses on the image plane of the objective lens. The resulting image is a combination of all transmitted and diffracted electrons and has low contrast. In order to improve the contrast it is possible to adjust the optics by placing an objective aperture in the back focal plane of the objective. When it allows the diffracted beam to pass, a dark field image is obtained. When it allows the transmitted beam to pass, a bright field image is obtained.

In the transmission processes, electrons are scattered by the interactions with the lattice. The scattering strength is sensitive to the atomic number Z and the sample thickness. In bright field TEM, high-Z atoms and relatively thick areas appear darker. The opposite is true for dark field TEM [100]. It is possible to combine bright field and dark field TEM images in order to obtain the atomic positions of both light and heavy atoms with picometer accuracy [101], but for the investigations carried out in Chapter 8 it was possible to use the bright field image only. This was because it was sufficient to consider the positions of the heavy

metal cations only in that work.

By measuring atomic displacements on high resolution TEM images, it is possible to map out a number of interesting physical properties in a TEM cross sectional sample with unit cell precision. One example of this, which is heavily used in Chapter 8, is that it is possible to effectively map the electric polarisation in $BiFeO_3$ by considering the relative shifts of the A-site and B-site sublattices, the main structural deformations associated with the ferroelectricity in that system [102]. Another example is that it is possible to locally map the strain fields and rotations in a sample by again considering atomic displacements and comparing the experimental result with that of a set of perfect planes. For this analysis the software package Strain++ was used [103].

TEM sample preparation is a relatively demanding process. In order to create a sample suitable for cross sectional TEM investigations it is necessary to thin it until it is electron-transparent. The classical way to prepare TEM samples is to cut the macroscopic sample, grind and polish it using abrasive SiC paper, then perform ion milling. This method is time efficient but also destructive. In comparison, cross section lamellar samples can be also obtained by focussed ion beam milling (FIB). Using this method sample damage is located exclusively near the surface region from which a small slice of material is removed. That method was used in this work. The specific tool used was a dual beam Jeol 4500 FIB/SEM. Milling was carried out using a Ga+ ion beam and imaging was enabled with the electron beam (as in scanning electron microscopy). In order to mechanically protect the sample surface from damage and also protect charge build up, a common problem with insulating materials, a conducting layer of Au was deposited on the sample surface and grounded to the metal sample holder using conductive silver paint. After the lamellar sample is cut out of the sample using FIB, it is lifted out and attached to a TEM grid on which it is further thinned and gently polished with the ion beam in order to remove regions which have suffered damage and ensure electron transparency [104].

3.8 Photovoltaic characterisation

Temperature dependant photovoltaic characterisation of a $BiFeO_3$ thin film deposited directly on an insulating $NdScO_3$ substrate was carried out and is presented in Chapter 8. Measurement electrodes were deposited on the surface of the film and the device gap was illuminated with monochromatic linearly polarised light from a 405 nm laser (Newport). An electrometer (6517A, Keithley) was

used to measure the electrical behaviour of devices both when illuminated and in the dark. Voltage was applied and current was measured. The sample was mounted on a holder inside an optical cryostat (VPF-700, Janis) and connections to electrodes were fed out of the cryostat. Electrodes were connected to the electrical measurement system with fine metal wires and conductive silver paint. Measurements with the laser were carried out with the illumination centred on the electrode gap. The laser beam was centred on that area by measuring the current during positioning of the laser and maximising the measured photocurrent.

3.9 Sample fabrication by pulsed laser deposition

3.9.1 Overview

Pulsed laser deposition (PLD) is a thin film deposition technique widely used for deposition of complex oxide materials. In this method, a high power pulsed laser is used to ablate a sintered ceramic or single crystal target in a reactive oxygen atmosphere. Typically the oxygen pressure is around 0.1 mbar but pressures as high as few tens of millibar can be used. Typically each laser pulse has an energy of around 50 mJ and is focussed onto an area of around 10 mm^2. Each laser pulse itself approximately 20 ns in duration. The penetration depth of the laser pulse into the target can be as large as several microns. The extremely high energy density causes each pulse to vaporise target material and generate a plasma plume, which condenses to form a film on a heated (typically 600-700 °C) substrate. The highly energetic nature of this process helps ensure stoichiometric target ablation. One major advantage of PLD over some other methods is that it is simple to grow multiple materials in the same PLD system by simply replacing the target – multiple targets can be mounted in a chamber at the same time on a carousel. The growth rate of the epitaxial layers of complex oxide materials is typically 0.1-1 Å/s, and anywhere between a few tens to a few hundred pulses is required to complete a one unit cell layer.

In this work epitaxial thin films of $BiFeO_3$, $BiFe_{0.95}Mn_{0.05}O_3$, $SrRuO_3$, (La,Sr)MnO_3 and $BaTiO_3$ were deposited by PLD using a Coherent LPXpro 210 248 nm KrF excimer laser with $\sim$20 ns pulse duration. A schematic diagram of the PLD setup used is shown in Fig. 3.9. It is possible to monitor the epitaxial layers using in-situ characterisation techniques such as reflection high-energy electron diffraction (RHEED) but such methods were not used here.

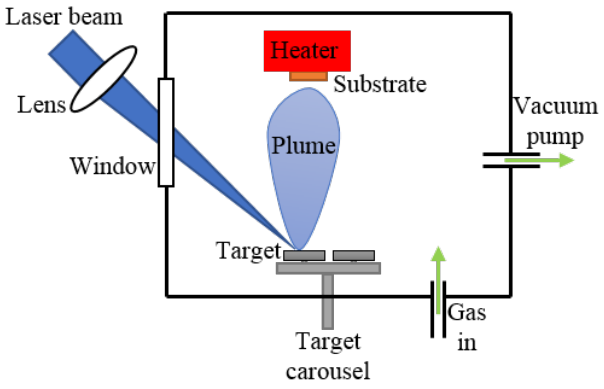

Figure 3.9: Schematic view of a simple PLD chamber.

3.9.2 Substrate treatment

In order to achieve high quality epitaxial films it is often critical to ensure that the substrate material has single termination and is atomically flat. This is because the atomic arrangements and reaction chemistry of the top surface layer determines the growth dynamics of the first few layers, and the form of those propagate through and affect the form of the rest of the growth. In this thesis three types of substrate were used. $SrTiO_3(001)_c$, $DyScO_3(110)_o$ and $NdScO_3(110)_o$. The result of this is that all the films deposited here are $(001)_{pc}$ oriented. Substrates were sourced from Crystec GmbH (Germany) and SurfaceNet GmbH (Germany) and polished with miscut angle of around 0.1°.

The first treatment to obtain single termination $SrTiO_3$ $(001)_c$ surface was developed by Kawasaki et al. [46, 105] and subsequently refined by Koster et al. [106, 107]. Here substrate pieces were first soaked in DI water for 30 mins in an ultrasound bath. This has the effect of hydroxylating the SrO terminated regions of the substrate surface. Secondly substrate pieces were directly dipped in NH_4F buffered HF (7:1) for 15 s. In this step the hydroxylated SrO regions were preferentially etched away, leaving a surface with pure TiO_2 termination. Finally substrate pieces were annealed in air for 1 hour at 1000 °C. This temperature and dwell time was chosen as it is sufficiently high that the surface reconstructs to form unit cell high terraces but is not so high that Sr diffusion occurs, spoiling the single termination. In order to grow $SrRuO_3$ films on $SrTiO_3$ in the step flow growth mode it is crucial to have single termination. Interestingly it was found that after a few weeks the substrate surface loses its single termination, but this was simply recovered by repeating the DI water soak and acid dip steps or by placing

the substrate in DI water and heating at 80 °C for 1 hour. Both of these treatments efficiently removed any $Sr(OH)_2$ that forms at the surface and left the step terrace structure effectively repaired.

Various treatments for $DyScO_3$ substrates have reported in the literature. These include one step processes consisting of an annealing step at around 950-1200 °C in oxygen [108, 109], argon [108], air [110], and two step processes where a chemical treatment consisting of an etch in concentrated NaOH after an optional dip in buffered HF is added after the annealing step [111, 112]. Over the course of this work it has been found:

1. regardless of atmosphere, one step annealing processes do not reliably produce surfaces with single termination despite yielding excellent step terrace structures,

2. in order to reproducibly obtain perfect single termination it is necessary to use a two step process consisting of an oxygen anneal followed by an etch in NaOH. This treatment allows for two-dimensional growth of $SrRuO_3$ films of any thickness,

3. the nature of the annealing process has a significant effect on the domain structure of $BiFeO_3$ films which are deposited on the substrate surface directly or with a bottom electrode layer of either $La_{0.7}Sr_{0.3}MnO_3$ or $SrRuO_3$, and

4. it is possible to deposit $SrRuO_3$ films which are atomically flat and have a step terrace structure on as-received untreated $DyScO_3$ substrates, so long as the layer thickness is around 20-30 nm.

These observations are consistent with what is already reported in the literature.

$NdScO_3$ substrate pieces were not treated before deposition.

3.9.3 Optimised $BiFeO_3$ deposition

Despite the large amount of interest in $BiFeO_3$ in recent years and there being several papers where optimisation of PLD growth parameters are discussed [92, 113–117], relatively few of these studies [93, 118] are systematic and prove the optimised films have both high structural quality and good electrical characteristics – i.e. are phase pure, have good surface morphology, ordered domain structures, and robust ferroelectric properties. For the investigations on $BiFeO_3$ in this thesis, it is preferable for samples to present all four of these characteristics. In addition to this, a wide range of deposition parameters for $BiFeO_3$ thin films are reported. The

effect of tuning various deposition parameters on $BiFeO_3$ film growth on $DyScO_3$ and $SrTiO_3$ substrates, with and without $La_{0.7}Sr_{0.3}MnO_3$ and $SrRuO_3$ buffered bottom electrode layers, is discussed. Mn doping by 5% did not noticeably affect growth dynamics.

It has been observed that substrate treatment has no effect on phase composition of $BiFeO_3$ films, however it has a significant effect on the domain patterns and surface morphology of deposited $BiFeO_3$ films. During the course of this work it has been observed here that:

- depositing $BiFeO_3$ directly on bare $DyScO_3$ favours the formation of 109° domain walls,
- depositing $BiFeO_3$ directly on air annealed $DyScO_3$ also favours the formation of 109° domain walls, but to a lesser extent,
- depositing $BiFeO_3$ directly on oxygen annealed $DyScO_3$ favours the formation of 71° domain walls,
- depositing $BiFeO_3$ on $DyScO_3$ substrates with conducting buffer layers make it favourable for polarisation to point down (due to the electrostatic boundary conditions) and aid formation of 71° domain walls, but it is possible to stabalise 109° stripe domain $BiFeO_3$ on LSMO/DSO if the Bi deficiency in the $BiFeO_3$ is sufficiently high, and
- the step flow growth mode is only accessible on $SrTiO_3$ if a conductive $SrRuO_3$ buffer layer is introduced.

The effect of oxygen pressure on the stoichiometry of $BiFeO_3$ films is clearly reported in the study of Bea et al. [92]. When the oxygen pressure is too low, Fe_2O_3 is driven to form. When the oxygen pressure is too high, Bi_2O_3 is driven to form. For the correct energy and temperature parameters, there exists a window in oxygen pressure for single phase $BiFeO_3$ growth. Oxygen pressure can be used as a lever to control Bi deficiency which is an important parameter when working to stabilise either 71° or 109° stripe domain patterns. Lower oxygen pressure favours the formation of 109° domains as it drives Bi deficiency, and higher oxygen pressure favours the formation of ordered 71° domains. Intermediate pressures, in contrast, tend to yield mixed or disordered domain patterns. With a bottom electrode layer there exists a relatively wide window of oxygen pressure for which there is step flow growth of $BiFeO_3$ on SRO/DSO. This is similar to what is reported for the growth on SRO/STO by Jiang et al. [118].

Deposition temperature mainly has an effect on the phase composition of $BiFeO_3$ layers, but can also affect the domain pattern as it drives Bi deficiency [115]. Regardless of whether deposition is with a bottom electrode layer or not, at low temperature there is Bi_2O_3 and at high temperature there is Fe_2O_3. From the perspective of fabricating devices with good electrical performance, it was found favourable to deposit in the part of the growth window with relatively high temperature as it reduced the number of outgrowths of misoriented $BiFeO_3$ in the layer. These can significantly compromise the electrical performance of devices, even in single phase films. Higher temperature tends to favour less defective films.

The laser fluence has a number of important effects on the deposition as it is related to the stoichiometry of the plume, the energetics of atoms in the growth surface and the growth rate. When the fluence is too high, outgrowths of misoriented $BiFeO_3$ and Bi rich phases form. Part of this is driven by the interactions of ions in the plasma plume, which form particles that embed themselves in the film. When fluence is too low, the deposition rate is slow and ablation is not stoichiometric. Again, from the perspective of device engineering, it is favourable to use a plume that is sufficiently energetic that ablation is stoichiometric but is not of such high energy density that particles in the plume interact.

The laser frequency is the main lever with which to control the growth rate. In the work here it was found that growth rates in the range 0.1-0.3 Å/s enabled high quality films with ordered domain patterns to be stabilised. Slower growth rates favour more Bi deficient films.

The target-substrate is an effective control of the stoichiometry of the plume which the substrate samples. It is a relatively coarse control of stoichiometry which does not significantly change the growth rate. Decreasing the target-sample distance enables a lower fluence to be used, which can ultimately help reduce the number of outgrowths in the film.

Using targets with Bi excess effectively shifts the growth window towards higher temperature, lower fluence, and overall a lower growth rate. Slowing down the growth in this way was found to suppress certain kinds of defects and significantly improve electrical performance (i.e. reduce DC leakage). Use of Bi deficient targets enables 109° stripe domains to be stabilised on LSMO/DSO. This is unexpected and not previously reported, but is in line with a similar result that has been obtained for $BiFeO_3$ directly on $DyScO_3$ in another group [119]. They stabilise 71° from a polished target and 109° from heavily ablated target. The lesson to learn from this result is that to properly control the stoichiometry of $BiFeO_3$ thin films it is important to polish the target surface thoroughly before every deposition.

Bea et al. have reported that that more segregation of parasite phases occurs in thicker films [120]. This stands to reason as the thicker the film the longer the time given for segregation to occur. The result of this is that it easier to grow thin phase pure films than thick phase pure films.

It has been found that cooling quickly in a low oxygen pressure increases domain wall conductivity, and cooling slowly in a high oxygen pressure reduces leakage and improves electrical performance. It is of note though that as far as the experiments carried out by the present author suggest, all the conductivity which is associated with fast cooling at low pressure is thermally activated.

In summary it is advantageous to be in the corner of the growth window where temperature is high, oxygen pressure pressure is sufficiently high that domains are nice and ordered but not too high there are interactions in the plume between ions (particles) and outgrowths on the surface, and fluence is be high enough to ensure stoichiometric ablation but not so high that interactions in the plume cause problems. Bi excess in the target pushes the growth window in this direction but if the excess is too large the growth rate becomes intolerably slow. The slowest and highest growth rates reported for $BiFeO_3$ in the literature which yield good 71° stripe domains are 15 nm/hour [121] and 250 nm/hour [122]. As there is an order of magnitude of difference between these it is reasonable to expect that at the atomic level these films will not be identical. A slow growth rate was found to yield domain walls with greater conductivity at room temperature as more time is given for defects to form at domain walls during the growth, but the extra conductivity from this method is thermally activated and does not persist at low temperature. For investigations and applications of domain wall physics in $BiFeO_3$ this knowledge is useful.

Optimised $BiFeO_3$ for the different targets used in this work ranged were in the range 650-690 °C, 0.15-0.225 mbar, 5-12 Hz, 0.2-0.6 J/cm^2, 40-55 mm. The spot size used throughout was 9-10 mm^2.

3.9.4 $BiFeO_3$ target fabrication and notes on target handling

Ceramic PLD targets for the $BiFeO_3$ films used in this work were fabricated using two different methods: conventional solid state reaction and coprecipitation. Both of these methods yielded dense PLD targets with a minimal particle / droplet problem. For both methods, powders were wet milled with isopropanol in a Retsch XRD-Mill McCrone vibromill with agate milling media. Particle sizes were sub-micron after grinding in all cases, ensuring sintered ceramic pellets had high density. Bi_2O_3, Fe_2O_3, and Fe powders of 99.99% purity or higher from Fisher

Scientific or Sigma Aldrich were used. Over the course of the present work it was found that the co-precipitation method yielded targets which were denser and gave films with a reduced particle problem.

In the conventional solid state reaction method, powders were wet milled, dried, calcined, wet milled, dried, mixed with 5 wt. % polyvinyl alcohol binder and pressed into a pellet with a uniaxial press. Calcination and sintering were done in air at 750 °C for 2 hours and 850 °C for 4 hours respectively. The sintering step included a burnout step to remove PVA consisting of a dwell at 400 °C for 2 hours followed by a dwell at 500 °C for 1 hour.

In the coprecipitation method, Bi_2O_3 and Fe powder were completely reacted with analytical grade nitric acid to form a solution of bismuth nitrate and iron nitrate. This was then neutralised with an excess of ammonia solution to precipitate out the insoluble metal hydroxides, and heated on a hot plate to remove excess water. The resulting slurry was then further heated up to 350 °C to completely remove the ammonium nitrate by-product as well as any water. The resulting fine mixture of oxides was then calcined at 600 °C for 3 hours before being wet milled, dried, mixed with 5 wt. % polyvinyl alcohol binder, pressed into a pellet, and sintered at 800 °C for 3 hours with the same burnout step as for the conventional solid state reaction method.

Before each deposition, targets were polished with abrasive SiC paper (grades P800 to P4000, Struers), rinsed in isopropanol in an ultrasound bath for 15 s, blown dry, then baked on a hot plate at 150 °C for 10 mins to remove any remaining solvent. Before deposition each target was preablated in deposition conditions by a number of counts that would correspond to around 20 nm of material being deposited. This treatment increases film quality.

3.9.5 Optimised of $BaTiO_3$ deposition

$BaTiO_3$ thin films on LSMO/STO were deposited using similar parameters to Li et al. [123]. Like the work there it was found that oxygen pressure had a significant effect on the leakage. Optimised deposition parameters were 650°C, 0.4 J/cm^2, 3×10^{-3} mbar, 5 Hz, 55 mm. The DC leakage was found to increase when oxygen pressure was changed from this value, causing the switching properties to degrade. After deposition $BaTiO_3$ films were cooled at a rate of 15 ∘C/min in the same oxygen atmosphere as they were deposited. The $BaTiO_3$ target used in this work was stoichiometric and supplied by Praxair Inc. (USA).

3.9.6 Optimised $SrRuO_3$ and $La_{0.7}Sr_{0.3}MnO_3$ deposition

$SrRuO_3$ films were deposited on both $SrTiO_3$ and $DyScO_3$. Details of the growth are similar to those published by Hong et al. [124]. The specific parameters used were 680 °C, 0.4 J/cm^2, 0.15 mbar and pulse frequency 3-18 Hz, 55 mm. The appropriate pulse frequency to choose depended significantly on the terrace width, i.e. the miscut angle, of the substrate. The terrace widths corresponding to the frequency range 3-18 Hz are 800-40 nm.

$La_{0.7}Sr_{0.3}MnO_3$ films were also deposited on both $SrTiO_3$ and $DyScO_3$. Unlike $SrRuO_3$, $La_{0.7}Sr_{0.3}MnO_3$ growth dynamics are not particularly sensitive to the termination of the substrate piece and layer by layer growth was achieved with parameters of 600 °C, 0.15 mbar, 5 Hz, 0.4-0.5 J/cm^2 and 55 mm. Deposition rates for those two fluences were 0.6 Å/s and 1.8 Å/s. Layer by layer growth was obtained in all cases.

The $La_{0.7}Sr_{0.3}MnO_3$ and $SrRuO_3$ targets used in this work were stoichiometric and supplied by Praxair Inc. (USA).

3.10 Device fabrication

3.10.1 Patterning devices

Electrode deposition using a shadow mask

The simplest way of fabricating regular electrode patches is by simply placing a shadow mask on the sample surface and depositing a conductive metal layer directly. TEM grids with square grid patterns are commercially available with hole sizes as small as 7.5 μm and bar widths as low as 5 μm. By simply mounting one of these on the sample surface and using it as a shadow mask, patterned electrode patches could be conveniently obtained. In this work, capacitor devices were square and had side length in the range 40-200 μm.

Photolithography and patterning of oxide electrodes

In some cases conventional UV lithography was used to pattern devices. Using this method, devices of any shape (minimum feature size of 1 μm) can be fabricated. In the photolithography process used here, the sample was first spin coated with negative photoresist (AZ5214E, Microchemicals) and baked. Next, the sample was exposed to UV light through a photomask, which is a transparent slide with opaque regions that make up the device pattern. This step was followed

by another bake before the whole sample was exposed to UV light again. After these steps are complete the sample is held in developer (Microposit MF-319, Shipley) then rinsed in water and blown dry. With negative-type photoresist the portion of negative photoresist that is exposed to the UV light becomes insoluble in the photoresist developer and remains even after all the unexposed photoresist is removed by the developer solution. Where the reverse pattern than is on the photomask is wanted, it is possible to use the same process but develop immediately after the first exposure. In this case, the regions with negative photoresist which are exposed to UV light are preferentially removed. After photolithograhy it is possible to pattern devices by using "lift off" or by etching. In lift-off, after photolithography a metal layer is deposited everywhere, the sample is placed in acetone, which removes the photoresist and the material deposited on it, leaving only the metal layer deposited directly on the sample behind.

After removing the photoresist from regions where it is not wanted using developer, a thin organic layer still remains on the exposed sample surface. This layer is detrimental to the adhesion of certain metals, especially Pt, which is notorious for having poor adhesion when deposited by e-beam evaporation. A short plasma ashing step immediately before electrode deposition was found to result in electrodes that proved well adhered, even when in very thin layers (few nm) and under ultrasound cleaning. This helped avoid the need for oxide electrodes or an adhesion layer in many parts of this work.

In contrast to lift-off, it is also possible to use patterned photoresist as an unreactive protective template when etching away certain materials in order to form devices. The $La_{0.7}Sr_{0.3}MnO_3$ devices used in Chapter 6 were fabricated by patterning photoresist on the sample surface then etching in a dilute solution of hydrogen peroxide and sulphuric acid [110]. Specifically the recipe used was to first make a stock solution of 50 ml of DI water + 25 ml H_2O_2 (30%) + 0.25 ml H_2SO_4(98%), then take 1 ml of this and add it to 99 ml of DI water. That solution was found to etch $La_{0.7}Sr_{0.3}MnO_3$ at a rate of approximately 1 nm/s. Although not used for the devices which data is presented for in this thesis, it is of note to add here that it is possible to similarly pattern $SrRuO_3$ with a similar etching rate using a 0.2 M solution of aqueous $NaIO_4$. This result is consistent with what is reported by Weber et al. [125]. This etchant did not significantly etch underlying $BiFeO_3$, $DyScO_3$ or $SrTiO_3$ layers.

3.10.2 Metal deposition

DC sputtering

DC sputtering is another form of physical vapour deposition where a metallic target is bombarded with ionised gas molecules (often Ar) causing atoms to be sputtered off into the plasma. These vaporised atoms then condense as a thin film on the substrate. The gas molecules are ionised by applying a large DC voltage (typically -2 to -5 kV) to the target and deposition pressures are typically in the range 10^{-2}-10^{-1} mbar. This technique was used to deposit the Pt electrodes in Chapter 4.

Electron beam evaporation

Electron beam evaporation is a form of physical vapour deposition in which an electron beam bombards metallic target in a vacuum chamber. The energy imparted to the target causes atoms to transform into a gaseous phase which then precipitates on any surface it comes into contact with, resulting in a thin coating. Deposition rates for Au and Pt electrodes were 2.5 Å/s and 0.2-0.5 Å/s respectively. were used for the Pt electrodes used here. Deposition rate and layer thickness was monitored and controlled during deposition using a quartz crystal growth rate monitor. The thin (<20 nm) layers of Pt deposited using this method gave a route to obtaining electrodes which almost perfectly conserved the surface morphology of the films they were deposited on. The explanation for this is that in electron beam evaporation deposition the effective temperature of the metal is very high, enabling it to be grow epitaxially at the low deposition rates used here. The extremely high quality of these electrodes enabled the advanced AFM investigation carried out in Chapter 6 without needing to use oxide top electrodes, which are harder to make a good electrical contact to using either a metallic probe or a metal coated AFM tip. The Au electrodes used for the photovoltaic characterisation in Chapter 8 were also deposited using this method.

Chapter 4

Domain wall motion in $PbZr_{0.2}Ti_{0.8}O_3$

4.1 Introduction

It is well known that domain wall motion, particularly domain wall jump, significantly contributes to the dielectric response of polycrystalline and ceramic Pb(Zr,Ti)O_3 [126–129]. In order to tune the behaviour of devices it is essential to have a good understanding of how domain walls are affected by and conversely affect the lattice. Despite many experimental and theoretical studies of the dynamical behaviour of domain walls, the actual mechanisms of domain wall motion and the energies associated with those processes are not well understood [130]. Here the contributions of both reversible and irreversible domain wall motion and the presence of domain walls and a domain structure in the lattice on the dielectric response of two epitaxial (001) oriented PZT/SRO/STO films with different $PbZr_{0.2}Ti_{0.8}O_3$ layer thickness are compared, using the framework of the hyperbolic law [89]. The first film is partially relaxed and shows large amount of a domains (polarisation entirely in-plane) in the c domain matrix (polarisation entirely out-of-plane). Ferroelastic 90° domain walls separate these domains. The second film is fully strained and shows only c-domains. The contributions from the effect of domain walls on the lattice and the domain wall motion have been thoroughly studied. Further to this, by treating the depinning of domain walls as a thermally activated process, the activation energy for domain wall depinning has been directly measured for the ferroelastic 90° domain walls in the 20/80 composition of Pb(Zr,Ti)O_3.

4.2 Sample details

The two films studied here were deposited by PLD in identical deposition conditions. Circular Pt electrodes with radius 160 μm were deposited by RF sputtering through a shadow mask on both samples in order to form metal-insulator-metal capacitor structures. The composition $PbZr_{0.2}Ti_{0.8}O_3$ was selected as it has an in-plane lattice parameter (3.935 Å) which is well matched to that of $SrRuO_3$ (3.928 Å) [131]. Detailed microstructural investigations of films from the same growth series are presented in Ref. [131].

4.3 PFM and ferroelectric characterisation

The PFM characterisation of the 100 nm and 60 nm thick $PbZr_{0.2}Ti_{0.8}O_3$ films studied here is shown in Fig. 4.1.

It can be seen that both samples have a smooth surface, indicating good epitaxial growth. The 100 nm sample consists of roughly 40% a-domains in a c-domain matrix. 90° domain walls separate these domains. This polydomain structure emerges as a way of minimising the total strain energy. In contrast the 60 nm sample is essentially monodomain which indicates it is fully strained [131].

Ferroelectric hysteresis loop characterisation of both samples is shown in Fig. 4.2. Measurements were carried out at 300 K with an aixaCCT TF2000E ferroelectric tester using a triangular waveform at a frequency of 25 kHz. This frequency was chosen to reduce the contribution of leakage. No leakage subtraction was carried out on the current trace before integration.

It is clear from the figure that the coercive fields for the 100 nm sample (-270 and +240 kV/cm) are much smaller than those of the 60 nm film (-820 and +790 kV/cm). This is consistent with similar films of the same composition [132, 133], and shows that the thicker film is more easily polarised. The saturation polarisation for both samples is similar (95 $\mu C/cm^2$), and this too is consistent with similar films in the literature. Both hysteresis loops have a square shape, which is typical of a hard ferroelectric. This is to be expected for this composition of $Pb(Zr,Ti)O_3$. It is of note that the 60 nm sample has a larger leakage contribution, causing and a less sharp polarisation loop. Two possible causes of this are i) a higher defect density (notably threading dislocations) and ii) the effect of polarisation on Schottky barrier heights. Conduction in these samples follows the Schottky-Simmons conduction mechanism and in this description both of these effects matter [134].

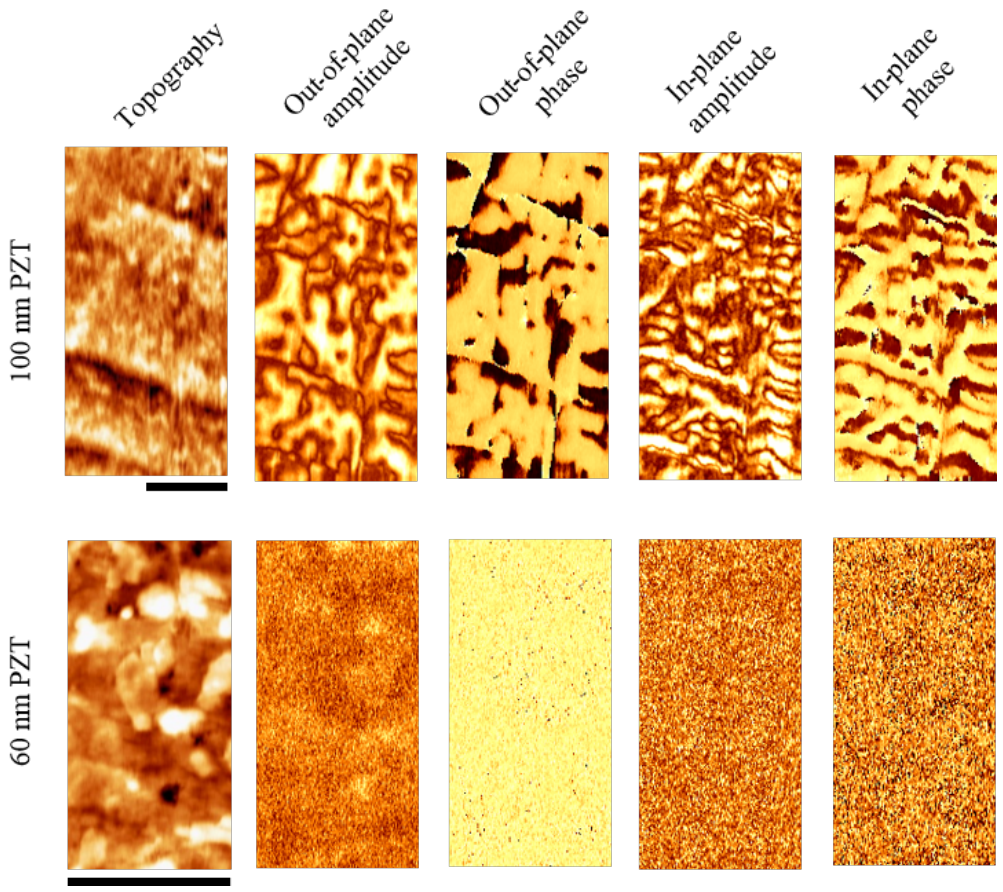

Figure 4.1: PFM characterisation both samples. The scale bars are both 0.5 μm in length. Data was collected at an AC voltage of 2 V and frequency of 22.36 kHz.

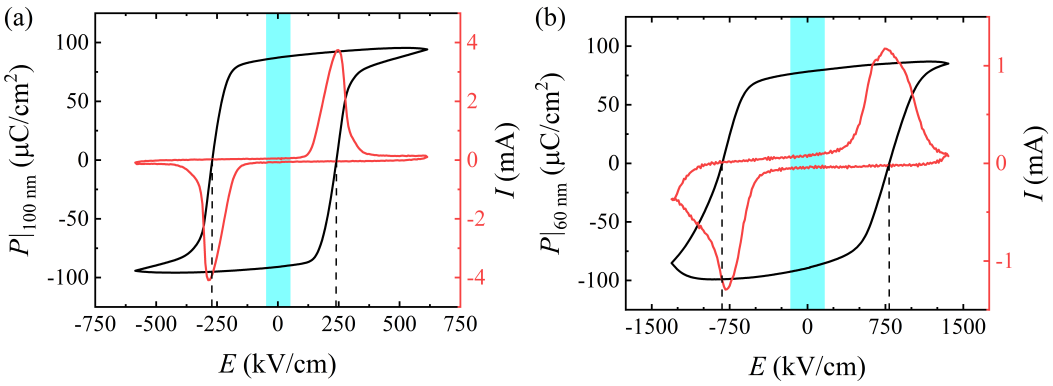

Figure 4.2: Ferroelectric hysteresis loops measured with a triangular waveform at 25 kHz for the (a) 100 nm and (b) 60 nm films. The cyan filled regions show the range of AC fields used for the dielectric measurements presented later here. Coercive fields are indicated by dashed lines.

4.4 Standard dielectric characterisation

Dielectric characterisation of both samples was carried out using an Agilent 4294A impedance analyser at six different temperatures (300 K to 400 K in 20 K steps). At each temperature the capacitance C_P and loss tangent tan(δ) were recorded for various AC driving field amplitudes E_0 ($< E_c/2$ in all cases) and frequencies f (100 Hz to 1 MHz). Real and imaginary parts of dielectric permittivity were calculated using Eqn. 3.2 and Eqn. 3.3. In this section the overall dielectric response of both samples is presented, then the individual contributions to both the real and imaginary parts of dielectric permittivity are extracted using the hyperbolic law, i.e. Eqn. 3.11. This enables the role of domain walls to be investigated in detail.

Care was taken to work in the regime where domain wall density is constant, i.e. the Rayleigh region [135–138]. The hyperbolic law fitting was carried out manually and data that were not well fitted with Eqn. 3.11 were not included in further analysis. When data is not clearly hyperbolic or is noisy the error bar on the fitting parameters ε_{rl} and ε_{r-rev} is large. The main source of noise in these experiments is from the interference of 50 Hz electrical noise associated with the power supply. As would be expected, this is is an issue at low frequencies only. The error bars shown from Fig. 4.4 are calculated directly from the least squares fitting of the various contributions to permittivity.

The dependence of real and imaginary parts of relative permittivity on electric field and frequency for both samples is shown in Fig. 4.3.

From Fig. 4.3(a) it can be seen that $\varepsilon_r'|_{100\text{ nm}} > \varepsilon_r'|_{60\text{ nm}}$. This is expected as the domain walls present in the 100 nm sample enhance the permittivity [131, 139]. The permittivity of the 60 nm sample can be taken as that of the bulk due to the low domain wall contribution there [140]. The origin of the greater variation in permittivity with electric field for the 100 nm sample is likely to the greater contribution of domain wall jump to permittivity in that sample, however it is also possible that the presence of domain walls in the thicker film make the lattice inherently more polarisable. Interestingly the value of E_0 where the linear Raleigh law well describes the behaviour, i.e. where domain wall jump is significant, is much higher for the 60 nm film than the 100 nm film. This indicates that perhaps in this sample the thinner sample the domain walls are more pinned. It is not possible to say from this plot alone whether that is due to an increased defect density in the sample or the depth of the individual defects. At high E_0, $\varepsilon_r'|_{100\text{ nm}}$ can be seen to decrease from linearity. This deviation indicates that at these fields some domain

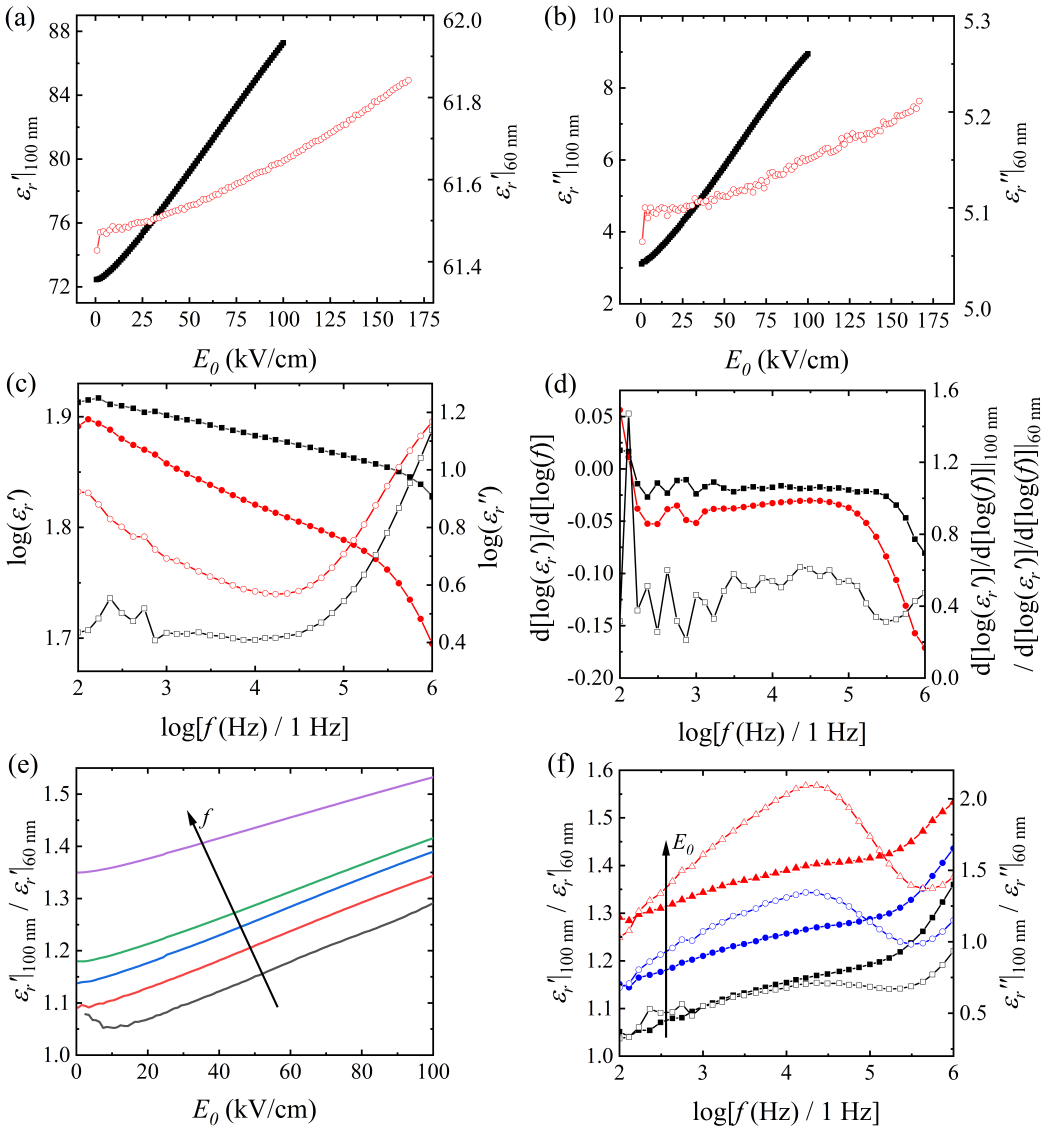

Figure 4.3: (a)-(b) Dependence of relative permittivity on AC electric field amplitude at 10 kHz and 300 K. (c)-(d) Frequency dependence of relative permittivity and its first derivative. (e) Electric field amplitude dependence of the ratios of relative permittivity for each sample at frequencies of 100 Hz, 1 kHz, 10 kHz, 100 kHz and 1 MHz. (f) Frequency dependence of the ratios of relative for each sample at electric field amplitudes of 10 kV/cm, 50 kV/cm and 100 kV/cm. For all plots black squares are used to represent the 100 nm sample and red circles used to represent the 60 nm sample. Solid points indicate the left y-axis should be used and whereas hollow points indicate the right y-axis should be used. All data in this figure was collected at 300 K.

coalescence occurs. This is associated with the onset of switching and decreases the density of domain walls. For this reason, the upper limit of E_0 for the hyperbolic law analysis was set as 50 kV/cm for the 100 nm sample. For the 60 nm sample the full range of E_0 values were used as deviation from the Rayleigh law regime was not seen at any measured frequency in that range.

Fig. 4.3(b) takes a similar form to From Fig. 4.3(a), but it is of note that $\varepsilon_r''|_{60\text{ nm}}$ is comparably high. Often the energy loss in ferroelectric capacitors is dominated by the contribution from domain walls [139], but here it appears this is not the dominant effect. It is likely that the energy loss in the 60 nm sample is high due to a different, more defective, microstructural defect structures caused by the film being less relaxed than the 100 nm film. Equally, it is likely that the energy loss in the 100 nm film is lower than has previously been reported for polycrystalline Pb(Zr,Ti)O_3 films due to the relatively large domain size resulting in minimal interactions between domain walls. These interactions are known to enhance permittivity [139]

Fig. 4.3(c) shows that we are in a relatively uniform part of the dielectric permittivity spectrum, however above 10^5 Hz the contribution to permittivity from dipolar relaxation clearly decreases [14]. As a result, in the following hyperbolic law analysis data collected above 10^5 Hz should likely be included, as this effect makes it impossible to conclusively extract the domain wall contribution. It is important that the hyperbolic law analysis is carried out in a frequency range where the effect of the applied AC electric field is the only cause of permittivity variation during a measurement. It is also of note that the data below 10^3 Hz suffers from some noise. This should be kept in mind in the subsequent analysis. Carrying out sensitive electrical measurements at frequencies close to that of mains power is experimentally challenging. The data quality for $f > 10^3$ Hz data quality appears to be much better. In this part of the dielectric permittivity spectrum it is often possible to describe the variation of permittivity with frequency by power laws (which appear linear on a log-log plot). Although it looks like this is possible for both samples between 10^3 and 10^5 Hz, it is not valid as the exponents would be different for the real and imaginary parts. This is forbidden by the Kramers-Kronig relations. It is also interesting that $\varepsilon_r'|_{100\text{ nm}}$ decreases more steadily than $\varepsilon_r'|_{60\text{ nm}}$ as a function of frequency. This indicates that 100 nm sample clearly retains its polarisability more effectively than the 60 nm film as frequency is increased.

Fig. 4.3(d) shows that between 10^3 and 10^5 Hz a power law would be a good fit for real part of permittivity for both samples, but the due to Kramers-Kronig relations applying the constraint that exponents must match it is clearly not

appropriate here [141].

Figure 4.3(e) shows that at higher f, the 100 nm sample is more polarisable than the 60 nm sample. This effect could be due to the effect of domain walls on the lattice or the direct contribution from domain wall motion. This effect is true even in the range where the dipolar contribution to permittivity is decreasing, which looks to be at a similar f in both samples. Further to this, Fig. 4.4(f) shows that the amount by which it is more polarisable increases at higher E_0, and at low f, the effect of increasing E_0 is stronger. Interestingly there is a peak in $\varepsilon_r''|_{100\text{ nm}}/\varepsilon_r''|_{60\text{ nm}}$ at around 10^4 Hz. This frequency does not depend on E_0, but the strength of it does increase at higher E_0. This suggests this increase in energy dissipation in the 100 nm compared to the 60 nm sample sample originates from electric field driven domain wall motion, as opposed to being from the lattice.

In conclusion, from this data we can justify going on to apply the hyperbolic law to decompose the data of ε_r into the lattice contribution and domain wall motion contributions is justified for both samples in the frequency range measured. Carrying out this analysis should enable the effects of domain walls on each sample to be studied in more detail than is possible from either the data in Fig. 4.4 or from the classical linear Rayleigh law description alone.

4.5 Hyperbolic law characterisation

In this section using the framework of the hyperbolic law [89] the contributions to the complex permittivity from both the the lattice and domain wall motion (vibration and jump) has been extracted for each sample for the same for a range of temperatures and frequencies. From these quantities associated losses have been calculated in addition to the threshold field marking the transition to the regime where domain wall motion is dominated by vibration to the regime where it is dominated by jump. Interestingly, the temperature dependence of this threshold field has been found to be similar for both samples and is well described as a simple thermally activated process. This has enabled an activation energy, which in this case is the energy to depin a domain wall, to be calculated for each sample and the results are consistent for both samples and with theoretical predictions in the literature.

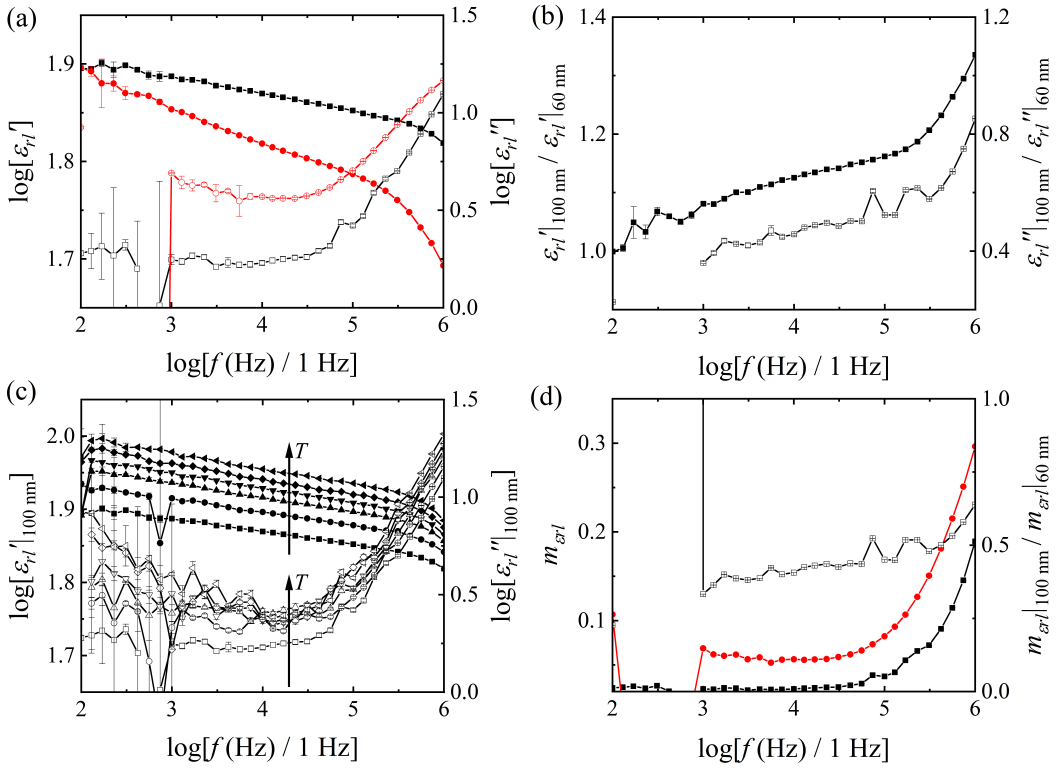

Figure 4.4: (a)-(d) Frequency dependence of the lattice contribution to relative permittivity, and its associated loss tangent. For (c), the temperatures data is shown for are 300 K, 320 K, 340 K, 360 K, 380 K and 400 K. Black squares are used to represent the 100 nm sample and red circles used to represent the 60 nm sample. Solid points indicate the left y-axis should be used and whereas hollow points indicate the right y-axis should be used.

4.5.1 The lattice contribution ε_{rl}

The first contribution which will discussed in detail is that of the lattice. This contribution, which includes polar phonon and electron contributions as well as the effect of static domain walls on the lattice, is expected to dominate in the epitaxial thin films studied here [135, 136]. It is worth noting that in some polycrystalline ferroelectric perovskite oxide thin films the domain wall motion does in fact dominate over the lattice contribution, but that is not the case in high quality epitaxial thin films. It is perhaps intuitive that due to the small volume of domain walls it is to be expected that the largest contribution to permittivity comes from the lattice. The temperature and frequency dependence of ε_{rl} and the loss tangent $m_{\varepsilon r}l$ and it and all related parameters is presented in Fig. 4.4.

It is clear Fig. 4.4(a) takes a very similar form to Fig. 4.3(c). This is as as

expected and indicates that the lattice contribution to permittivity is indeed the main contribution, however because the domain wall motion components are excluded from the data shown in Fig. 4.4 it is possible to make more specific conclusions. The origin of the enhanced value of ε_r' for the 100 nm sample can now be determined to be from the effect of having static domain walls and a polydomain structure in the lattice. The effect of this is to make the sample more readily polarised and hence have a higher relative permittivity. The origin of the lower decrease in permittivity with frequency for the 100 nm is the same. Additionally, the higher energy dissipation from the lattice contribution is higher for the 60 nm sample. It is likely that the origin of this is the different microstructural defect structure, because if it were from the static contribution of domain walls, i.e. domain walls providing defect sites, the energy loss in the 100 nm sample would be greater than in the 60 nm sample. Similarly to as for the case for Fig. 4.3(c) it is inappropriate to fit a power law to the linear parts of Fig. 4.4(a) as the gradients would be different for the real and imaginary parts, and that is forbidden by the Kramers-Kronig relations. It is of note that like in Fig. 4.3(c) the deviation from the behaviour that it appears to be well fitted by a power law comes at an earlier frequency for the imaginary part than the real part. This is associated with the decrease of the dipolar contribution to permittivity, which appears at 10^5 Hz. This is not a surprise and reinforces the earlier conclusion that in order to unambiguously extract the effect of domain walls it is necessary to exclude data above 10^5 Hz. Below 10^3 Hz the data is noisy due to some of the fits not converging. When this is the case data points are omitted.

From Fig. 4.4(b) it is clear that at low frequency the polarisability of the two samples is in fact very similar at low frequency. This means that in this regime the effect of static domain walls and the domain structure on the polarisability of the lattice is not significant. This becomes steadily and consistently more significant as frequency is increased. The same is not true of the ratio of energy losses, which in fact closest to 1 at higher frequencies.

Fig. 4.4(c) shows the influence of temperature on both real and imaginary parts of ε_{rl} for the 100 nm sample. It is to be expected that over this temperature range (well below T_C) the effect of increasing temperature is to enhance polarisability and also the energy loss. This trend is the same for all contributions the permittivity as well as for the total relative permittivity ε_r. For clarity for the rest of the investigations here only data for 300 K is shown.

Fig. 4.4(d) shows that the loss tangent is consistently roughly twice as large in the 60 nm sample. This ratio is not especially dependent on frequency in the range $10^3 - 10^5$ Hz. In ferroelectric capacitor devices it is normal for domain walls

make a capacitor less ideal by either productive conductive pathways or sites where it is energetically favourable for defects such as oxygen vacancies to accumulate. From the data for the two samples studied here it is apparent that this is not the dominant cause of energy loss. The cause of this is probably strain, which is not relieved in the thinner film. This will result in different defect structures in each film.

The conclusions to be taken from this component is that having domain walls and a-domain structure present in the lattice inherently makes the lattice more polarisable. This effect is distinct from that of domain wall motion.

4.5.2 The domain wall vibration contribution ε_{r-rev}

The contribution to permittivity from reversible domain wall vibration [135] often proves to be the most difficult one to extract from the hyperbolic law analysis, especially when the contribution from domain wall jump is not large. This is particularly true for the 60 nm film studied here and is clear from the functional form of the hyperbolic law: $\varepsilon_r = \varepsilon_{rl} + \sqrt{\varepsilon_{r-rev}^2 + \alpha_r E_0}$. The frequency dependence of ε_{r-rev} and its associated loss m_{r-rev} are shown in Fig. 4.5.

Fig. 4.5(a) clearly shows that the contribution to permittivity from domain wall vibration is higher in the 100 nm sample, and that there is not a clear frequency dependence in the range measured here. For the 100 nm sample the energy loss from from domain wall vibration does decrease with frequency. The same appears to be true also for the 60 nm sample, but that data does suffer from higher noise due to the low domain wall density. It is interesting that the effect of the decrease of the dipolar contribution to permittivity is is not particularly clear here. This is perhaps not surprising, as the presence of the decrease of the dipolar relaxation contribution to permittivity is not expected to affect domain wall motion.

Fig. 4.5(b) shows that $\varepsilon'_{r-rev}|_{100\text{ nm}}/\varepsilon'_{r-rev}|_{60\text{ nm}} \approx 4$. This is surprising given that from the PFM data it is clear that the difference in domain wall density in the two samples is much greater than four times. In contrast the ratio of energy losses $\varepsilon'_{r-rev}|_{100\text{ nm}}/\varepsilon'_{r-rev}|_{60\text{ nm}} \approx 8$. This value is higher, but still appears to be inconsistent where the PFM data which makes the 60 nm sample is demonstrated to have a monodomain.

Fig. 4.5(c) shows that the loss tangents for the domain wall vibration contribution are similar, however for the 100 nm sample it is slightly greater. In the Rayleigh region it is expected that there is no domain wall interaction, but that is not clearly the case here. It is of note that the difference is not significant: $m_{rev}|_{100\text{ nm}}/m_{rev}|_{60\text{ nm}} \approx 1.5$. The raw values at 10 kHz

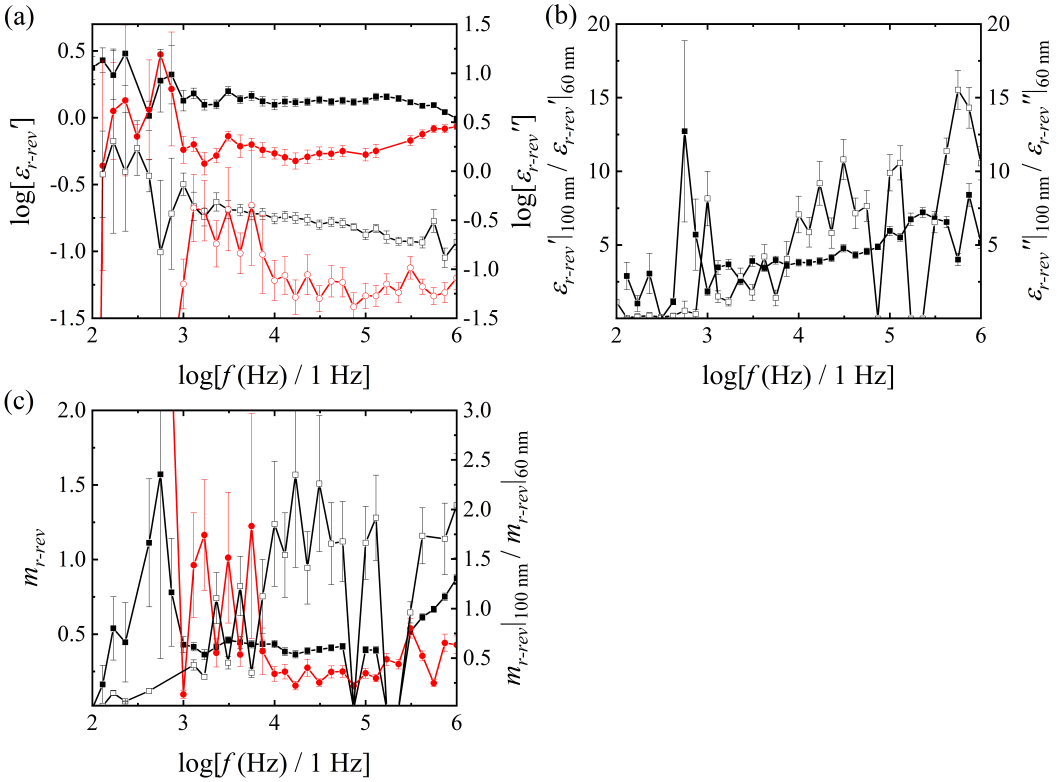

Figure 4.5: (a)-(c) Frequency dependence of the domain wall vibration contribution to relative permittivity, and its associated loss tangent.Black squares are used to represent the 100 nm sample and red circles used to represent the 60 nm sample. Solid points indicate the left y-axis should be used and whereas hollow points indicate the right y-axis should be used.

are $m_{rev}|_{100\text{ nm}} = 0.43, m_{rev}|_{60\text{ nm}} = 0.23$. These values are similar to those that reported in the literature for BST thin films [139, 142], which indicates the vibration of domain walls is a very dissipative phenomenon in general. For comparison at 10 kHz $m_{\varepsilon rl}|_{100\text{ nm}} = 0.023$ and $m_{\varepsilon rl}|_{60\text{ nm}} = 0.056$. No information on the m_{rev} values for Pb(Zr,Ti)O_3 have been reported in the literature. The ratio of loss tangents in both samples is similar, but is higher in the 100 nm sample. This could be due to interaction of domain walls, but is close to being within measurement error.

Two things can be concluded from this data. The first is that although the domain wall vibration contribution is greater in the 100 nm sample, the amount by which it is greater is far less than expected. The second is that the the domain wall vibration contribution to permittivity has been found to be far more dissipative than the lattice contribution, with loss tangents which are typically one order of magnitude higher.

4.5.3 The domain wall jump contribution $\alpha_r E_0$

As the contribution to permittivity from domain wall jump can be very large ($\approx 1 \times 10^{-5}$ m/V) in polycrystalline Pb(Zr,Ti)O_3 thin films and ceramics [143, 144] it is reasonable to expect based on the information in Fig. 4.4(a) that there is a large difference in the magnitude of this effect in the two films measured here. This is consistent with what is expected from the PFM characterisation. The frequency dependence of α_r and its associated tangent loss m_α is shown in 4.6.

From Fig. 4.6(a) it is clear that there is a large difference in domain wall jump coefficients for each of the two samples. The consistently higher values for the 100 nm sample are consistent with what is expected from the PFM characterisation. The frequency dependence of real and imaginary parts of α_r is weak and similar for both samples. As for the lattice contribution, the decrease with frequency is weaker for the 100 nm sample. Also, it comes as no surprise that the imaginary part of α_r, which represents the amount of energy loss associated with domain wall jump is significantly higher in the 100 nm sample. Despite again it looking possible to fit a power law to real and imaginary parts of α_r, this is not possible because the gradients of real and imaginary parts on the log-log plot (essentially the exponent for the power law) are different, and the Kramers-Kronig relations forbid this. The value of α_r in the 100 nm sample is around five times lower to that measured by Mangalam et al. for a similar film on $SrRuO_3$/$GdScO_3$ [33]. PFM characterisation of their sample reveals it contains a similar density of 90° domain walls, but due to the different substrate material and growth conditions it is reasonable to expect that their value for α_r will be slightly different, but within an order of magnitude.

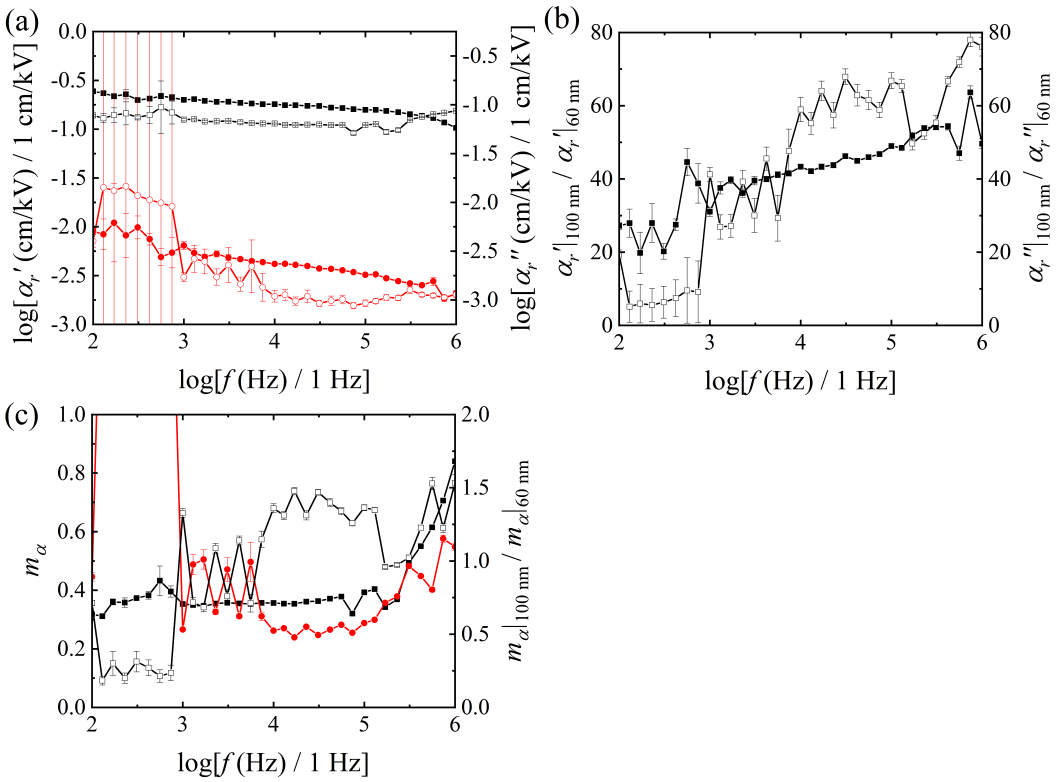

Figure 4.6: (a)-(c) Frequency dependence of the domain wall jump contribution to relative permittivity, and its associated loss tangent. Black squares are used to represent the 100 nm sample and red circles used to represent the 60 nm sample. Solid points indicate the left y-axis should be used and whereas hollow points indicate the right y-axis should be used.

It is worth noting that theoretical calculations by Li et al. have predicted that compressive/tensile strain has the effect of significantly increasing/decreasing the energy barrier for domain wall motion in both $PbTiO_3$ and $BaTiO_3$ [130]. It is therefore to be expected that the domain wall mobility is higher for the case of the sample of [33] on $GdScO_3$ than the samples with a slightly higher 90° domain wall density on $SrTiO_3$ studied here.

Fig. 4.6(b) shows frequency dependence of the ratio of real and imaginary parts of α_r. It is clear that the ratio of both real and imaginary parts is around 50, indicating that the amount of domain wall jump is higher by roughly that many times in 100 nm film. This is a significant difference and is consistent with the PFM data. According to Boser [90],

$$\alpha_r \propto \frac{f_0 P_s}{\sqrt{N F_1}} \varepsilon'_{r-rev}. \tag{4.1}$$

Here f_0 is a geometrical factor, P_s is saturation polarisation, N is the number of obstacles or defects, and F_1 is a function which is proportional to the pinning depth of the defect. As the two samples have the same orientation the polarization directions are the same, meaning both the factor f_0 and P_s will be very similar. This can be seen from the P-E loops (Fig. 2) where the remnant polarization is almost identical for both samples. The difference of the parameter α'_r hence will be due to the product NF_1. This indicates that the 100 nm, which has a much larger value for parameter α'_r, has a lower defect density and/or less deep defects.

From Fig. 4.6(c) it can be seen that despite the very different domain wall densities, the loss tangents for domain wall jump are similar in both samples, but are perhaps slightly higher for the 100 nm film. This slight increase may be due to a small amount of domain wall interaction. The values for m_α at 10 kHz of $m_\alpha|_{100\text{ nm}} = 0.36$ and $m_\alpha|_{60\text{ nm}} = 0.26$ are similar to the values for m_{r-rev}, indicating that domain wall jump and domain wall vibration are similarly dissipative processes in $Pb(Zr,Ti)O_3$ films in this frequency range. There is no obvious frequency dependence. The dissipation parameters m_α are lower than those reported for $Pb(Zr,Ti)O_3$ thin films ($m_\alpha \approx 0.42$) [128, 145, 146]. This might be due to the lower domain wall density in the two samples studied here, as a higher density favours increased domain wall interaction and hence a higher dissipation factor [139]. The similarity of the dissipation factors calculated for the samples in this work indicates that the dissipation due to domain wall motion is not strongly related to domain wall density.

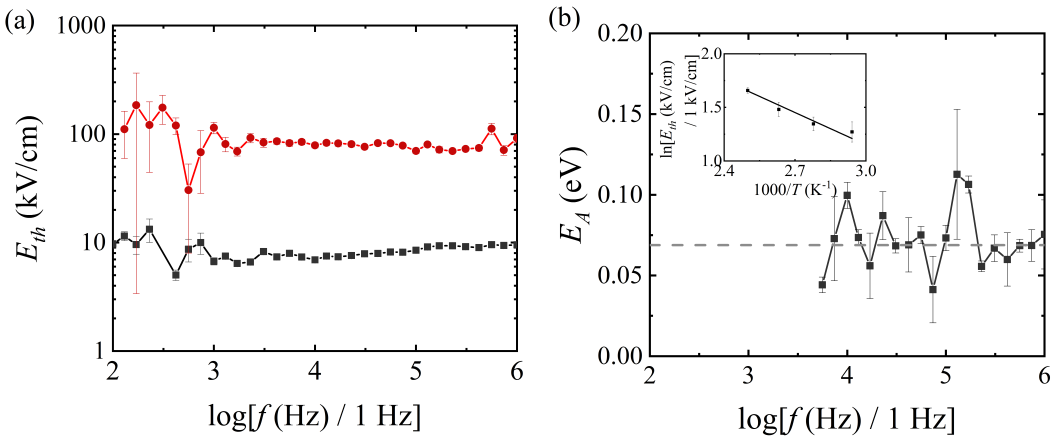

Figure 4.7: Frequency dependence of (a) threshold field at 300 K and (b) activation energy for electric field driven domain wall depinning for E_0=10 kV/cm The inset on (b) shows the Arrhenius plot used to calculate activation energy. Black squares are used to represent the 100 nm sample and red circles used to represent the 60 nm sample.

4.5.4 The threshold field E_{th}

The threshold field E_{th} is defined to be the electric field amplitude at which the domain wall motion is dominated by domain wall jump as opposed to domain wall vibration. Below this field domain walls are pinned. At or above it most have sufficient energy to depin or equivalently jump. This field is defined as $E_{th} = \alpha'_r/\varepsilon'_{r-rev}$. Interestingly the temperature dependence of this can be described as a simple thermally activated process and an activation energy calculated. This depinning energy is interestingly consistent with a recent theoretical prediction for the amount of energy it takes to depin a 180° domain wall from an oxygen vacancy in $PbTiO_3$, which is chemically and structurally similar to the composition of $Pb(Zr,Ti)O_3$ selected here.

From Fig. 4.7(a) it is clear that the threshold field for the 60 nm sample (83 kV/cm) is much higher than that for the 100 nm sample (7.5 kV/cm). This is in line with what can be predicted based on the data in Fig. 4.3(a), the magnitudes of the domain wall motion coefficients ε_{r-rev} and α_r for each sample, and also the hysteresis loops shown in Fig. 4.2. In addition, the frequencies measured here there is no significant variation of E_{th}. This can be seen from the threshold field for domain wall pinning/unpinning. According to Boser [90], the ratio between the

coercive field and the threshold field is equal to:

$$\frac{E_c}{E_{th}} = \frac{2}{\sqrt{\pi}}\sqrt{\ln\frac{L_3}{2L_0}} \tag{4.2}$$

where L_3 is the average distance between two domain walls and L_0 is the distance between two points where domain wall velocity is zero when an AC excitation voltage is applied. Here the ratio $\frac{E_c}{E_{th}}$ is equal to 90 and 33 for the 60 nm and 100 nm samples respectively, which is very high compared to the value $E_c/E_{th} \approx 2.2$ obtained by Boser [90]. This indicates that the distance between domain walls is apparently so large in the samples here that there is actually no interaction between them, i.e. the domain wall motion is not influenced by the domain wall density here. The consequence of this is that it possible to exclude domain wall interactions as the cause of the slight difference in loss tangents for the domain wall motion contributions to relative permittivity.

Fig. 4.7(b) shows the result of describing temperature dependence of threshold field as a simple thermally activated process. Threshold field values were obtained from graphs of the same form as Fig. 4.7(a) but taken at higher temperatures, in conjunction with the data of Fig. 4.7. The simple thermally activated model used has the standard form

$$E_{th} = Ae^{-E_D/k_BT} \tag{4.3}$$

where A is an amplitude factor, E_D is the energy to depin a domain wall from a typical defect, and k_B is Boltzmann's constant. The inset shows the linear dependence of a the logarithm of threshold field as a function of inverse temperature on a typical Arrhenius plot. The linearity of the data justifies the application of this model. For the 100 nm sample the calculated depinning energy E_D is 70$\pm$10 meV.

4.5.5 Discussion of the value of threshold field

In order to sensibly discuss this result in context it is helpful to introduce the historical perspective. In 1954, Merz found that the domain wall propagation speed in $BaTiO_3$ single crystals is proportional to $e^{-2E_A/E}$ [147]. E_A is the "activation field" and E is the electric field experienced at the domain wall. This relation is called Merz's law and is a classical result.

In more recent years experimental values of the activation field have been determined by Tybell et al. [148] using an AFM based method. Here they applied voltage pulses to a conductive AFM tip in contact with monodomain $Pb(Zr,Ti)O_3$

(001) thin films (deposited by rf magnetron sputtering) and imaged the size of the resulting domains using PFM. By applying pulses of different duration and amplitude to films of different thickness they found the domain wall speed in their samples was well described as a creep process of the form $v \propto e^{\frac{R}{k_B T}[\frac{E_0}{E}]^{\mu}}$. Here the exponent μ is equal to 1 and the effective activation energy $[R/k_B T]^{1/\mu} E_0$ was found to be 1320, 1300, and 500 kV/cm for the 29, 37 and 81 nm thick films they measured. These values of field are consistent with values of around 800 kV/cm (at 300 K) and 3200 kV/cm (at 200 K)for $PbTiO_3$ obtained by molecular dynamics simulations by Shin et al. [149], however they are in disagreement with the values obtained by Meyer and Vanderbilt using the nucleation model based on the domain wall energy of $PbTiO_3$ [150]. For comparison, the coercive and threshold fields found for the 60 nm monodomain film measured here are 750 kV/cm and 83 kV/cm respectively. It is worth noting here that the activation field for domain wall motion for AFM based measurements is likely to be quite different to that of the measurements presented here which use in a parallel plate capacitor geometry. This is because the electric field distribution in AFM measurements is much more inhomogeneous. This said, it is reasonable to expect that the domain wall motion in our case is likely well described by creep at low field with an additional contribution from domain wall motion at higher field. Also it is likely that the defect structure in the films used in the AFM studies (deposited by rf magnetron sputtering) is quite different to in the films studied here (deposited by PLD). More recently a number of experimental studies of domain wall dynamics have been completed using TEM [151, 152], but in these domain wall speed and domain wall motion barriers have not been systematically studied.

It is surprising given the intense interest in domain wall dynamics that the AFM based technique is the only method that has been used in recent years to experimentally quantify values for the activation field associated with domain wall motion, and it is of note that the values it yields are not in agreement with those from simulation. In reality the motion of domain walls is affected by various lattice defects which interrupt the periodic potential of the crystal lattice. It is well known that ferroelectric failure (such as imprint and fatigue) originates from domain wall pinning as lattice defects, especially oxygen vacancies [153–156]. In light of this, it is reasonable to expect that the depinning E_D extracted from the hyperbolic law analysis is related to the energy required to depin a domain wall from an defect, most likely an oxygen vacancy or an accumulation of oxygen vacancies, in the lattice.

A number of studies using density functional theory (DFT) methods have

been used to calculate the energy barrier for domain wall motion, both in an ideal lattice and a lattice with defects. These are useful guides, but when considering the quantitative results from these studies it is important to keep in mind the limitations of this approach. DFT is a useful tool but is fundamentally limited by the size of the supercell it considers and its assumption of periodic boundary conditions. Particularly when it comes to modelling the macroscopic effects of defects, the inhomogeneity of their distribution is important. This is incompatible with DFT simulations using a small supercell and periodic boundary conditions. This said, it is informative to consider the values obtained using various DFT methods for barriers to domain wall motion.

He and Vanderbilt [154] calculate that oxygen vacancies find it favourable to migrate into 180° domain walls in $PbTiO_3$, and once they do they experience a binding energy to the domain wall of between 100 and 250 meV. This is the energy that needs to be input to depin a domain wall from a single vacancy. It is also worth noting that thin films produced by PLD are often off-stoichiometric. It is reasonable to expect that the most common type of defect in these films are oxygen vacancies, however other types of defect, such as lead-oxygen divacancies, are also predicted. The lead deficiency of the films studied here is expected to be smaller than the oxygen deficiency due to the excess lead used in the targets. The distribution of vacancies is not necessarily isotropic, and it is at times favourable for defects to aggregate. It is not simple to build this effect into DFT simulations due to the necessity of having to use periodic boundary conditions.

Chandrasekaran et al. [157] calculated the energy barrier to motion of a 180° domain wall in pure $PbTiO_3$ in the presence of various defects. The energy cost of moving one of these domain walls a distance of one unit cell in an ideal lattice calculated to be around 120 meV. In the presence of defects, depending on the type of defect, they calculate that its value changes by around a factor of two.

Most recently, Li et al. [130] calculated the depth of the potential well a 180° would experience if it were on top of a single oxygen vacancy in $PbTiO_3$ to be around 300 meV. This amount of energy would need to be put input to the system to depin the domain wall. This is the exact process that the energy E_D corresponds to. In addition, they found the energy cost of moving a 180° domain wall across half a unit cell of an ideal lattice to be around 30 meV. It is also of note that Li et al. also calculate that compressive strain can act to significantly increase the energy barrier for domain wall motion [130]. This is in contrast to tensile strain, which has the effect of decreasing it. Even though the strain of the sample the value of E_D is obtained for here is relatively small, a strain of -0.5% would result in an

enhancement of the energy barrier by a factor of around 1.5.

There are two different energy costs that need to be considered here. The cost of moving a domain wall the distance of one unit cell in an ideal lattice, and the cost of depinning the domain wall from any defect it is located on. Using another result from Meyer and Vanderbilt [150], that the domain wall energy for 90° domain walls is around one quarter of that of 180° domain walls in $PbTiO_3$, it can be concluded that the barrier for motion of the 90° domain walls in the $PbZr_{0.2}Ti_{0.8}O_3$ films studied here is likely significantly less than the obtained value for threshold field. The dominant contribution to the value of 70±10 meV will originate from the depinning of the domain wall from defects. Because of this, the value for E_{th} presented here can be considered as an estimate amount of energy it takes to depin a domain wall from an average defect in the sample measured, whether it be a point defect or an extended defect. Despite the limitations of the DFT simulations, it is of interest that the experimentally determined value obtained here is reasonably consistent (same order of magnitude) with predictions from theoretical works. This enables us to make the conclusion that this experimental approach employed here may yield a new and useful way to measure the barriers to domain wall motion in this system and similar systems, but further work likely involving NMR, EPR, and TEM is needed to properly determine and understand the defect structure. This information is required to fully interpret the value of E_D obtained here and discuss it in context.

4.6 Chapter summary

Here it has been demonstrated that PFM and dielectric characterisation are complementary methods which together provide a more complete understanding of the dynamical behaviour of domain wall motion in this system than has been previously possible. The hyperbolic law has been shown to be an appropriate framework to analyse the system studied here and the frequency and temperature dependence of the motion of 90° domain walls to the dielectric permittivity have been systematically studied. Interestingly, the temperature dependence of the threshold field has been found to be well described as a simple thermally activated process, enabling the activation energy to depin a domain wall to be calculated. The value obtained, 70 ± 10 meV, is consistent with theoretical predictions.

Chapter 5

Ferroelectric switching and domain wall functionality in $BiFeO_3$

5.1 Introduction

$BiFeO_3$ has been extensively studied in the last decade and is one of the most promising multiferroic materials. Due to its room temperature multiferroicity and photovoltaic effect it has several applications in the fields of magnetism, spintronics and photovoltaics. One specific field which it is of particular interest to is non-volatile information storage. Recent work on this topic by Sharma et al. [158], Bai et al. [13] and Jiang et al. [12] has demonstrated that it is possible to manufacture prototype ferroelectric domain wall memory devices which are compatible with the requirements of industry. In these devices the conductive $BiFeO_3$ domain walls are the active element, as opposed to the electric polarisation. This work lifts the conductive domain walls in $BiFeO_3$ from being an interesting feature from a fundamental physics perspective to being of serious interest for future technological application. As a result it is now more important than ever to develop a complete understanding of domain wall properties.

The aims of the work presented in this chapter are as follows:

1. to study the switching behaviour in these devices. This has not been studied before for two variant 71° stripe domain $BiFeO_3$ samples in a capacitor device geometry, and

2. to correlate the domain wall structure in devices in different switching states

with the electronic behaviour of devices, with the aim of elucidating existing reports of transport and magnetotransport measurements of domain walls in $BiFeO_3$.

The methods employed to do achieve these aims are through-electrode PFM and standard variable-temperature transport measurements.

5.2 Additional background

There have been relatively few studies on domain wall transport and magnetotransport. The first of these was that of He et al. [159], but this work has several issues. In this work a significant magnetoresistance originating from 109° domain walls at temperatures below 200 K and fields up to 7 T was reported. The claimed magnetoresistance was large (up to -70% at 7 T at 10 K) when both magnetic field and transport are aligned with the 109° stripe domain pattern. For the two perpendicular geometries there is no magnetoresistive response. These measurements have not been reproduced and doubt over their veracity is cast by the fact that magnetoresistance measurement presented consisted of a single sweep from 0 to 7 T, as opposed to tracing out a loop by sweeping from 0 to 7 T to -7 T to 0. It is not clear that the data presented is not just current drift. In addition, the conductivity in the geometry where current runs parallel to the 109° domain walls is seen to be essentially temperature independent below 200 K. Again, this is not consistent with the findings of any other group for 109° stripe domain $BiFeO_3$. The next study was that of Lee et al. [160] which reports an anisotropic magnetoresistance at domain walls in 1% Li doped $BiFeO_3$ films on SRO/STO. These measurements were on films with irregular 'as-grown' domain patterns consisting of 71°, 109° and 180° domain walls. An out-of-plane capacitor device geometry was used. They showed that the low temperature conductivity of the capacitor devices was greatest in the half switched state (where domain wall density is highest), that the transport is well described as thermally activated above 100 K and governed by variable range hopping below 100 K, and that the current from the domain walls shows a marked unidirectional anisotropic response when magnetic field is applied. This latter observation is ascribed to the coupling of ferromagnetic domain walls to antiferromagnetic domains. Despite showing interesting results there are two main limitations to this study. Firstly the lengths and orientations of each type of domain wall in devices at different stages of switching are not known. Secondly the sample studied exhibits a disordered domain pattern to start with meaning that switching will not be repeatable within the device. The effect

of this is that the observed effects cannot be assigned to any particular type of domain wall, let alone quantified particularly accurately. Most recently Domingo et al. [121] measured the room temperature magnetoresistance of individual 71° domain walls using C-AFM. In that study the orientation of 71° domain walls was found to determine the sign of the magnetoresistance, meaning that macroscopically averaged measurements of samples containing of many domain variants and domain wall types and orientations are at risk of averaging away some of the contributions and underestimating the contributions from specific domain walls.

There have been more studies on how ferroelectric switching proceeds in $BiFeO_3$ [72, 161, 162], but the full picture of how it proceeds in mesoscopic capacitor devices is not fully understood. For $(001)_{pc}$ $BiFeO_3$ it has been found that the most favourable switching pathway consists of a single 71° step. There is no detailed study of how ferroelectric switching proceeds in capacitor devices with an initial $BiFeO_3$ layer consisting of 71° stripe domains. It is reasonable to predict that the switching across a region with an initial 71° domain wall will consist of two 71° steps (one as polarisation in each domain is flipped). In this picture, using the notation of Streiffer [31] and Fig. 2.8(a), there will be a significant proportion of 109° domain walls in the partially switched state. The switching would be from r_3^- and r_4^- to r_3^+ and r_4^+. This model would be consistent with the recent study by Yang et al. [163] which finds that C-AFM measurements with a sufficiently high applied voltage create up-polarized nano-domains and 109° domain walls at the interface between as-grown 71° stripe domains. One particularly interesting study by Johann et al. showed that the switching process in $BiFeO_3$ capacitor structures with as-grown 71° stripe domain patterns is repeatable upon cycling, so long as the cycling frequency is not greater than around 1 kHz [164, 165], but this work does not study the switching behaviour. After the first 500 cycles or so the stripe width increases and the regular domain structure is stable up to at least 10000 cycles. There are a number of points to raise from this study though. Firstly, the sample measured in this work does not completely switch. Secondly, despite having relatively regular stripe domains, the sample used has a morphology which is associated with a layer plus island growth mode. In addition there are many pinholes. These inhomogeneities are expected to provide sites where domains pin and nucleate upon cycling which ultimately will compromise the repeatability. Also in order to image the domain pattern with PFM the Cu electrodes were chemically removed. This unfortunately had the effect of switching some of the ferroelectric polarisation. The effect on the in-plane polarisation component was particularly

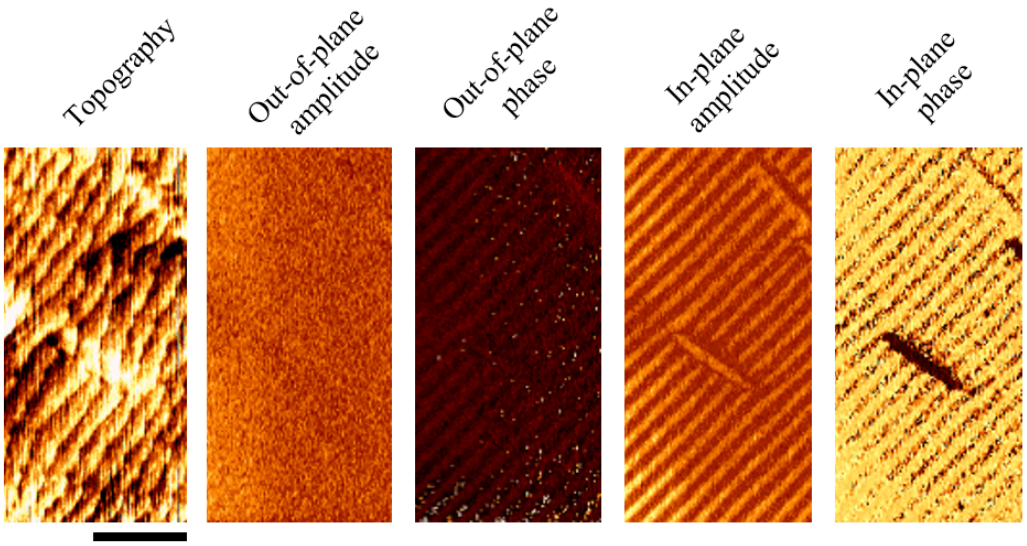

Figure 5.1: PFM characterisation of the BFO/SRO/DSO sample measured here. The scale bar is 1 μm. For these scans an AC voltage of 1.5 V was applied to the tip at a frequency of 22.36 kHz. The steps in the topography image are 1 u.c. in height.

significant. Measurements where PFM was carried out through a top electrode did not yield good quality in-plane information there due to the smearing effect of the top electrode and the crosstalk from the out-of-plane component dominating the in-plane signal.

5.3 Sample details

The sample selected for this work is a BFO/SRO/DSO film. The $BiFeO_3$ and $SrRuO_3$ layer thicknesses are 100 nm and 8 nm respectively. The sample was phase pure under XRD and layer thicknesses were calculated from Laue fringes about the $(001)_{pc}$ Bragg reflections. PFM characterisation for this sample is shown in Fig. 5.1. The as-grown domain structure consists of regular 71° stripe domains with polarisation pointing down. Two of the stripe domain variants dominate, which is as expected because of the anisotropic in-plane strain applied by the $DyScO_3(110)_o$ growth surface and underlying orthorhombic $SrRuO_3$ layer. This is similar to the sample used by Johann et al. [165]. The topography shows the film has grown in the step flow growth mode and that the surface is pinhole free. This suggests that there are few topographical features which could provide pinning sites which disrupt the domain structure during the switching process.

The $BiFeO_3$ films used for which data is presented here were cooled at a rate

of 20 °C/min in 5 mbar O_2 atmosphere. This was done to attempt to enhance the conductivity at the domain walls – cooling at slower rates in higher oxygen pressures results in less conductive samples as there are fewer oxygen vacancies.

5.4 Domain evolution during ferroelectric switching

Through-electrode PFM was used to study the evolution of the domain structure within the device as a function of the switching state. This is different to the method of Johann et al. [165], where a chemical method was used to remove their Cu top electrodes before imaging with PFM. They found that when top electrode was removed the etchant would preferentially switch the exposed area of the $BiFeO_3$ film such that the polarisation was pointing down. For this reason that method is not appropriate for studying the domain pattern in partially switched devices. Capacitor devices were fabricated by depositing square platinum electrodes of thickness 3 nm and side length 60 μm. These electrodes were deposited by e-beam evaporation at a slow deposition rate of 0.3 Å/s. The Pt surface was seen by AFM to perfectly conserve the $BiFeO_3$ surface morphology. The edge of a capacitor device on a sample in the same growth series is shown in Fig. 5.2. The error signal image shows the difference between the measured tip position and the set point of the AFM tip assigned by the controller. In practice, this image can be considered to be an approximation of the first derivative of the topography image with respect to height. The cause of the difference in $BiFeO_3$ surface morphology between Fig. 5.1 and Fig 5.2 is the miscut angle of the substrate. Both these films clearly grew in a 2d growth mode, however in the case of Fig. 5.2 the miscut angle was sufficiently low that incident atoms were not given time to migrate to step edges like in a true step-flow growth mode. As a result islands can be seen to have nucleated on step terraces, with one unit cell high steps.

Pt was chosen as the top electrode here for three reasons. Firstly it is known to make a good rectifying contact with $BiFeO_3$, enabling accurate electrical measurements of the switching to be made. Secondly when deposited slowly by e-beam evaporation it is possible to deposit layers which perfectly conserve the $BiFeO_3$ surface morphology, unlike Au for example. Finally, it has a relatively high stiffness (Young's modulus = 168 GPa) compared to other commonly used metal electrodes such as Au (78 GPa) and Cu (130 GPa). The effect of this is that the thin Pt electrodes used here mask the surface piezoresponse less than the thicker non-epitaxial electrodes used in other studies. In principle oxide electrodes such as $SrRuO_3$ or $(La_{0.7}Sr_{0.3})MnO_3$ would be a better choice due to their higher stiffness,

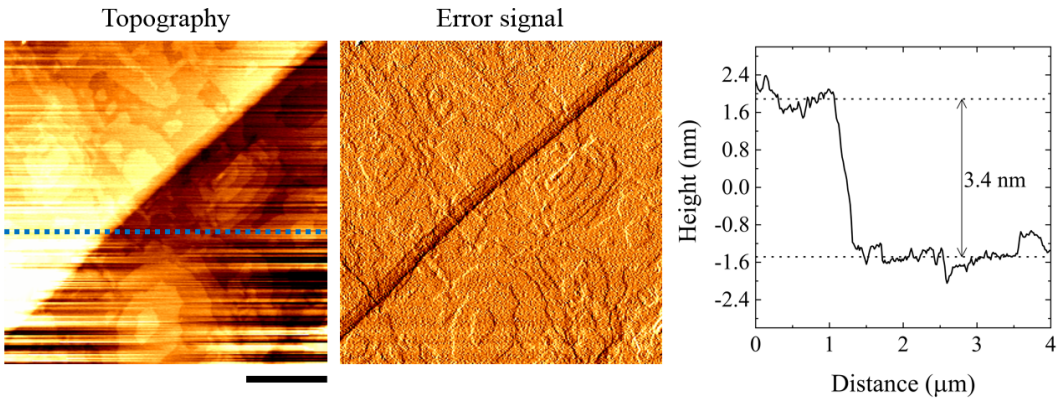

Figure 5.2: AFM scan over the edge of a capacitor device. Left: AFM topography. Middle: Error signal. Right: Line profile along blue dotted line. The scale bar is 1 μm.

but these were not used here as i) it was found that they were difficult to contact well with a metal probe needle and ii) the fabrication process required a chemical etching or Ar milling step.

In order to make a stable electrical contact to the top electrode while the surface piezoresponse is probed with the AFM tip a home-made setup consisting of a tungsten probe needle mounted on a micromanipulator was added to the AFM sample stage. The AC voltage was applied from the probe needle to the top electrode and the bottom electrode was grounded. The needle was connected to a pulse generator (AFG3102C, Tektronix) which allows arbitrary pulse sequences to be applied. This setup proved to be more electrically stable than the alternative case without a needle where the AC voltage is applied through the tip, but measurements with tip only are still possible. Fig. 5.3 shows a large area scan where the as-grown domain structure is imaged both through a top electrode and on the bare surface.

Pt electrodes are at the top left and bottom right corners of this scan area. The central region shows the as-grown domain pattern. The morphology and domain structure for this sample are consistent with those shown in Fig. 5.1. This is the sample for which electrical measurements are presented later. Similarly to Fig. 5.2, it is clear that surface morphology is conserved after deposition of Pt. The out-of-plane PFM is clearly dominated by the small patches of up polarised domains, despite the small crosstalk from the in-plane component. The amplitude of the piezoresponse is larger for the regions with the top electrode than the as-grown surface. This due to the different distributions of electric field the sample experiences when the tip scans and electrically contacts these regions. When scanning an electrode the whole device area is effectively electrically contacted.

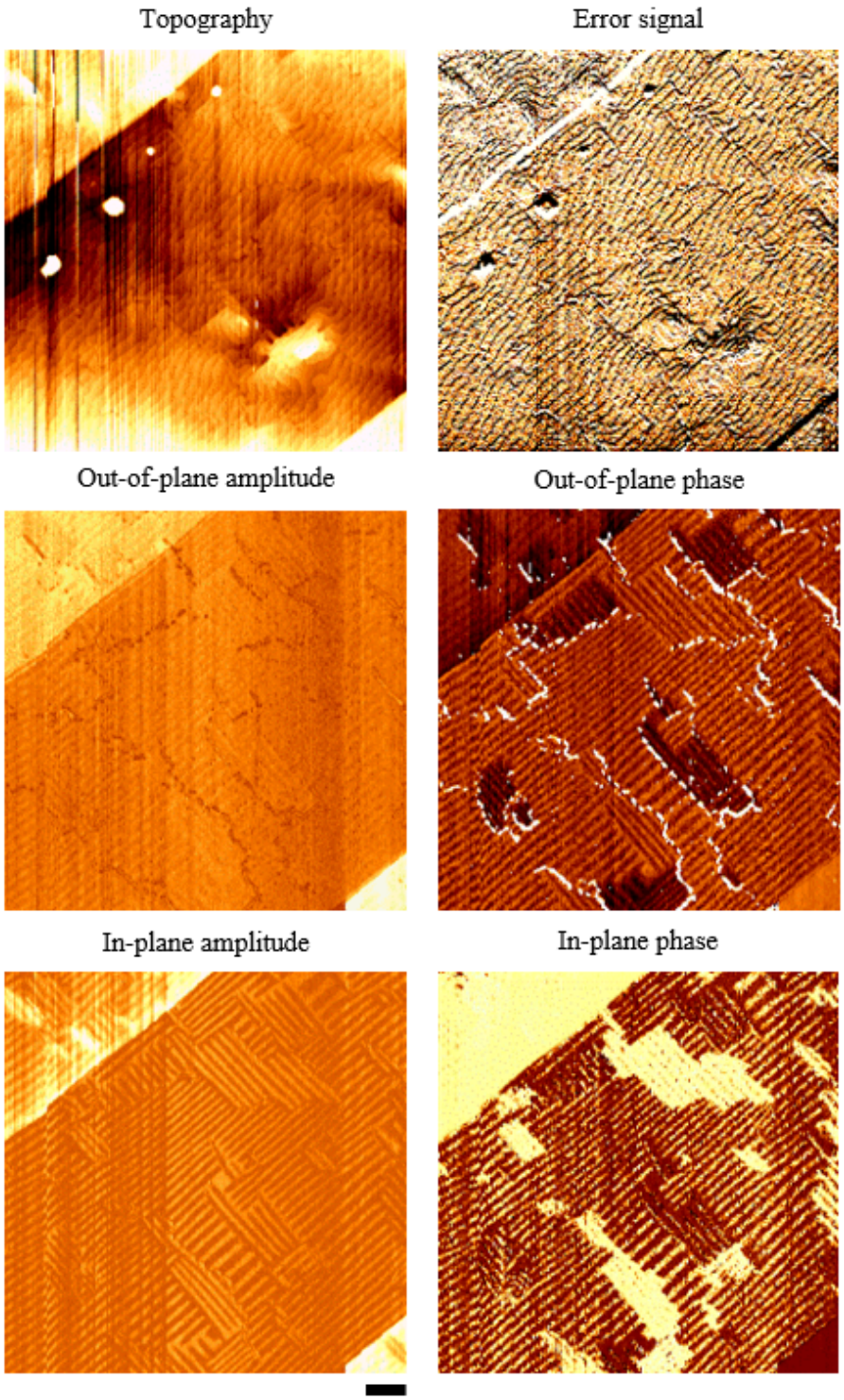

Figure 5.3: PFM characterisation of the BFO/SRO/DSO sample measured here. The scale bar is 1 μm. For these scans an AC voltage of 1.5 V was applied to the tip at a frequency of 22.36 kHz.

In contrast, when scanning the as-grown surface the AFM tip essentially acts as a point source. This measurement is consistent with that of Johann et al. [165]. The small up polarised domains are clearly visible in both the out-of-plane phase and amplitude PFM data. These are removed by cycling [164]. It is clear here that the in-plane PFM image is relatively clear and not dominated by cross talk. The in-plane amplitude image clearly shows the 71° stripe domain structure. This is in contrast to the work of Johann et al. [165] who found it impossible to reliably carry out in-plane PFM measurements through their top electrodes due to the smearing effect of the top electrode and crosstalk from the out-of-plane component of the piezoresponse. The reason why it is possible to obtain the in-plane information here lies with the electrode choice. Johann et al. used thicker (10-30 nm) Cu electrodes which were deposited by thermal evaporation. Despite having perfectly good electrical properties, these electrodes are less favourable for this type of PFM measurement than the high quality epitaxial Pt electrodes used here.

In order to investigate how the ferroelectric switching proceeds it is necessary to controllably be able to put the device into partially switched states. To do this unipolar triangular waveforms of various amplitudes and 400 μs duration were applied. Switching was performed additively with no reset pulses applied in order to watch switching cycles sequence in the same area proceed in a stepwise manner. This is the same method Lee et al. [160] used to change the domain structure in their study. Through-electrode PFM data from two different devices on the same sample are shown in Fig. 5.4 and Fig.5.5. Scan areas are all 10×10 μm^2.

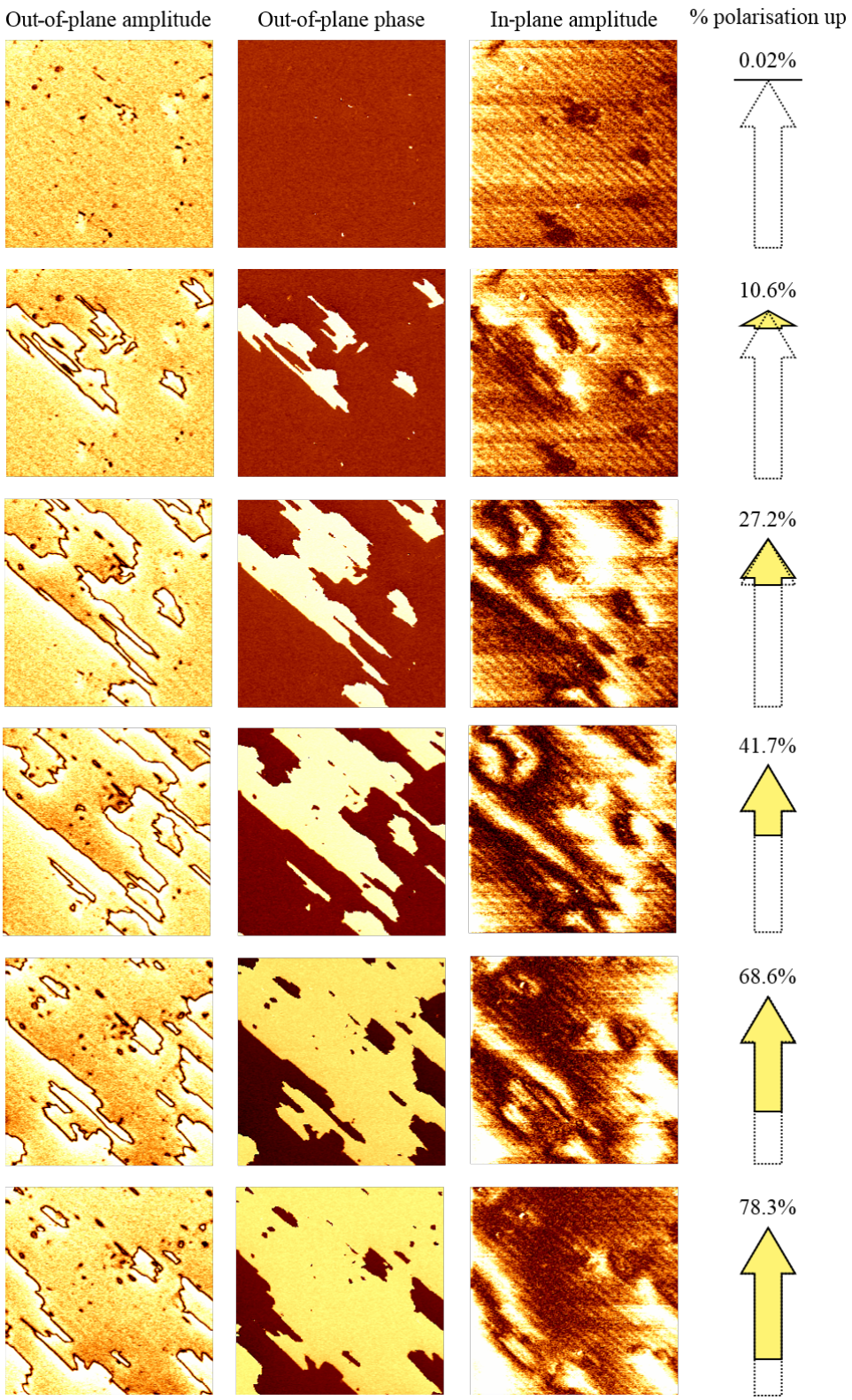
Out-of-plane amplitude
Out-of-plane phase
In-plane amplitude
% polarisation up
0.02%
10.6%
27.2%
41.7%
68.6%
78.3%

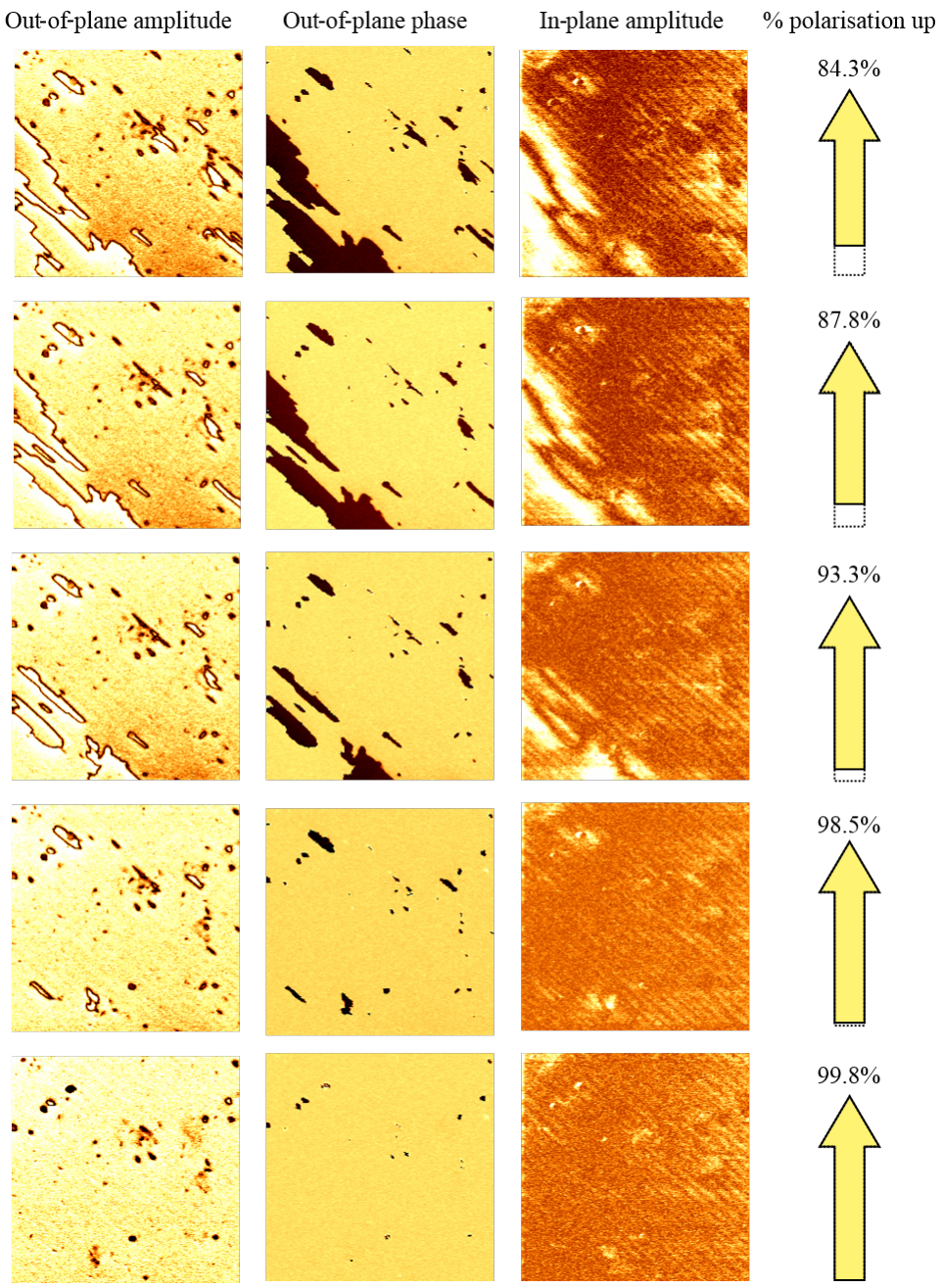

Figure 5.4: Domain structure of a capacitor device 1 measured by through electrode PFM. The polarisation is incrementally switched from a down state (top row) to an up state (bottom row) through successive application of voltage pulses. The cartoon arrow indicates the proportion of the device with polarisation oriented upwards. For these scans an AC voltage of 1 V was applied to the tip at a frequency of 22.36 kHz.

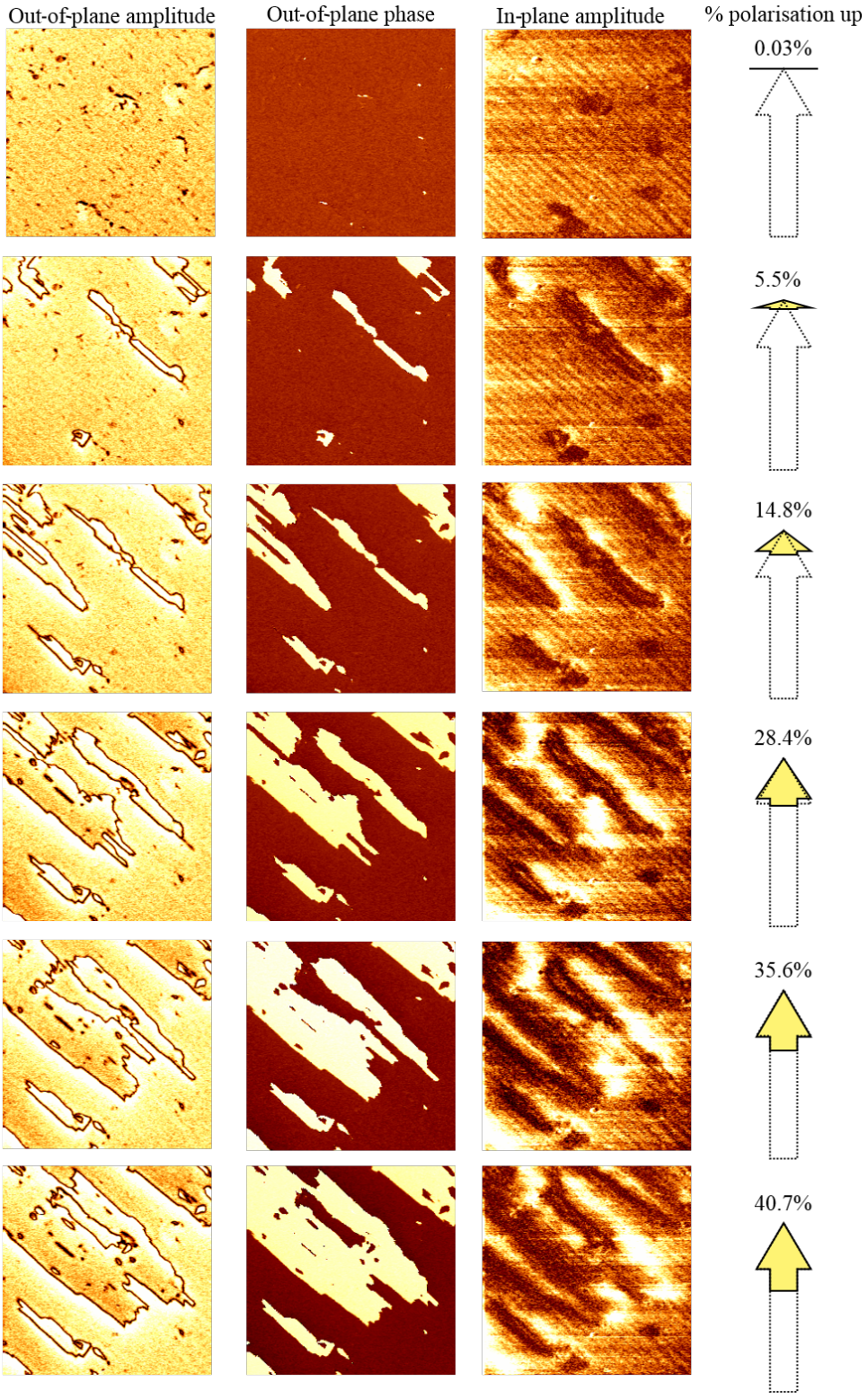
Out-of-plane amplitude
Out-of-plane phase
In-plane amplitude
% polarisation up
0.03%
5.5%
14.8%
28.4%
35.6%
40.7%

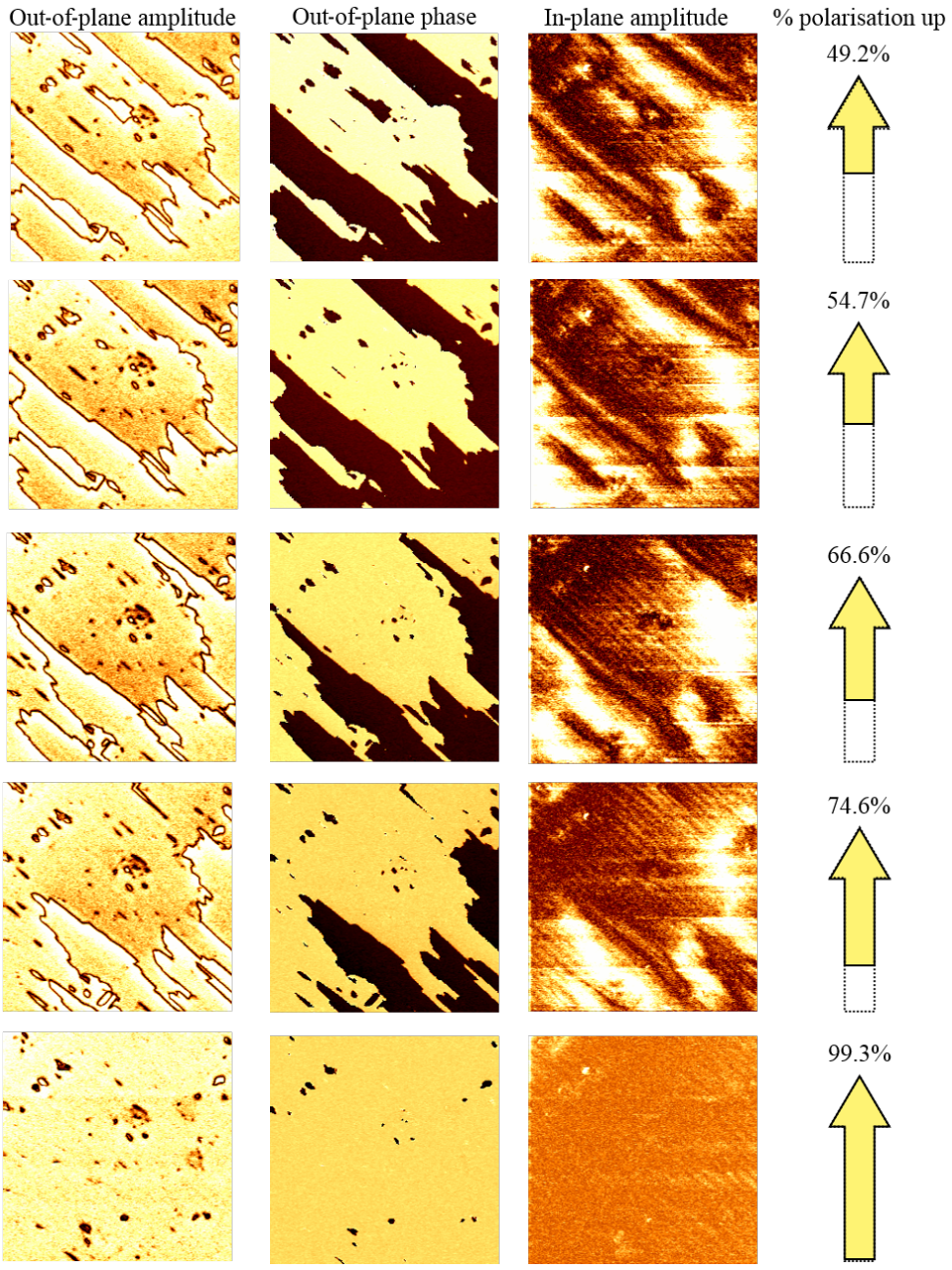

Figure 5.5: Domain structure of capacitor device 2 measured by through electrode PFM. The polarisation is incrementally switched from a down state (top row) to an up state (bottom row) through successive application of voltage pulses. The cartoon arrow indicates the proportion of the device with polarisation oriented upwards. For these scans an AC voltage of 1 V was applied to the tip at a frequency of 22.36 kHz.

From these measurements it is possible to make the following observations:

1. the 71° stripe domain pattern is conserved even after repeated cycling, which is consistent with the result of Johann et al. [164],
2. the alignment of the 71° stripe domains improved after some initial cycling, so it effectively consists of two variants only. Again, this is consistent with the observations of Johann et al. [164],
3. the density of the small out-of-plane domains in the as-grown domain pattern is decreased after some initial cycling,
4. the switching seems to proceed by 109° domains forming at 71° domain boundaries. This is consistent with the observation of Yang et al. [163] in their purely AFM based study. Formed 109° domains proceed to grow preferentially along the direction of as-grown 71° stripe domains but do broaden in both directions,
5. the out-of-plane polarisation in this device is at least 99.8% switchable. This value is calculated from the out-of-plane phase image shown in Fig. 5.5 k), and
6. the density of 71° domain walls is roughly constant throughout the switching process, but the density of 109° domain walls is significant in the partially switched state.

From the data shown in Fig. 5.4 and Fig. 5.5 the length of the different types of domain walls can be calculated. The length of 109° domain walls was calculated from the out-of-plane phase images as the length of the boundaries between areas with polarisation pointing down and areas with polarisation pointing up. The length of 71° domain walls was calculated from the in-plane amplitude images by tracing the length of the clearly visible stripe domain walls. The result of this analysis is shown in Fig. 5.6. It is clear that the switching behaviour for both device 1 and device 2 is very similar. Because of this it is possible to say that the AFM scans presented in Fig. 5.4 and Fig. 5.5 are sufficiently large that they provide a representative picture of what is happening across the much larger device area. This data seems somewhat skewed with the maximum length occurring when the device is around 60% switched. This may be a result of the asymmetry of the Pt/BFO/SRO/DSO device, but equally the skew is small and could reasonably lie within experimental uncertainty. The same can be said of the wider scatter in the series of data from device 2.

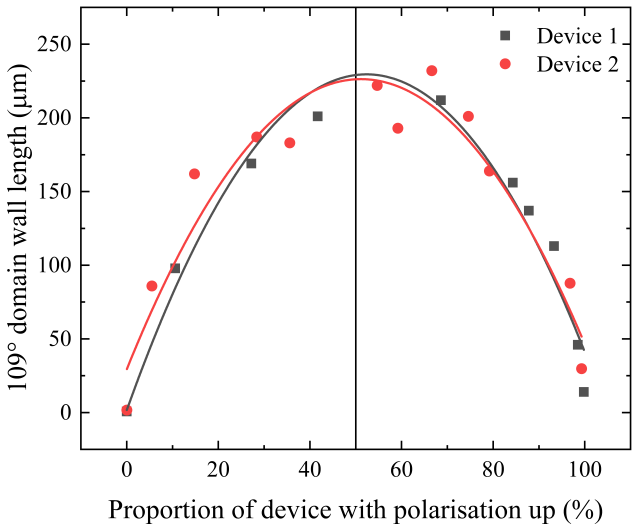

Figure 5.6: Length of 109° domain walls in the scanned region at different stages of switching. Second order polynomial fits are added as a guide for the eye.

From the data presented in this section it is demonstrated the switching mechanism in $BiFeO_3$ capacitor devices with an initial two variant 71° structure follows a similar mechanism to that observed by Yang et al. [163]. 109° domain walls are nucleated at 71° domain boundaries. These grow preferentially along the direction of the as-grown stripe domains, and the 71° stripe domains are essentially flipped upwards by this process. The 71° stripe domain pattern is conserved even as the polarisation is flipped, and is robust to cycling. Through electrode PFM is demonstrated to be an appropriate and valid method by which both the in-plane and out-of-plane domain structure information can be obtained for ferroelectric materials such as $BiFeO_3$ with complex domain architectures.

5.5 Electrical characterisation

Given the evolution of the domain pattern in this sample is now understood it is now possible to study the electrical behaviour of the device and relate that to the domain structures present.

Electrical characterisation was carried out at 80 K and 300 K using a cryongenic probe station (Lake Shore Cryotronics model PS-100). Top electrodes were contacted with a tungsten needle and all voltages were applied top to bottom. Hysteresis loop data was obtained using an aixACT TF2000E ferroelectric testing system with a triangular waveform of frequency 1 kHz. No corrections for leakage

were made. Devices were initially poled using a unipolar triangular voltage pulse with an amplitude above that of the coercive field, then unipolar triangular voltage pulses of the opposite sign and various amplitude were applied to put the device into a partially switched state. To calculate the switched polarisation the device was switched back, the current trace recorded, and the remnant polarisation calculated. To measure the steady state current through capacitor device in a given state, a small non-switching probe voltage was applied and the steady state current was measured using an electrometer (Keithley 6517A). Specifically, the current was recorded 20 s after the probe voltage was applied. This gave sufficient time for the current to stabilise but insufficient time for the probe voltage to measurably change the switching state of the device. It proved favourable to use a negative probe voltage when measuring the steady state current as due to the electrical asymmetry of the Pt/BFO/SRO/DSO device the leakage current was higher for that configuration. In order to exclude any effect of drift the series of pulse voltages V_{pulse} for which steady state current I_{ss} was measured was randomised. I.e. instead of measuring for a pulse voltage of 0 V first, then 0.3 V, then 0.6 V, then 0.9 V, until the largest V_{pulse} was reached, the measurement series was acquired with for example 1.5 V first, then 3.3 V, then 0.6 V, then 4.5 V, then 2.1 V, until all values of V_{pulse} in the predefined measurement series had been applied. This ensured that any drift in measured data was captured as random error rather than systematic error. The results of these experiments are shown in Fig. 5.7.

The asymmetry of the hysteresis loop at 300 K is clear. This non-ideality is actually favourable for this experiment as in order to measure a steady state current a certain amount of leakage is required. At 80 K this leakage is effectively eliminated. As the electrical transport mechanism in $BiFeO_3$ is understood to be thermally activated above 100 K this is exactly what is expected [160]. At lower temperatures the coercive fields are larger. This is because the crystal lattice experiences less thermal vibration and is therefore effectively stiffer. A larger electric field needs to be applied to flip the polarisation.

At room temperature the effective conductivity switches between two states as the ferroelectric polarisation is switched. The difference in conductivity of these two states is a factor of around 2.5. The behaviour here is dominated by resistive switching. It is striking how closely the values of steady state current correspond to the switching state of the device. In contrast, 80 K a peak in steady state current occurs, and this is coincident with the point at which the device is half switched. This is consistent with the behaviour observed by Lee et al. [160]. In that study it was found that below 100 K the electrical transport is dominated by

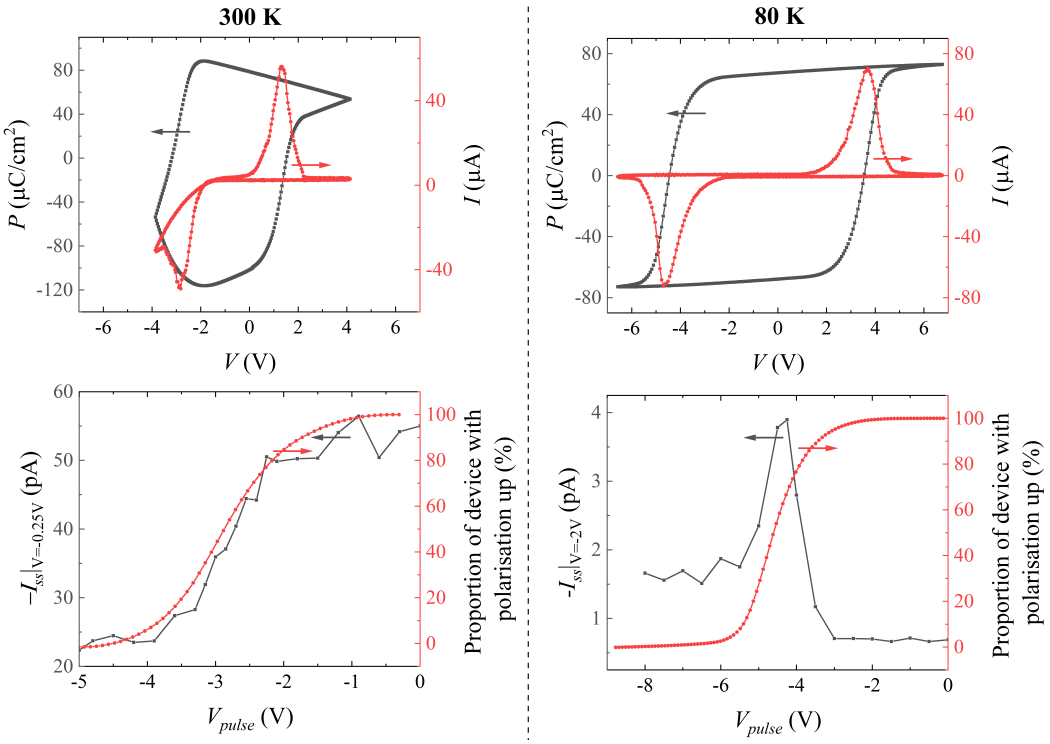

Figure 5.7: Ferroelectric hysteresis loop and steady state current measurements for Pt/BFO/SRO/DSO capacitor devices in various switching states at temperatures of 80 K and 300 K.

the conductivity of domain walls, as opposed to the bulk. The presence of the same peak here, indicating that conductivity is highest in the half switched state allows us to reinterpret the other data presented in that study with more clarity, given that we know the physics is the same in our case and theirs.

In fact, as it is known that the domain walls dominate the low temperature electrical transport it is possible to go further than this and directly evaluate the resistivity of each type of domain wall at the low temperature of 80 K. From the in-plane PFM is clear that during the switching the areas with switched polarisation contain 71° stripe domains with the same width as in unswitched regions. From measuring the 71° stripe domain width to be around 160 nm and assuming their width to be around 1.2 nm [166] it is possible to calculate that length of these domain walls present in the scanned area is around 630 μm and that their volume fraction is around 0.75%. For comparison, this is more than three times the maximum length of 109° domain walls, indicating that the 109° domain walls dominate the transport behaviour of the device, especially in the half switched state. The volume fraction of 109° domain walls in the device in different switching states can be similarly calculated by assuming a domain width of 0.8 nm [166]. Values for this parameter range from essentially zero up to a maximum of 0.15%. By simply setting the total resistivity of the device at 80 K equal to the sum of the contributions from each type of domain wall, and considering the difference in resistivity between two points the resistivity of each type of domain wall can be evaluated. In order to minimise the effect of any contribution from the polarisation dependence of Schottky barrier heights at the metal-ferroelectric interfaces it is best to consider a pair of measurements with similar V_{pulse} but notably different 109° domain wall lengths. The output of this relatively crude analysis is that at 80 K $\rho_{109} \approx 3\times10^6$ Ωcm and $\rho_{71} \approx 10 \times 10^6$ Ωcm. These values are consistent with those of Lee et al. who estimate that at this temperature the average resistivity of domain walls in their Li-doped sample is around 1×10^6 Ωcm. Unlike the measurement of Lee et al., the analysis here is able to discriminate between the contributions from the different domain wall variants because the length of each type of domain wall in the the devices under test here were evaluated in various switching states.

The data presented earlier showed that the density of 71° domain walls remains roughly constant throughout the switching process, unlike the density of intermediate 109° domain walls which changes significantly. As the peak in steady state current at 80 K emerges when the device is half switched this contribution can be directly assigned to the 109° domain walls. It has been demonstrated that domain walls dominate the electrical transport below 100 K [160], and given the

data obtained here is of the same form as that of Lee et al. [160] it seems very likely that the main cause of the low temperature conductivity in $BiFeO_3$ are these intermediary 109° domain walls, as opposed to 71° domain walls. Values for the conductivity of each type of domain wall have been calculated at a temperature of 80 K.

In light of the results here it is very likely that 109° domain walls are specifically responsible for the large enhancement of anisotropic magnetoresistance of the half-switched $BiFeO_3$ layer in the sample of Lee et al. [160]. Despite their sample being of much lower symmetry than the sample used here, i.e. the domain structure was irregular and all orientations of polarisation were present in the as-grown state, the crystallographic structure is similar. This means that it is more likely than not that the switching pathway for polarisation is the same in that sample as the one measured here, where 109° domain walls form at the boundaries between regions with polarisation aligned upwards on one side and downwards on the other. It will just proceed in a much more specially inhomogeneous way. The low temperature anisotropic magnetoresistance response in the sample of Lee et al. presents a strong hysteresis for devices in a half switched state [160]. This directly implies a net magnetic moment at domain walls. Despite this initially sounding like a bold claim this work follows earlier studies where it was found that the exchange bias interaction may be enhanced by increasing the proportion of 109° domain walls in a $BiFeO_3$ sample. In contrast, 71° domain wall structures had no effect on the exchange bias [167]. More recently theoretical work has predicted that both 71° and 109° domain walls carry a magnetisation in $BiFeO_3$ [168]. It is possible based on the observations here to conclude that the ferromagnetism associated with the magnetic moment of domain walls in the study of Lee et al. is specifically associated with the 109° domain walls which are present in the partially switched state, and not the 71° domain walls. The method employed here can be relatively simply extended to measurements in the presence of magnetic field and offer a pathway to probe domain wall behaviour in temperature regimes where it would otherwise be inaccessible due to the measured currents being too small.

5.6 Chapter summary

In the work presented here the evolution of the domain pattern in $BiFeO_3$ capacitor devices with an initial 2-variant 71° stripe domain pattern in various switching states has been determined for the first time and found to be repeatable. In the down and up states the domain pattern consists purely of 71° stripe domains.

In the half switched state 109° domain walls emerge, mostly at the boundaries of bundles of 71° domain walls. This is consistent with and extends the observations of the AFM based measurements of Yang et al. [163]. The length of 109° walls was found to be closely connected to the device conductivity and by the combination of PFM and electrical data the resistivity of each type of domain wall present was directly evaluate. The data here elucidates the conclusions of reports in the literature of the low temperature magnetotransport properties of domain walls and strongly suggests that the ferromagnetism associated with the magnetic moment of domain walls in the study of Lee et al. [160] are specifically associated with the 109°.

Further to this, the combination of methods used here is demonstrated to provide a pathway to probe domain wall behaviour in $BiFeO_3$ in temperature regimes where it would otherwise be inaccessible due to its insulating nature at low temperature.

Chapter 6

Real time ferroelectric switching in $BiFeO_3$

6.1 Introduction

One commercial application of ferroelectric materials is in non-volatile information storage. In ferroelectric random-access memory (FeRAM) devices the data bits 0 and 1 are stored in the form of the ferroelectric polarisation state either pointing up or down [27]. Despite development of this technology the switching properties and dynamics of polarisation reversal are still not yet fully understood. The fundamental properties in bulk materials may be studied by static characterisation methods [169, 170], but for devices on the nanometre scale the models used have to be modified [171]. The process of polarisation reversal in ferroelectric materials can be considered as consisting of three processes: domain nucleation, domain growth, and domain wall motion. In order to design devices on the nanometre scale a good understanding of the the coupled motion of charges, atoms and domain walls during electric field driven polarisation switching is required. In order to access this information it is necessary to investigate the time dependent behaviour. There have been a number of several structural and electrical investigations on this topic (with a focus on $Pb(Zr,Ti)O_3$) with nanosecond time resolution, but typically these studies focus on either the electrical [172] or structural [173] response. Measuring the charge flow associated with this process is relatively straightforward, using a PUND pulse sequence or similar to extract the displacement current associated with the ferroelectric switching. In contrast, it is more technically challenging to measure local structural changes in a time resolved manner. One method of doing this is with time-resolved x-ray

diffraction. It is only in the last couple of years that this method has been used in conjunction with electrical characterisation methods to simultaneously track the electrical and structural response of ferroelectric thin film capacitor devices with nanosecond resolution [174, 175]. In these recent studies the material studied was $PbZr_{0.2}Ti_{0.8}O_3$.

In this chapter detailed time resolved simultaneous measurements of the charge transport and structural response of $BiFeO_3$ during ferroelectric switching are presented. The aim of the investigations here are to determine the polarisation dynamics during ferroelectric switching.

6.2 Sample details and static characterisation

The three samples are used in this chapter are listed in table 6.2. Top electrodes on samples 1 and 3 are squares of side length 200 μm, realising metal-ferroelectric-metal capacitor devices. After growth films were cooled slowly at 5 °C/min in 500 mbar O_2 – this cooling procedure decreased the amount of DC leakage.

High resolution reciprocal space maps about the $(002)_{pc}$ Bragg reflections for samples 1 and 2 are shown in Fig. 6.1. The components of the reciprocal lattice vector q parallel to the film surface ($q_{\|}$) and perpendicular to the film surface, i.e. along the growth direction, ($q_{\perp}$) are clearly defined in Eqn. 3.16 and Eqn. 3.17.

In the RSM for sample 1 there are clear peaks from the $BiFeO_3$ (lowest $q_{\perp}$) and $DyScO_3$ (higher $q_{\perp}$), but the peak from $SrRuO_3$ (occurs at the highest $q_{\perp}$) is broad due to the low layer thickness

For sample 2 the $BiFeO_3$ peak (lowest $q_{\perp}$) is clearly split, which is as expected from vertical 109° domain walls [94, 176]. The $DyScO_3$ peak is also clear, and appears at a slightly higher $q_{\perp}$. The reflection from the $La_{0.7}Sr_{0.3}MnO_3$ layer very is clear here and appears at a $q_{\perp}$ of arond 3.28 $Å^{-1}$. The oscillations are Laue

ID	Top electrode	Ferroelectric	Bottom electrode	Substrate	Notes
1	Pt	$BiFeO_3$	$SrRuO_3$	$DyScO_3$	71° stripe
	30 nm	150 nm	8 nm		
2		$BiFeO_3$	$La_{0.7}Sr_{0.3}MnO_3$	$DyScO_3$	109° stripe
		300 nm	30 nm		
3	$La_{0.7}Sr_{0.3}MnO_3$	$BiFe_{0.95}Mn_{0.05}O_3$	$SrRuO_3$	$SrTiO_3$	71° stripe
	20 nm	150 nm	50 nm		

Table 6.1: Samples used for the time resolved ferroelectric switching measurements presented in this chapter.

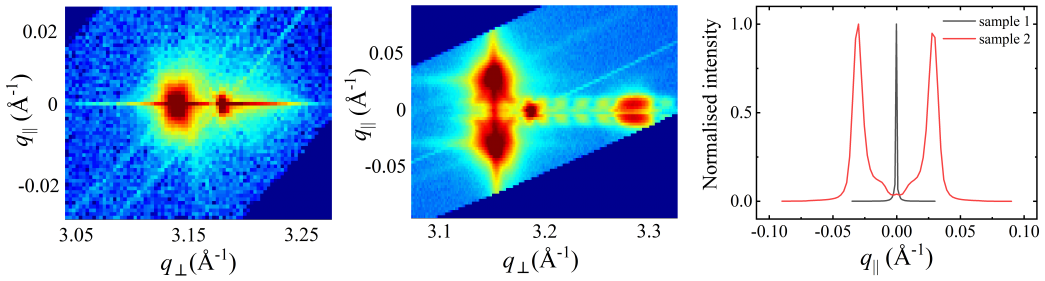

Figure 6.1: Left: RSM about $(002)_{pc}$ for sample 1. Middle: RSM about $(002)_{pc}$ for sample 2. Right: line profile along constant $q_{\perp}$ through the $BiFeO_3$ peak for each reciprocal space map.

oscillations which confirm the high quality of the LSMO film.

The line profile along $q_{\|}$ through the $BiFeO_3$ peak clearly shows the difference in peak splitting between these two samples.

6.3 Change in domain populations with cycling

It has been previously reported that upon cycling at sufficiently low frequencies the 71° stripe domain $BiFeO_3$ films is conserved, after an initial increase in stripe width [164]. This is consistent with the results in Chapter 5 obtained using using through electrode PFM. The measurements there give a good idea of the switching pathway, but in order to have a fuller picture it is necessary to study the dynamic behaviour in a time resolved manner. The technique used in this Chapter allows for these measurements as the splitting of $BiFeO_3$ peaks can be used to learn about the different populations of domain variants.

Fig. 6.2 shows a RSM of the $(024)_{pc}$ reflection from sample 2, where the $BiFeO_3$ peak is clearly split in two. For the two peaks of this type which are accessed by rotating the sample by ±90° this peak is not split. For a rotation of 180° it is. This is what is expected for two variant 71° stripe domains [164]. For films where all four monoclinically distorted structural variants are expected to appear in equal proportions, such as $BiFeO_3$ films on SRO/STO, the splitting should be clear for all four $(103)_{pc}$ reflections. It can be seen that after cycling the domain pattern changes, with the end result being a structure that is effectively monodomain. This is because defects accumulate at the as grown domain walls and act as pinning sites for the domain walls that are formed during the polarisation reversal process which are eventually displaced repeated cycling. The result of this is that after sufficient cycling the defect structure no longer drives the domains to maintain a

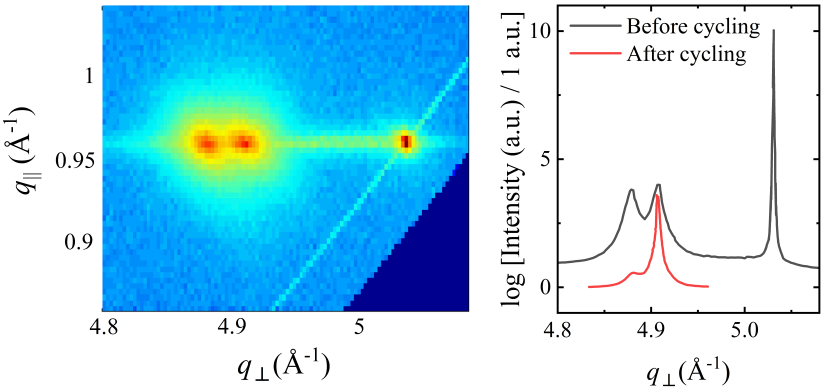

Figure 6.2: Left: RSM of $(024)_{pc}$ peak showing the $BiFeO_3$ peak split in two in $q_{\perp}$ due to the two different 71° domain variants in sample 1. Right: Line profiles at constant $q_{\parallel}$ through the split $BiFeO_3$ peak before and after cycling showing the distribution of intensity.

stripe domain structure. Instead, one of the polarisation variants that makes up the stripe domain pattern is favoured over the other. It appears that after the stripe pattern is smeared out by repeated cycling an effectively monodomain structure is formed.

The conclusion to draw from this measurement is that it is not directly possible to use this method to learn about the domain wall behaviour or domain pattern change during the switching process in $BiFeO_3$ devices with as grown 71° domain walls. This is because the switching ceases to be reversible in the way it is for the lower numbers of cycles used in previous studies such as that of Johann et al. [164]. It is however still perfectly valid to look for the structural response on the unit cell level and study the switching behaviour in that scheme.

6.4 Time resolved structural response to applied field

In this section the sequence of electrical and structural events during the polarisation reversal process in $BiFeO_3$ is presented. The structural response was measured using the 2d Pilatus detector and a rectangular PUND voltage sequence was applied. The limiting factor in these measurements proved to be fatigue, which caused breakdown after many electrical cycles. This is a greater problem for $BiFeO_3$ than $PbZr_{0.2}Ti_{0.8}O_3$ due to the higher leakage in $BiFeO_3$. By appropriately doping and using oxide electrodes for the top and bottom contacts the device lifetime can be significantly increased. This is the reasons why sample 3 is 5% Mn doped and has $La_{0.7}Sr_{0.3}MnO_3$ top electrodes. Specifically, Mn doping of $BiFeO_3$ results in leakage

current being significantly surpressed by the formation of deep trap levels [177].

Two samples are used in this part. First the structural response during polarisation reversal is measured for the $(002)_{pc}$ peak for a 150 nm thick 5% Mn-doped $BiFeO_3$ (sample 3) on SRO/STO. This is then compared with the structural response of an undoped $BiFeO_3$ film of similar thickness on SRO/DSO (sample 1).

6.4.1 5% Mn-doped $BiFeO_3$ on SRO/STO

Fig. 6.3 shows the electrical and structural response of sample 3 under cycling by a rectangular PUND voltage sequence. The current j rises and decays with a time constant of around 3 μs in response to the non-switching pulse (second), but for the switching pulse (first) there is an additional contribution from the ferroelectric switching that decays on a timescale of 20 μs. The pulse length of 40 μs was chosen to ensure all the switching occurs during the first voltage pulse.

The structural response during the switching peak seems to consist of at least three parts. These are labelled **I**, **II** and **III** on Fig. 6.3. In the first regime the out-of-plane lattice spacing of the pseudocubic unit cell c and bias induced strain ϵ slowly increase, but the normalised intensity $\widetilde{I}$ and normalised peak width in the out-of-plane direction $\widetilde{w}_\perp$ remain unchanged. Most of the charge flow occurs here. It is also in this part that the normalised peak width in the in-plane direction $\widetilde{w}_\parallel$ is at its highest, but begins to decrease. In the second part c and ϵ continue to increase but there is also a decrease in $\widetilde{I}$ and an increase in $\widetilde{w}_\perp$. In this part the ferroelectric switching completes. In the third part c and ϵ continue to increase but $\widetilde{I}$ and $\widetilde{w}_\perp$ maintain their new constant values. This step takes place after the ferroelectric switching is complete and therefore consists of the pure piezoelectric relaxation. After the field is removed c and ϵ relax and values for $\widetilde{I}$, $\widetilde{w}_\perp$ and $\widetilde{w}_\parallel$ tend towards new equilibrium values. After the voltage is removed some relaxation occurs as the piezoelectric response is not maintained.

One interpretation of this is as follows. In the first step the polarisation is not reversed but is rotated, mainly in-plane. As this happens the c lattice parameter will not significantly change, and there will be no compression of c due to the piezoelectric effect. During this step the structure factor and $\widetilde{I}$, which is sensitive to this, is effectively constant. As $\widetilde{w}_\perp$ is constant and does not deviate from its initial value in this regime it is possible to say that the rotation of the polarisation is essentially all in-plane. If there is a change in the out-of-plane component of polarisation it is small. Half way through this step $\widetilde{w}_\parallel$ has its maximum and begins to clearly decrease. This parameter is a measure of the in-plane coherence of the

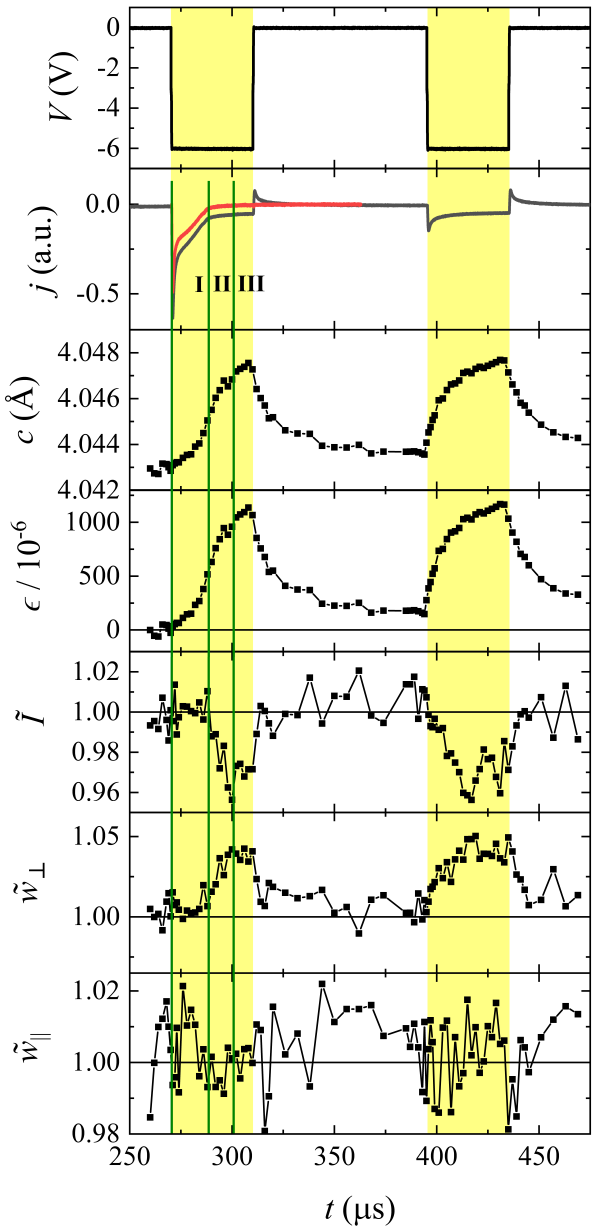

Figure 6.3: Electrical and structural response of sample 3 under cycling with a PUND pulse sequence. Only the negative pulses are shown. From top to bottom the panels show applied voltage, current (grey is raw, red is calculated switching current), out-of-plane lattice parameter c, the bias induced strain (calculated from the change in c), the normalised peak intensity and the normalised $BiFeO_3$ peak width in $q_\perp$ and $q_\parallel$.

lattice so it is reasonable to expect this parameter to reach its maximum value after the in-plane rotation has occurred, as it is expected that the rotation is not uniform throughout the sample. It is also reasonable to expect this parameter to decrease before the onset of the bulk of the ferroelectric switching occurs. In the second step the polarisation reversal occurs. This is evidenced by the increase in $\widetilde{w}_{\perp}$ and the change in $\widetilde{I}$. In this step c and ϵ increase most rapidly and $\widetilde{w}_{\parallel}$ is effectively constant. In the third step the sample response is purely piezoelectric.

Due to the rhombohedral structure of $BiFeO_3$ the polarisation is aligned along $(111)_{pc}$ directions. There are four 'down' states and four 'up' states. The sets of down and up states may be considered as effectively degenerate in energy. In reality this is not exactly true because the monoclinic distortion of the pseudocubic unit cell of the underlying orthorhombic $SrRuO_3$ layer has an effect, but as the distortion is rather small it does not significantly affect behaviour during individual switching cycles. Because of the effective degeneracy in energy it is reasonable to expect that upon application of an external electric field a unit cell with polarisation initially in a down state will be switched into the up state by simply being rotated through an angle of 71° in one step, because this is the pathway for which the structural deformation and energy cost is lowest. 109° and 180° switching in this geometry has a higher energy cost. This model is consistent with the findings of Baek et al. [178], but it is of note their work contains no dynamic measurements of the polarisation as it reorients. In this sample and this experiment although the switching pathway is expected to consist of one 71° step, it is important to note that in this sample polarisation can lie along any of the four polar axes and the specific pathway through which polarisation is switched will depend on the initial state. The as-grown domain structure consists of four-variant 71° stripe domains where the out-of-plane component of polarisation is all down. As the polarisation is switched from down to up states it passes through intermediate states where the proportion of polarisation that lies in-plane is higher than either the start or end states. Due to the complexity of the $BiFeO_3$ unit cell, consisting of two pseudocubic unit cells connected along the body diagonal with Bi and Fe atoms displaced and the two oxygen octahedra tilted in opposite directions it is extremely difficult to determine the time dependent motion of the full structure during the ferroelectric switching process. That said, it is possible to use the data collected to compare different models and get close to the true information. Three illustrative toy models for the polarisation switching process are shown in Fig. 6.4. In the first toy model the polarisation is considered fixed and traverses an arc as it switches between down and up states. This model is both inconsistent with the data and clearly

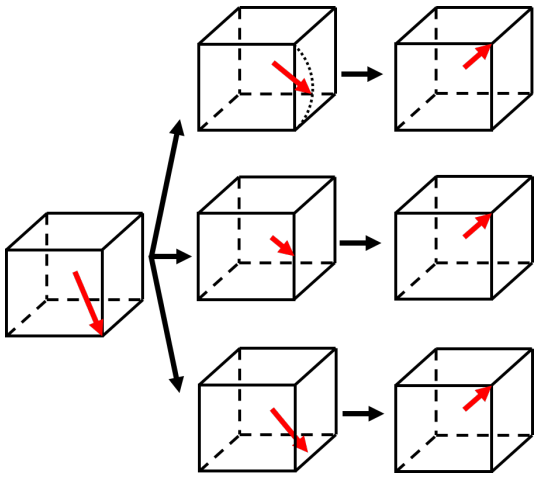

Figure 6.4: Simplified 71° switching pathways for rhombohedral $(001)_{pc}$ $BiFeO_3$. In the top route the magnitude of the polarisation is constant as it is rotated through an angle of 71° along an arc which connects the start and end states. In the middle route the magnitude of the polarisation is allowed to vary as it traverses the straight edge of the pseudocubic unit cell. In the lower route the polarisation is allowed to vary and moves in two stages. It first rotates through some angle in-plane before switching up to the final state.

wrong. There is not a justification for considering the polarisation as fixed during the switching process. The origin of the ferroelectricity is intimately connected with the loss of inversion symmetry and non-centrosymmetry of the unit cell and during the switching process the structure is varying with time. This situation is analogous to the magnitude of polarisation varying over the width of a domain wall, which is a known phenomenon [179, 180]. In the second toy model the polarisation is allowed to vary and traverses the shortest path separating the up and down states. This model is also inconsistent with the data but is more realistic as it allows the magnitude of polarisation to vary. The flawed assumption here is that the shortest path connecting the two energetically favourable for the polarisation to switch by traversing the shortest path. This is clearly an oversimplification given the complexity of the structural changes and associated time-dependent potential energy landscape. The third toy model allows the magnitude of the polarisation to vary. Here polarisation is rotated by some angle in-plane before the out-of-plane component is switched. During the rotation part the change in out-of-plane lattice parameter and structure factor is small. Unlike the previous models this model is consistent with the data presented in Fig. 6.3.

One feature that could possibly be expected to emerge in the data is an overall compression of c part way through the switching process. This would be

the result of the magnitude out-of-plane component of polarisation being smallest half way through the switching. This effect would be expected to be evident in the data for c, ϵ, $\widetilde{I}$ and $\widetilde{w}_{\|}$ but is not seen. This indicates that throughout the switching process the average value of the in-plane component of polarisation is roughly constant.

In addition to this model for the ferroelectric response other features are also present in the structural data. The first of these is the piezoelectric response, which is present at all times when voltage is applied. The piezoelectric response is dependent on the orientation and magnitude of the polarisation. For the case in which polarisation is aligned parallel to the applied field the lattice is driven to expand. For the case in which polarisation is aligned antiparallel to the applied field the lattice is driven to compress [181]. This behaviour is the one of the reasons why the increase in c and ϵ is slower in the first voltage pulse than the second. It is worth noting that piezoelectric coupling is typically linear, which is not what the data shows here. The data is however of a form consistent with similar measurements of $PbZr_{0.2}Ti_{0.8}O_3$ [174], where it was seen that the piezoelectric coefficient d_{33} is not constant on the microsecond timescale. This is consistent with work on similar materials which shows the piezoelectric response may indeed include both non-static and non-linear contributions [129, 182, 183].

In regions **I** and **II**, c and ϵ show a slow piezoelectric response which is similar to that seen in $PbZr_{0.2}Ti_{0.8}O_3$ [174]. This is typically associated with two processes: domain wall creep motion and reorientation of the oxygen octahedral structures. These processes are both slow as the structural and electrical responses occur on length scales that are much larger than the unit cell level. The charge flow that accompanies these slow processes is also slow, i.e. its timescale is not described by the time constant of the charging and discharging peaks, and is part of the reason why the tail of the of the current response is relatively long.

During the switching pulse the normalised peak intensity $\widetilde{I}$ can be seen to change by about 3%. The peak intensity is dependent on many variables, one of which is the square of the structure factor. A better measure of the structure factor is integrated peak area, as that is directly proportional to the structure factor [91]. For $PbZr_{0.2}Ti_{0.8}O_3$ the difference in structure factor due to the violation of Friedel's law for $(002)_{pc}$ to $(00\bar{2})_{pc}$ is around 7% [35, 174, 184]. Assuming the magnitude of the effect in $BiFeO_3$ is similar the observed change in $\widetilde{I}$ which is coincident with the switching may be associated with it.

It is worth noting that Friedel's law is not a fundamental law of physics. It is simply a statement that the Fourier transform of a real function $F(k) =$

$\int_{-\infty}^{\infty} f(x)e^{ikx}dx$ has the following property: $F(k) = F^*(-k)$. Here F^* is the complex conjugate of F. The squared amplitude of this is centrosymmetric $|F(k)|^2 = |F(-k)|^2$. The structure factor for centrosymmetric systems exactly matches this mathematical relation. Non-centrosymmetric structures (i.e. those without inversion symmetry) however do not as k and $-k$ are not conjugate pairs. For the case that k and $-k$ are not conjugate pairs Friedel's law is said to be 'violated'.

To exclude the possibility of Ohmic heating causing the expansion in c parameter, the temperature increase required to cause the expansion was calculated using the following equation:

$$\frac{\Delta c}{c} = \alpha_{THE}\Delta T. \tag{6.1}$$

In this equation the fractional change in c is expressed in terms of the linear coefficient of thermal expansion α_{THE} and the temperature change ΔT. Assuming α_{THE} is approximately 10^{-5} K^{-1} (typical for perovskite oxides), to achieve the fractional change in c shown in Fig. 6.3 (approximately 0.14%) a temperature change of increase of 140 K is required. It is therefore not plausible that this increase in c originates from Ohmic heating of the $BiFeO_3$ during the switching process, where the transient switching currents are on the order of tens of μA and the DC resistance is typically tens of MΩ.

In summary, the data here suggest that the switching consists of two steps. First a metastable state where polarisation is rotated in-plane by some angle is stabilised. This process takes around 15 μs, which is a surprisingly long time, however it is reasonable as the accompanying structural deformation is complex and is coupled to the larger lattice structures, including the oxygen octahedra. Only once this state is established does the switching really take place. The piezoelectric response of this sample is similar to that of $PbZr_{0.2}Ti_{0.8}O_3$, which indicates that domain wall creep motion and reorientation of oxygen octahedral structures are coupled with the polarisation reversal here.

6.4.2 Undoped $BiFeO_3$ on SRO/DSO

The time dependent structural response of sample 1 is shown in Fig. 6.5. This sample is undoped and deposited on SRO/DSO. Two series of data are shown. The first series is for the $(024)_{pc}$ peak and the second series is for the $(103)_{pc}$ peak. Both show a similar response, which is strikingly different from that of sample 3.

The current response for both series of data shows a clear switching peak

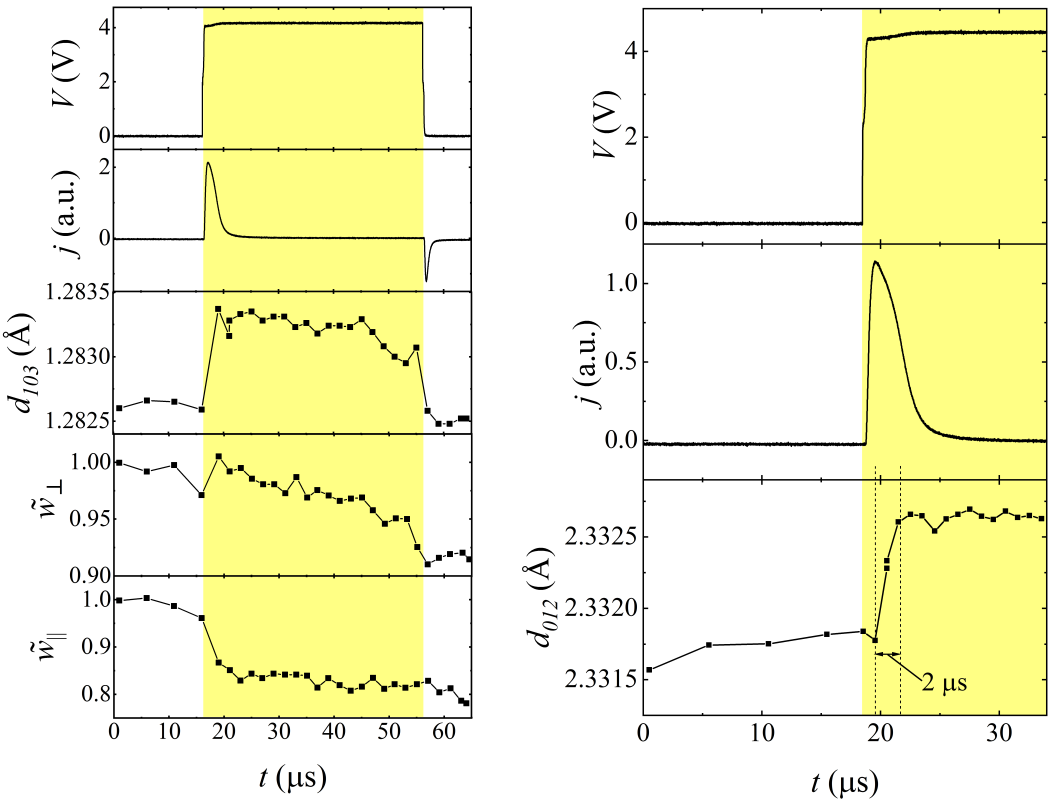

Figure 6.5: Electrical and structural (left is $(024)_{pc}$ and right is $(103)_{pc}$) response of sample 1 under cycling with PUND. Only the positive switching pulse is shown. From top to bottom the panels show applied voltage, current (grey is raw, red is calculated switching current), d-spacing d_{hkl} and normalised $BiFeO_3$ peak width in $q_\perp$ and $q_\parallel$.

which is narrow compared to that of sample 3. The applied voltages are similar and are sufficient to ensure complete switching.

The first difference is in the response of the interplanar spacings d_{012} and d_{103} to applied voltage. The increase in this sample is much faster, and an initial decrease in d_{012} as soon as field is applied can be seen. Despite both these peaks having an in-plane component the out-of-plane Miller index is greater meaning that the response of the out-of-plane component will dominate over the in-plane component. i.e. the observed increase in these d-spacing can be interpreted as an effective increase in out-of-plane lattice parameter. In the data for the $(024)_{pc}$ Bragg reflection there is a weak feature at the beginning of the voltage pulse that could imply a compression. From this data it is possible to say that if this signal is genuine then that compression is less than in the case of $PbZr_{0.2}Ti_{0.8}O_3$. This is reasonable due to the different orientations of the polar axes in $BiFeO_3$ and $PbZr_{0.2}Ti_{0.8}O_3$, and is consistent with the data presented for sample 3.

The second difference is that the rapid increase in d-spacing occurs on the same timescale as most of the charge transport, and can therefore be associated with the ferroelectric switching. There is no slow piezoelectric response here. In ferroelectric materials the competition between disorder and elasticity determines the domain wall motion behaviour under DC field. This is inherently related to the switching dynamics. There are three regimes: creep, depinning, and flow. At zero temperature domain walls are pinned by disorder and do not move when small electric fields are applied. Above a critical field a depinning transition occurs. Above this, the domain walls have a velocity which is proportional to the field - this is the flow regime. At finite temperature thermal effects smear out the depinning transition and a finite velocity is expected for non-zero field. This motion is thermally activated and is known as creep [185, 186]. Fig. 6.6 shows this schematically. The explanation for the absence of a slow piezoelectric response in sample 1 is that the switching process here appears to be essentially creep free. It is reasonable to expect that sample 1 has less disorder than sample 3 for two reasons. Firstly, the $DyScO_3$ substrate is a better lattice match so the $BiFeO_3$ film is essentially strain-free. secondly, the biaxial strain from the $DyScO_3$ substrate has the effect of favouring domain growth along one in-plane direction than the other, which means the process of domain nucleation and growth in this sample is less disordered than the sample on $SrTiO_3$ which has no such anisotropy. The effect of it being more ordered is reduce the amount of pinning and make the flow regime a better description of the domain wall motion during the switching process. The reorientation of oxygen octahedra in the two films is expected to be similar

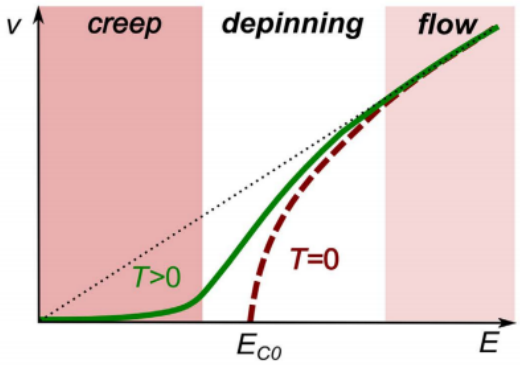

Figure 6.6: Theoretically-predicted domain wall velocity (v) for a pinning dominated system under DC electric field. The three dynamic regimes (creep, depinning, flow) are indicated by different colours. E_{C0} represents a dynamic threshold field at zero temperature. Figure from Ref. [185].

because of their similar symmetry, hence it is likely that is not the cause of the slow piezoelectric response in the data previously presented for sample 3. The same can be said for the $PbZr_{0.2}Ti_{0.8}O_3$ sample similar data are presented for by Kwamen et al. [174].

Despite the peaks measured here containing a mixture of information from in-plane and out-of-plane contributions, it is valid to interpret $\widetilde{w}_\perp$ and $\widetilde{w}_\parallel$ as quantities dominated by the out-of-plane and in-plane coherence respectively, despite the mixing. This is because for the peaks measured the Miller index for the out-of-plane component is larger than the non-zero in-plane component. Due to the mixing of in-plane and out-of-plane components it is correct to expect that along these directions the switching is less inhomogeneous than the case of the $(002)_{pc}$ direction. Despite this, in contrast to sample 3, $\widetilde{w}_\perp$ does not significantly increase when the voltage is applied. This indicates that the switching in sample 1 is less inhomogeneous over the device area. In fact, there is a significant decrease in $\widetilde{w}_\parallel$ at the start of the switching peak which may be associated with an increase in coherence caused by domain coalescence.

Using the same method as for the Mn doped sample, the temperature increase required in order for the fractional change in d-spacings shown in Fig. 6.5 to be caused by Ohmic heating are around 80 K and 40 K. For the same reason as for the Mn doped sample, it is clear that the expansion in d-spacing does not originate from Ohmic heating.

The conclusions to draw from these measurements are that:

1. the polarisation switching pathway in the BFMO/SRO/STO film consists

of one 71° step which takes place in two parts. The polarisation rotates in-plane before the bulk of the ferroelectric switching occurs. During the process of ferroelectric switching the in-plane component of polarisation is approximately constant, and

2. the piezoelectric response of the BFMO/SRO/STO film is dominated by creep and motion of the octahedral tilting structure. This is unlike the essentially strain free BFO/SRO/DSO sample for which these slow processes are absent.

6.5 Chapter summary

In this work a number of aspects of the polarisation switching dynamics in $(001)_{pc}$ oriented $BiFeO_3$ have been revealed. Firstly, it has been demonstrated that the time-resolved experiments used here are not appropriate to probe the domain dynamics of $BiFeO_3$ with, as after significant cycling the as-grown domain structure is effectively erased and a more monodomain structure is stabilised. It is possible to extract the dynamics at the unit cell level though. The ferroelectric switching has been found to consist of an initial in-plane rotation, after which the value of polarisation is temporarily suppressed, followed by the polarisation flipping upwards to complete its reorientation to an end state which is offset from its start state by 71°. Further to this, the strain imposed by the substrate is found to have a significant effect on the timescale of the switching dynamics. When the $BiFeO_3$ layer is deposited on $SrRuO_3$ buffered $DyScO_3$ it is essentially strain free and ferroelectric switching proceeds quickly, unhindered by the relatively slow processes of the creep motion or the oxygen octahedral dynamics. These processes are present when an $SrRuO_3$ buffered $SrTiO_3$ substrate, which exerts a compressive strain, is used.

Chapter 7

Electric field induced strain wave assisted ferroelectric switching in $BiFeO_3$ and $BaTiO_3$

7.1 Introduction

The process of ferroelectric switching is mediated by the nucleation and growth of domains [23]. The timescale of this process is limited by the domain wall velocity [187]. Improving the timescale of ferroelectric switching is an attractive goal to researchers who aim to design devices for applications where fast data processing is required. As early as 1994 simulations predicted that manipulation of the ferroelectric "soft phonon" mode with ultrashort optical pulses offered a way to achieve reversal times as low as 10 ps [188]. Relatively recently it has been experimentally shown that it is possible to achieve polarisation reversal times of less than 80 fs in $LiNbO_3$ by using femtosecond long mid-infrared pulses to excite a high-frequency phonon mode [189]. The effect of this is that the atoms are displaced within the unit cell along the ferroelectric mode and the polarisation is transiently reversed. This timescale is three orders of magnitude quicker than what is possible to drive with electrical pulses, however it is notable that in their case despite the polarisation being reversible it relaxed back to its initial state around 200 fs after excitation. In the work presented here an alternative route for accelerating polarisation switching in ferroelectrics is presented. Here a metal-ferroelectric-metal capacitor device structure is used, and an 1028 nm infrared laser pulse is used to generate an ultrafast acoustic strain wave (compressive) [190] in one metallic electrode ($SrRuO_3$ and $La_{0.7}Sr_{0.3}MnO_3$ here)

which propagates through the ferroelectric layer during the switching process. The effect of this is expected to be seen in both the structural response and the electrical response when the same time resolved measurement methods as in Chapter 6 are used. The aim of the experiments presented here are to investigate if the switching dynamics of ferroelectrics can be accelerated or enhanced by this mechanism.

The incident laser pulse can be expected to have three effects on the sample. These are a) heating of the sample, b) generation of an ultrafast sound wave using the metallic bottom electrode as a transducer or c) generation of free charge carriers. The latter possibility is in the current experiment practically ruled out as wavelength of the laser used, 1028 nm (1.2 eV), is well below the band gap of both $BiFeO_3$ (2.7 eV) and $BaTiO_3$ (3.2 eV).

7.2 Experimental and sample details

The two samples are used here are summarised in table 7.2. Top electrodes on samples 1 and 4 are squares of side length 200 μm, realising metal-ferroelectric-metal capacitor devices. The hysteresis loop for sample 4 is shown in Fig. 7.1. The frequency used for this measurement is 2 kHz which is close to the cycling frequency used in the experiments here.

Here the raw structural data was measured with the 1d point detector. In order to improve statistics the time dependent raw data was convoluted with a step function of 800 ns width before being fitted as described in Chapter 3. This width of the step function was chosen as it reduced noise significantly without fine features being smeared out.

The majority of the data presented in this chapter are for $BiFeO_3$ (sample 1). A small amount of data for $BaTiO_3$ is included at the end for comparison.

ID	Top electrode	Ferroelectric	Bottom electrode	Substrate	Notes
1	Pt	$BiFeO_3$	$SrRuO_3$	$DyScO_3$	71° stripe
	30 nm	150 nm	8 nm		
4	Pt	$BaTiO_3$	$La_{0.7}Sr_{0.3}MnO_3$	$SrTiO_3$	Monodomain
	30 nm	250 nm	25 nm		

Table 7.1: Samples used for time resolved laser-assisted switching measurements.

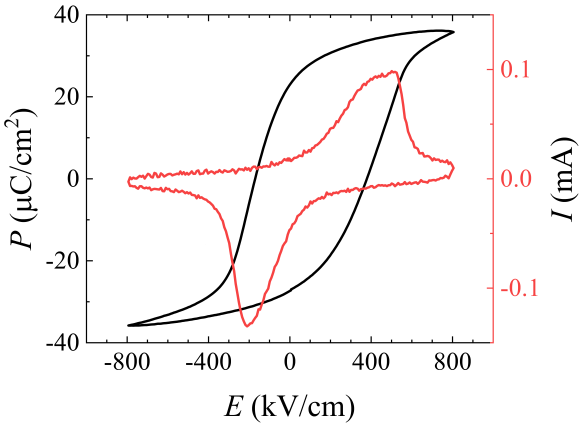

Figure 7.1: Ferroelectric hysteresis loop for sample 4 measured using a triangular waveform at a frequency of 2 kHz.

7.3 $BiFeO_3$

7.3.1 Effect of laser fluence

In order to search for the effect the laser pulse has on the switching a PUND sequence at a sub-coercive field of 3.5 V was applied and laser pulses of 15 ps duration and various fluence were applied. The fluences applied should be sufficient to generate the strain wave response in the $SrRuO_3$ layer [190]. The timings was such that the laser pulse was applied around 1 μs after the onset of ferroelectric switching, which is part way through the switching process. The result of this experiment is shown in Fig. 7.2. The black vertical line indicates the arrival time of the laser pulse. All fluences quoted in this chapter take into account the projection of the laser spot on the sample. The step part way up the voltage pulse is caused by a back reflection caused by an impedance mismatch between two cables in the measurement setup. As there is no trace of this in the current response the sample does not experience this and it can be considered simply as a measurement artefact.

In this data the fluence does not seem to have a significant effect on the electrical response, however there are trends in the structural data. It is of note that after the initial voltage pulse the induced strain returns to being close to zero, irrespective of the initial fluence. The normalised integrated peak area $\widetilde{A}$ shows no clear features over this range. The incidence time was found to have no effect on structural response which suggests that the features is from heating alone. This means that in this case the there is no improvement in ferroelectric polarisation reversal caused by an induced strain wave. The thermal expansion coefficient of these materials is typically on the order 10^{-5} K^{-1} so the values for induced strain

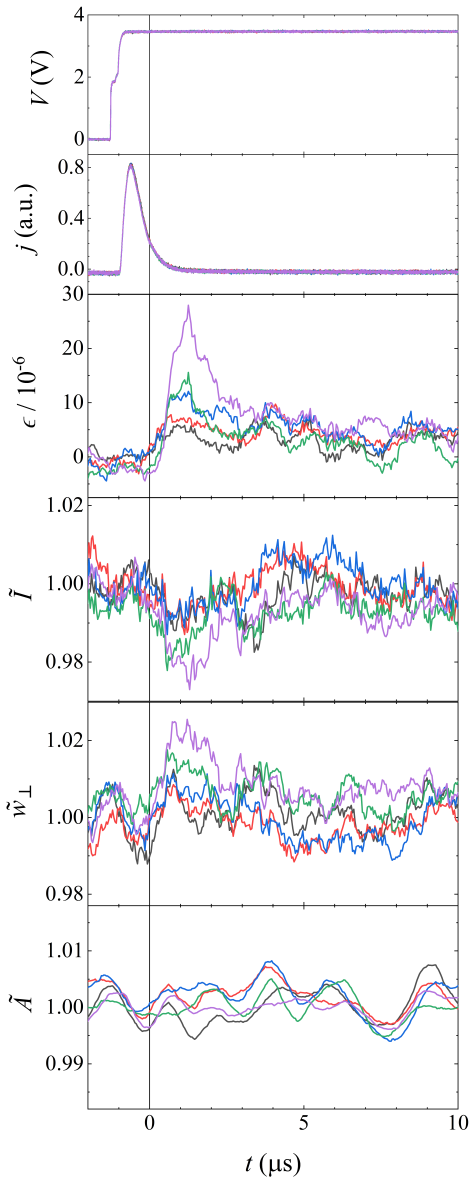

Figure 7.2: Simultaneous electrical and structural response of a capacitor device subjected to both subcoercive voltage pulses and 15 ps laser pulses of different fluence (applied at t=0 always). Incident fluences on te sample shown are 12.4 mJ/cm^2 (black), 15 mJ/cm^2 (red), 20 mJ/cm^2 (blue), 25 mJ/cm^2 (green) and 35 mJ/cm^2 (purple). Structural data is normalised relative to the response for a data series where a laser fluence of 10 mJ/cm^2 is used. In all these scans duration of the laser pulse is 15 ps. From top to bottom, the panels show as a function of time the applied voltage, current response, the induced strain, normalised peak width and normalised peak intensity. For this series of data the applied voltage was 3.5 V, which is below the coercive field

here indicate that the laser heating is a few K. This is in line with what can be calculated by considering the fluence, pulse duration, and absorption of the laser pulse by the device under test. For higher fluence, the heating effect is greater. It appears faster as the temperature change is larger, but in reality is not. The increase in normalised peak width it is coincident with the clear feature in induced strain. The physical interpretation of this parameter is that it is a measure of the decoherence in the out-of-plane direction, and it stands to reason that this increases by a small amount by heating. More accurately, because the incident beam has a finite width and a small divergence this parameter does contain some in-plane information, however it is dominated by the out-of-plane contribution.

7.3.2 Effect of delay

The next experiment probed the effect of the arrival time of the laser pulse on the polarisation switching. Laser pulses of 12.4 mJ/cm^2 fluence and 15 ps duration were applied at various incidence time while a PUND sequence of 4 V amplitude (just above the coercive voltage for this sample) was also applied. The result is shown in Fig. 7.3. For lower voltages than 4 V the structural response was purely piezoelectric and no switching was observed. From the data it is clear that when the laser pulse arrives late into the ferroelectric switching process it has a larger effect.

As mentioned before, the peak area is proportional to the square of the structure factor. The structure factor is different for 'up' and 'down' states due to violation of Friedel's law [174, 184]. The parameter $\widetilde{I}$ is also sensitive to this change but contains other effects. There are two features here, the overall increase in $\widetilde{A}$ resulting from the laser pulse and its speed. The greatest change in $\widetilde{A}$ is realised for the data series where the laser arrives rather late on and the smallest change is realised when the laser pulse arrives close to the onset of the pulse. This demonstrates that the effect of the laser pulse is to increase the amount of polarisation that can be switched for a given applied field. This is consistent with what would be expected for laser assisted switching by strain wave that modulates the crystal structure of the ferroelectric layer. In addition, the speed at which normalised peak area increases greatest for the series when the laser arrives late on into the switching process. It seems that the extent to which the laser pulse affects the ferroelectric switching process is related to the state of structural and electrical disorder it finds the device in. For cases when the $BiFeO_3$ is already in a slightly inhomogeneous state the laser has a larger potential to assist and enhance the switching

In contrast to the peak area, the other three structural parameters plotted

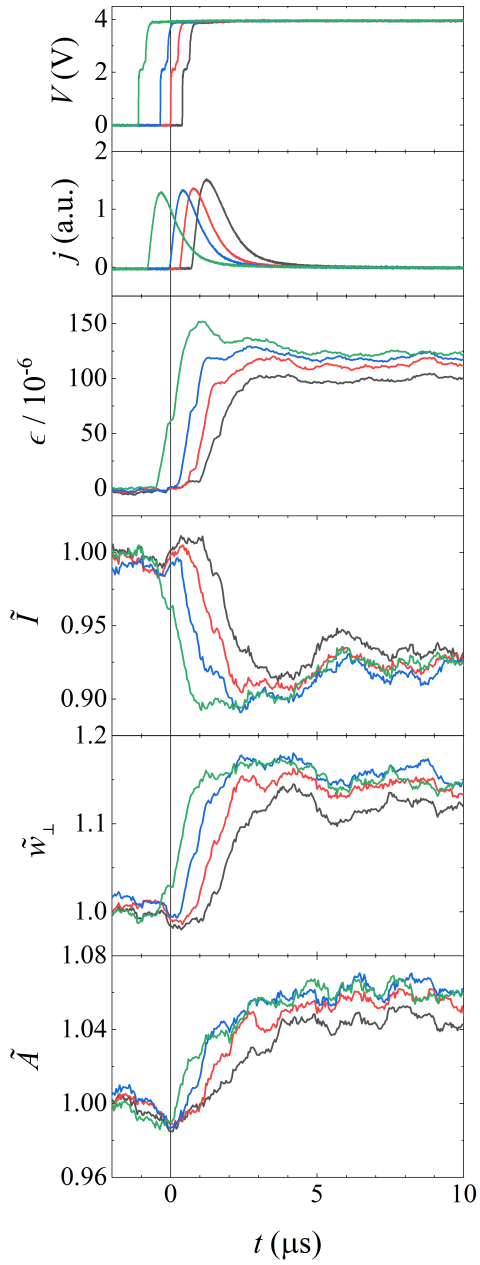

Figure 7.3: Simultaneous electrical and structural response of a capacitor device subjected to both i) subcoercive voltage pulses of different delays (by colour) and amplitude (from left to right) and ii) 15 ps laser pulses of fluence 12.4 mJ/cm^2. The voltage applied is 4 V. From top to bottom the panels show as a function of time the applied voltage, current response, induced strain, normalised peak intensity, normalised peak width, and normalised peak area. Structural data are normalised relative to the sample response at the same voltage but with no laser pulse applied.

are dominated by the other effects, notably the piezoelectric response. Despite this there are some differences in the responses for different voltage delays. After the switching is complete the value of ϵ which the system settles at is dependent on delay between voltage and laser pulse. This effect is from the ferroelectric switching and is consistent with the trend seen in $\widetilde{A}$. Further to this, the rate at which the strain increases shows the same delay dependence as $\widetilde{A}$, however here the increase is more rapid and additional effects are present. The first of these is the heating, but as the calculated temperature increase from the laser pulse is not large the effect of this on the rate of piezoelectric response is expected to be very small. The second effect is associated with the effect of the strain wave on the non-linear piezoelectric during switching. During switching due to structural change d_{33} is not constant, meaning that the timing of the strain wave resulting from the laser pulse hitting the SRO can be expected to have an effect on the speed of the piezoelectric response. Finally, in the strain data a peak after the initial rise emerges as the voltage pulse is brought progressively earlier in the time domain. Evidently for the case when the strain wave is most strong the c lattice parameter is initially driven to expand beyond the value it settles at. The data for $\widetilde{w}_{\perp}$ broadly mirrors the data for ϵ. This is indicative of a simple heating effect. At higher temperatures, due to disorder and anharmonicity, peaks are broadened. This should go directly along with the thermal expansion.

7.3.3 Effect of pulse duration

To attempt to distinguish heating and strain wave effects a series of measurements with two different laser pulse durations were applied.

Here a PUND sequence of 4.5 V amplitude was applied. This is above the coercive voltage and realises a relatively large amount of ferroelectric switching. The fluence is again fixed at 12.4 mJ/cm^2. Two series were measured, one with a pulse duration of the laser pulse of 15 ps and the other with a pulse duration (more specifically, a full width at half maximum in the time domain) of 300 fs. For both cases we expect the strain wave to be generated, but the heating effect will be approximately 50 times smaller for the measurement series with the shorter pulse.

Fig. 7.4 shows values of normalised peak area 12 μs after the laser pulse is fired. This time was chosen as it is several microseconds after which the structural response stabilises. From this data it is clear that the greatest change in integrated peak area (and therefore structure factor) occurs in the data series with the longer pulse duration, hence the larger heating dose. The difference between these two datasets is not anywhere near a factor of 50 though. This suggests that although the effect of heating on the structural change is important, the effect of the laser-induced

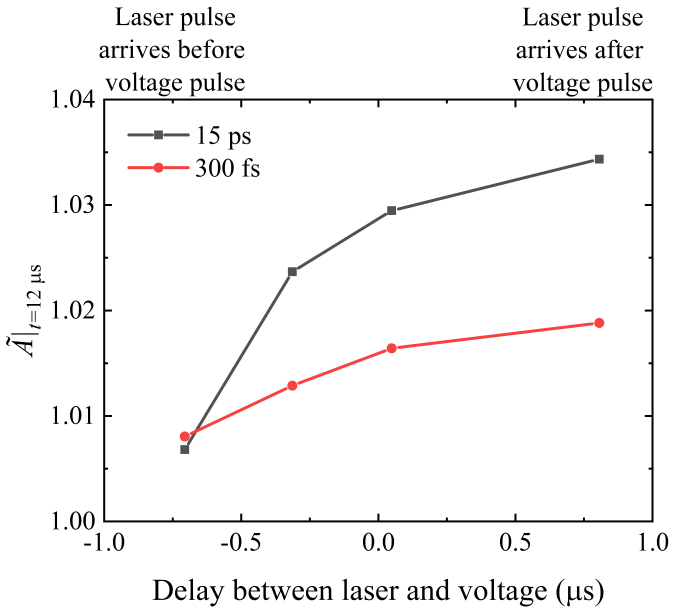

Figure 7.4: Dependence of normalised integrated peak area on the delay of the laser pulse with respect to the voltage pulse. Here voltage pulses of 4.5 V and laser pulses of 12.4 mJ/cm^2 and either 15 ps or 300 fs duration are applied. Normalisation is relative to data collected in the same conditions but without laser.

strain wave on enhancing the ferroelectric switching also has a significant effect.

7.3.4 Remarks

From the data in this section we can draw the following conclusions:

1. it is possible to enhance and accelerate ferroelectric switching by using a pulsed 1028 nm laser to launch a strain wave from a metallic bottom electrode which acts as a transducer,

2. the laser-induced strain wave does not itself induce switching, but it can accelerate and enhance switching,

3. both the effects of heating and laser induced strain wave effects are evident in the structural response. There is no effect on the electrical response for the $BiFeO_3$ devices tested here, and

4. the effect of the laser pulse is greatest when it is incident on the device at a time at which there is structural disorder.

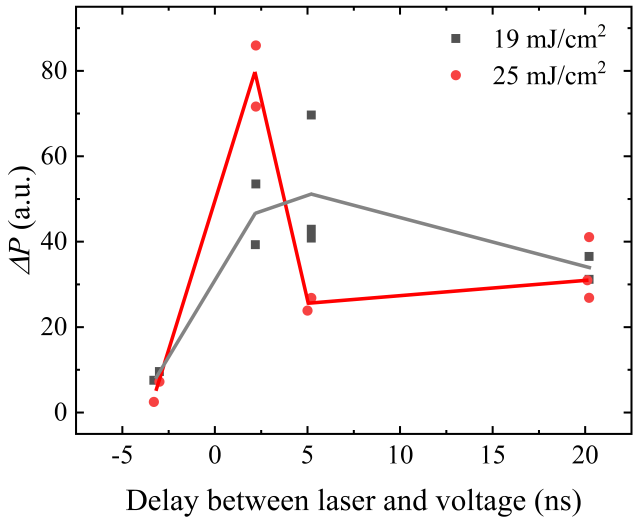

Figure 7.5: The effect of laser timing on polarisation reversal in sample 4 for fluences of 19 mJ/cm^2 and 25 mJ/cm^2.

7.4 $BaTiO_3$

7.4.1 Effect of delay

Following the measurements on the $BiFeO_3$ samples presented in this chapter, similar measurements on a $BaTiO_3$ sample were carried out. Preliminary results from sample 4 in table 7.2 are shown here. Interestingly, unlike for the $BiFeO_3$ samples there is a clear current response associated with the laser pulse. The voltages applied here are below the coercive voltage. By extracting the difference between the current traces it is possible to extract the charge transport associated with the ultrafast strain wave, and from this the difference in switched polarisation can be calculated. Results from this experiment are shown in Fig. 7.5. Here the fluences used were 19 mJ/cm^2 and 25 mJ/cm^2. The pulse length was 300 fs (more specifically, the full width at half maximum in the time domain). Unlike $BiFeO_3$ the laser pulse can be seen to have a clear effect on the current. Unlike $BiFeO_3$, when subcoercive field is applied the laser pulses do have an effect on the amount of polarisation which is switched. For higher fluences the polarisation is flipped both faster as well as further than the subcoercive field alone drives it. The scatter between the set of data measured here are different. It is possible that during the measurements at lower fluence that the laser spot shifted such that it was not completely incident on the device under test. Despite this, the overall trend that higher fluence causes greater and quicker polarisation reversal is clear.

7.5 Chapter summary

In this work it has been demonstrated that it is possible to accelerate and enhance ferroelectric switching in both $BiFeO_3$ and $BaTiO_3$ by launching a compressive acoustic strain wave through the ferroelectric layer during polarisation reversal. The fluence, arrival time of the laser pulse with respect to the applied field and pulse duration are all important factors. In addition to the strain wave effect there is also a notable heating effect. The same time resolved structural characterisation methods used in Chapter 6 are proven to be appropriate probes of the structural response, however $BaTiO_3$ exhibits a clear electrical response. By integrating the extra displacement current in the current response it is clearly shown that it is possible to affect the charge transfer and hence the polarisation switching.

Chapter 8

Structural investigation and photovoltaic response of mixed-phase M_B-orthorhombic $BiFeO_3/NdScO_3$

8.1 Introduction

The behaviour of $BiFeO_3$ under tensile epitaxial strain is not well understood. First principles and thermodynamics calculations have predicted that an orthorhombic phase of $BiFeO_3$ can be stabilised at high tensile strain, however estimates of the value of strain required for that range from 2.3% to 7% [191–194]. At this strain induced phase boundary between the rhombohedral-like M_B phase and the orthorhombic phase the dielectric constant and piezoelectric coefficients are predicted to be significantly enhanced and M_B and orthorhombic phases are predicted to coexist. Experimentally a number of structural phases of $BiFeO_3$ under tensile strain have been reported. These include M_B [195, 196], orthorhombic [197, 198], mixed orthorhombic-rhombohedral [199, 200] and even tetragonal structures [201]. When considered together these do not provide a coherent picture. In fact, some of these reports are conflicting. For example, Yang et al. [197] claim to stabilise a purely orthorhombic phase on $NdScO_3(110)_o$ but using similar deposition conditions and the same method both Chen et al. and Sando et al. [195] both obtained films with a single phase M_B structure on $PrScO_3(110)_o$, which is expected to favour formation of the orthorhombic phase more than $NdScO_3(110)_o$ as it exerts a greater tensile strain of around 1.5%. It

seems strain alone does not provide the full story and that processing conditions such as the growth rate may have a significant effect on which structural phases are stabilised. This has been found to be the case for the BFO/LAO ($BiFeO_3$/$LaAlO_3$) system, where the compressive epitaxial strain imposed by the substrate stabilises a tetragonally distorted phase and mixed-phase regions containing exhibiting both rhombohedral-like and tetragonal-like phases may coexist [77]. To add to the complexity of the structural picture, it has been demonstrated that even in effectively unstrained $BiFeO_3$ films (on TbScO3$(110)_o$) the bound charge at charged domains can act to both induce the formation of tetragonal-like structures and also stabilise nanosized domains with polarisation states with a large in-plane component and unconventional domain walls [102].

In this chapter a mixed-phase $BiFeO_3$ sample with $(001)_{pc}$ orientation and highly ordered stripe domains is studied. This is the first report of a sample of this type under tensile epitaxial strain. Two phases are present, a rhombohedral-like M_B phase and a more orthorombic-like M_B phase. Detailed structural measurements with XRD and TEM are presented. Finally, an interesting photoelectric response which can be associated with the polarisation instability and a possible phase transition in this mixed-phase strained system is presented.

8.2 Sample details

Fig. 8.1 shows simple XRD and PFM characterisation for the BFO/NSO film studied here. The $BiFeO_3$ layer was deposited directly on the untreated as-received $NdScO_3$ substrate at a rate of around 0.38 Å/s. The other deposition conditions were the same as those used for optimised growth of step flow 71° stripe domain $BiFeO_3$ on SRO/DSO. Like the BFO/SRO/DSO film in Chapter 5 after deposition the BFO/NSO sample here was cooled at a rate of 20 °C/min in 5 mbar O_2. In the XRD data the $BiFeO_3$ peaks appear unsplit which suggests the film is single phase. No parasite phases such as Bi_2O_3 or Fe_2O_3 can be seen. From the Laue thickness fringes in the zoom of the $(001)_{pc}$ peak it is possible to estimate the thickness of this film to be 23 nm. The presence of these fringes tells us that both the film surface and the film/substrate interface are of high quality. From the position of the $BiFeO_3$ peak it is possible to calculate that the out-of-plane lattice parameter is around 3.89±0.01 Å. This is consistent with the results of Yang et al. [197] and Chen et al. [195] who determine values of 3.90 Å and 3.884 Å for samples of similar thickness with orthorhombic and M_B $BiFeO_3$ structures respectively. For reference, the bulk value for the unstrained pseudocubic unit cell is 3.965 Å. The decrease in out-of-plane

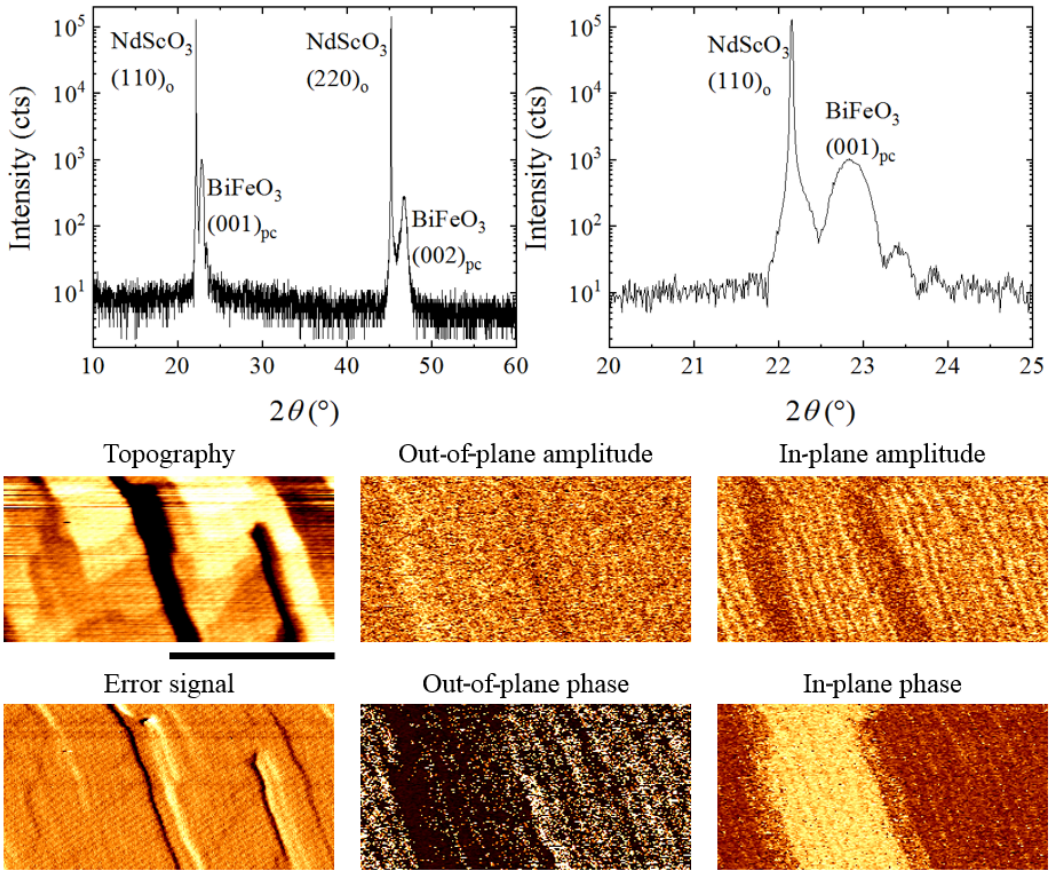

Figure 8.1: Simple XRD and PFM characterisation of 23 nm BFO/NSO film. The black scale bar is 500 nm. PFM scans were collected at an AC voltage of 3 V and frequency of 22.36 kHz.

lattice parameter is due to the tensile epitaxial strain imposed by the substrate. It is valid to compare the film here against those in the above named studies as the films there were prepared by the same method under similar strain and deposition conditions.

The PFM characterisation of the 23 nm BFO/NSO sample is also shown in Fig. 8.1. The topography shows atomically flat plateaus between the finger-like islands. This type of surface morphology is often seen in $BiFeO_3$ films deposited directly on insulating $REScO_3$ substrates with no conductive bottom electrode layer. There are faint features in the topography running from top to bottom which are correlated with the domains show in the PFM. These are wedge disclinations, the presence of which indicates that the polarisation has a non-zero out-of-plane component. From this information alone it can be concluded that the bulk of the film here does not have an orthorhombic or M_C type structure. In both of those cases the polarisation is confined to lie purely in-plane. The PFM signal shows clear stripe domains which are aligned with the overall features in topography. These domains are around 30 nm in width and appear in bundles, which is consistent with the results of both Yang et al. [197] and Chen et al. [195]. In order to further study the sample structure here more detailed measurements using XRD and TEM were performed.

8.3 In-depth x-ray characterisation

8.3.1 Symmetric RSMs

Fig. 8.2 shows reciprocal space maps for the $(00L)_{pc}$ reflections for both the 23 nm BFO/NSO film shown in Fig. 8.1 and a 100 nm BFO/DSO film. The BFO/DSO sample is essentially unstrained so can be considered as rhombohedral and exhibits clear periodic 109° stripe domains, albeit with some period doubling. The $BiFeO_3$ peaks on the line $q_{\|} = 0$ appear unsplit in $q_{\perp}$ for both films. This demonstrates that the film consists of, or is at least significantly dominated by, a single structural phase. From the $BiFeO_3$ peak positions in $q_{\perp}$ the effective out-of-plane pseudocubic lattice parameter can be calculated. For the BFO/NSO and BFO/DSO samples here the values of this parameter are are 3.885$\pm$0.002 Å and 3.9879$\pm$0.0001 Å respectively. As a reminder, the pseudocubic lattice parameter of bulk $BiFeO_3$ is 3.965 Å and the in-plane lattice mismatch of $BiFeO_3$ with $NdScO_3$ and $DyScO_3$ substrates is around +0.9% and -0.3% respectively.

From splitting of the $BiFeO_3$ peaks in $q_{\|}$ it is possible to learn more about

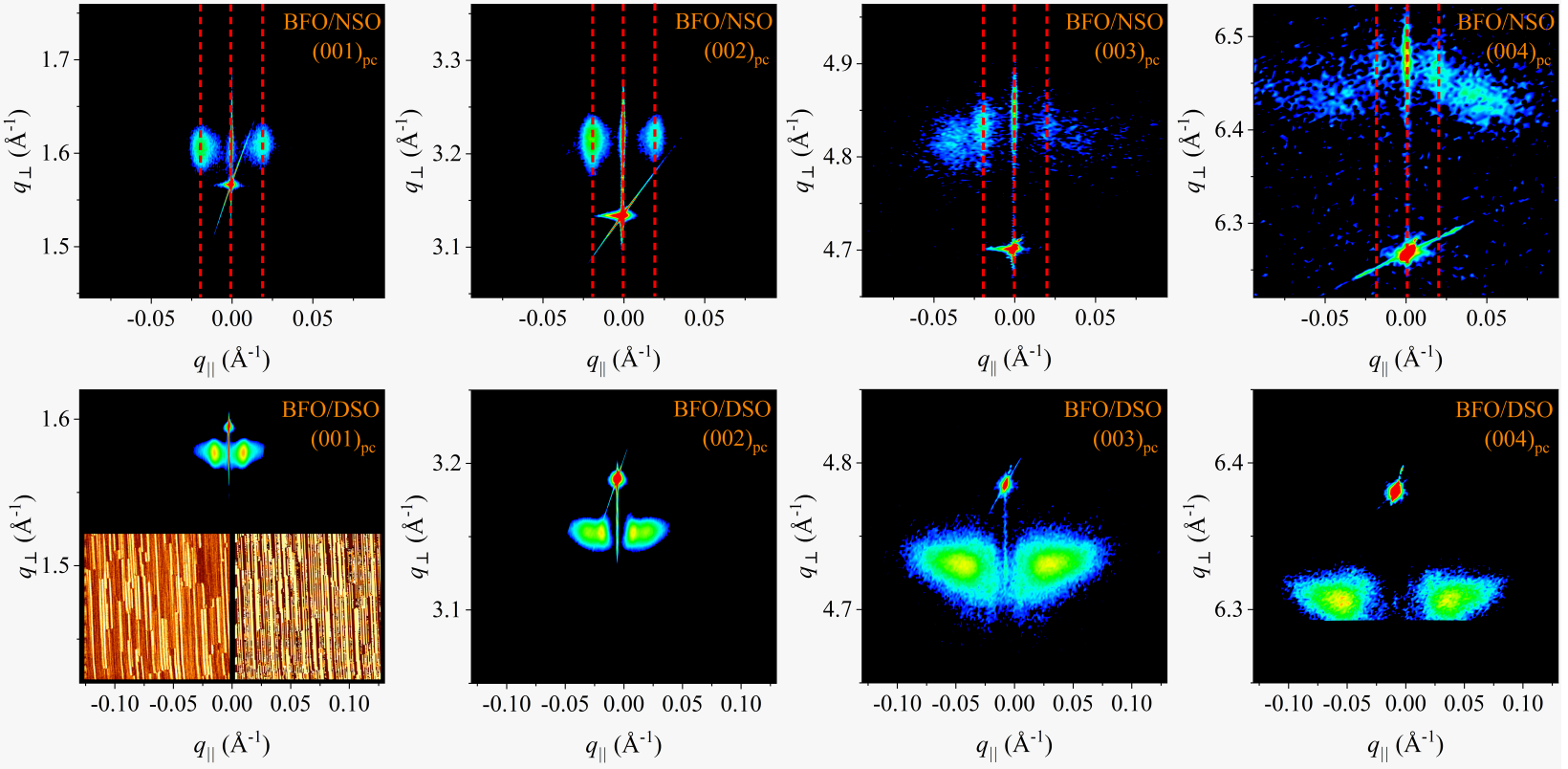

Figure 8.2: $(00L)_{pc}$ RSMs for 23 nm BFO/NSO (top) film and a reference 100 nm BFO/DSO (bottom) film. For both samples domain walls were aligned so they were perpendicular to the incident beam. It is only when this condition is met that the satellite peaks are visible. PFM in-plane amplitude (left) and phase (right) images of a 2×2 μm^2 area showing the domain structure of the BFO/DSO film are inset in the $(001)_{pc}$ RSM for that sample.

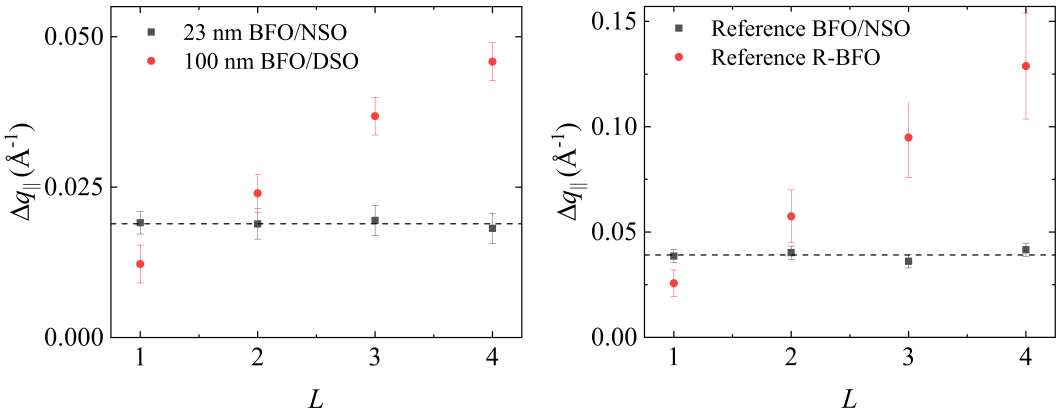

Figure 8.3: Splitting of satellite peaks for $(00L)_{pc}$ reflections for BFO/NSO and reference rhombohedral (109° stripe domain) BFO/DSO samples used in this work (left) and by Yang et al. [197]. Data is extracted from cuts along $q_{||}$ in $(00L)_{pc}$ RSMs.

the film structure. There are two potential causes of peak splitting in symmetric RSMs; periodic domain modulation and Bragg reflections from crystallographically tilted domains. The way to distinguish these is to consider the spacing of these in $q_{||}$ for a series of Bragg reflections. The 23 nm BFO/NSO film exhibits two sets of satellite peaks. The pair of satellite peaks at higher $q_{\perp}$ have a equal spacing in all $(00L)_{pc}$ RSMs, which indicates the domains are very well ordered and have a narrow size distribution. The inner satellite peak separations are plotted clearly in Fig. 8.3 alongside data from a 100 nm BFO/DSO film with well ordered 109° stripe domains and reference data from similar samples in the study of Yang et al. [197]. For the BFO/NSO film by considering the spacing of inner satellites in $q_{||}$ it is possible to calculate the average domain width as 30 nm. This is consistent with the PFM data shown in Fig. 8.1. In contrast, the outer satellite peaks at lower $q_{\perp}$ for the 23 nm BFO/NSO sample are not equally spaced in $q_{\perp}$. The spacing is around 10% higher for $(004)_{pc}$ than $(003)_{pc}$. This is indicates that there is some tilting of the crystal structure in the regions these peaks correspond to. This effect is much weaker than for the thicker 100 nm BFO/DSO reference sample which has clear and distinct diffraction peaks from the tilted 109° domains but is within measurement resolution here. It is important to note that the central zero-order peaks here with $q_{||} = 0$ originate from the domain modulation structure [202].

These results suggest that the 23 nm BFO/NSO film contains two distinct types of regions. The first of these has a smaller out-of-plane lattice parameter (larger $q_{\perp}$) and is not significantly tilted. The second of these has a larger out-of-plane lattice parameter (smaller $q_{\perp}$) and is more tilted, but is still much

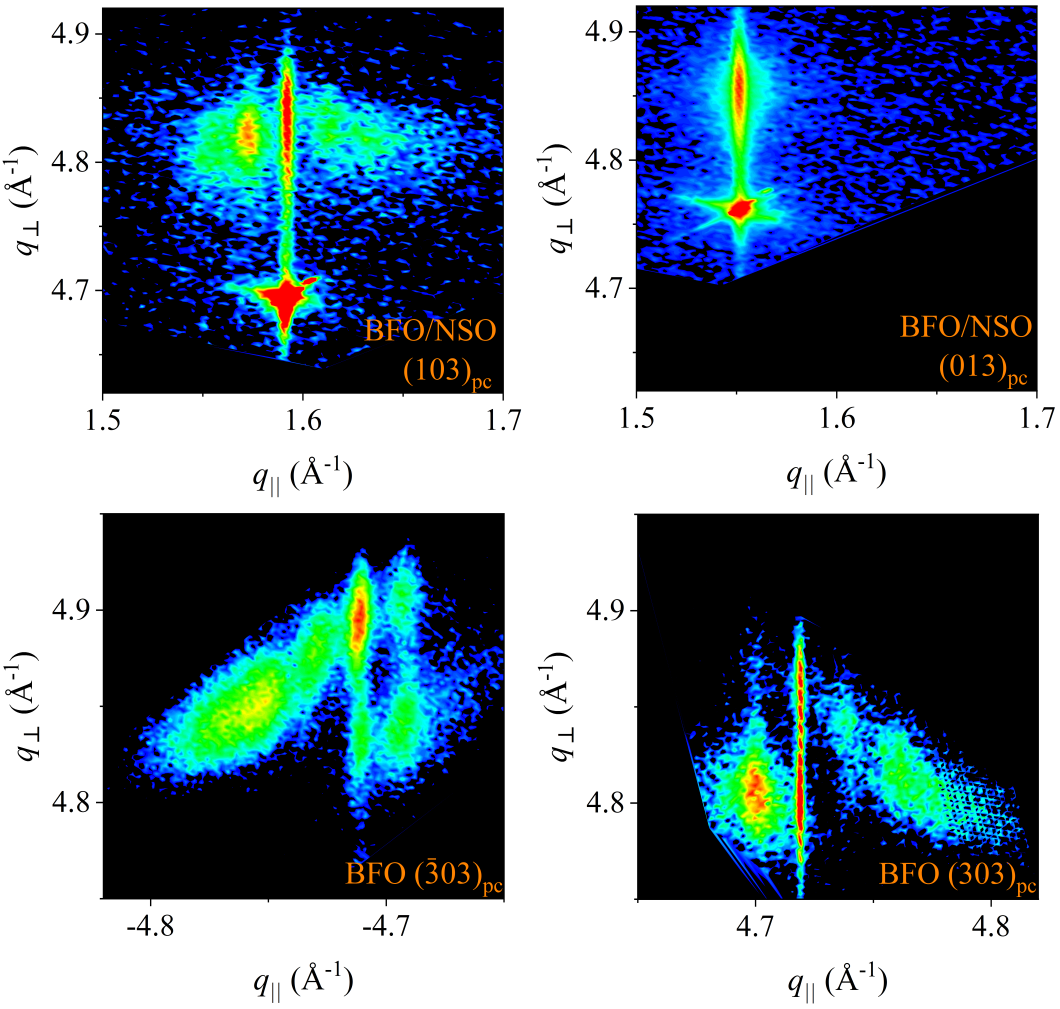

Figure 8.4: RSMs about the $(204)_{pc}$, $(024)_{pc}$, $(\bar{3}03)_{pc}$ and $(303)_{pc}$ Bragg reflections

less tilted than the reference 100 nm BFO/DSO sample. These regions may either be domain variants with different out-of-plane polarisation components or different structural phases. In order to learn more about the structure with XRD it is necessary to study the asymmetric peaks and access the in-plane information.

8.3.2 Asymmetric RSMs

Fig. 8.4 shows RSMs about four reflections: $(204)_{pc}$, $(024)_{pc}$, $(303)_{pc}$ and $(\bar{3}03)_{pc}$. From the RSMs about $(204)_{pc}$ and $(024)_{pc}$ it can be seen that the $BiFeO_3$ layer is completely strained to the in-plane lattice of the substrate. The peak positions in these two RSMs occur at different $q_{||}$ because the substrate presents two different in-plane lattice parameters. The spacing of inner satellite peaks from the

central $BiFeO_3$ peak is the same as that measured for $(00L)_{pc}$ peaks which confirms these peaks originate from periodic domain modulation. For all reflections with K≠0 no satellite peaks were present. Due to the apparent asymmetry in $q_{||}$ RSMs about $(303)_{pc}$ and $(\bar{3}03)_{pc}$ were measured. These peaks were chosen as they have a significant in-plane contribution.

This pair of RSMs clearly have different structures (both in terms of peak positions and intensity distributions) which suggests that structure here does not simply consist of a simple high symmetry phase. Instead it suggests that the structure is likely dominated by a low symmetry monoclinic phase. Lower symmetry phases are not expected here as it is already clear the $BiFeO_3$ layer is clamped to the $NdScO_3$ $(110)_o$ substrate surface, which presents a rectangular mesh and orthogonal pseudocubic a and b axes.

There are three types of polar monoclinic phase which could possibly be present: M_A, M_B, and M_C [203]. Stereographic projections of these are shown in Fig. 2.4. From the AFM images in Fig. 8.1 the presence of wedge disinclinations confirms the polarisation does not lay purely in the plane, ruling out the possibility that the majority phase has a M_C structure. Due to the tensile strain applied by the substrate it is obvious that M_B is a more favourable structural choice than M_A. M_A and M_B structures both belong to the space group Cc, and polarisation is aligned with the $<11w>_{pc}$ directions. For the case w>1 the structure is M_A and for the case that w<1 the structure is M_B. When w is close to zero or one it is possible to describe the structure as 'orthorhombic-like' or 'rhombohedral-like' respectively. It is possible that the structure of the film here is similar to that reported for $BiFeO_3$ on $PrScO_3$ substrate by Chen et al. [195], which purely consists of a M_B structure. The pseudocubic unit cell associated with the M_B unit cell is shown schematically in Fig. 8.5. It is more convenient to work in terms of this than the monoclinic unit cell, which is doubled and rotated by $45°$ in the a-b plane (with respect to the primitive pseudocubic unit cell). The monoclinic c-axis is tilted away from the vertical towards a $[110]_{pc}$ direction. In this structure all domain variants have the same out-of-plane polarisation component. This means that origin of the additional satellite peaks is a second structural phase.

The asymmetry in these reciprocal space maps demonstrates that not all monoclinic structural variants are equally present. Three possible reasons for this are i) the distortion of the pseudocubic NSO unit cell where the c-axis is deflected towards the $[010]_{pc}$ direction and ii) the substrate miscut. It is reasonable to expect that monoclinic structural variants which are aligned with these quantities are favoured above those that are not.

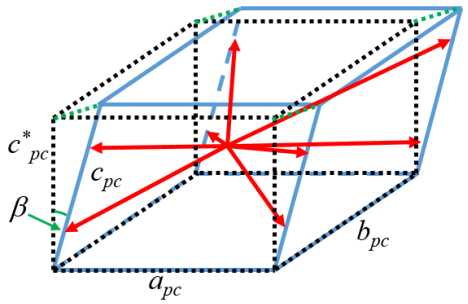

Figure 8.5: Primitive pseudocubic unit cell associated with M_B unit cell. The undistorted pseudocubic unit cell is shown in black, monoclinically tilted structure in blue, energetically favourable polarisation directions in red, and features to do with the monoclinic distortion are shown in green. Note that the polarisation is not aligned pointing towards cube corners.

Normally the presence of multiple structural phases is a sign that one is near a phase boundary. Morphotropic phase boundaries have been investigated in a number of solid state solution systems including Pb(Zr,Ti)O_3, (1-x)[Pb($Mg_{1/3}Nb_{2/3}$)O_3]-x[$PbTiO_3$] and (1-x)[$Na_{0.5}Bi_{0.5}TiO_3$]-x[$BaTiO_3$], in ceramic, single crystal and thin film form. Two structural models which are consistent with the data presented here and reasonable in the context of the existing literature are i) a M_B phase coexisting with an orthorhombic $BiFeO_3$ phase and ii) a M_B phase coexisting with another low symmetry monoclinic phase. In order to be consistent with the data these two phases must have the same in-plane lattice parameters as the substrate and different out-of-plane pseudocubic lattice parameters. It is important to note that it is not possible to distinguish between the two proposed structural models with the XRD data presented here, as the pseoducubic cells for M_B and orthorhombic structures are both distorted. The distortion direction is different in each case. In order to test the structural models derived here a TEM specimen was prepared enabling the cross section perpendicular to the stripe domain direction to be viewed. The stripe domains run along the $[\bar{1}10]_o$=$[010]_{pc}$ direction, and this is the direction along which the cross section is viewed. In projection the polarisation in M_B regions is expected to be oriented at an angle <45° from the horizontal, and in orthorhombic regions any polarisation would be confined to purely in-plane directions. It is important to note that multiple orthorhombic phases of $BiFeO_3$ are stable, not all of which are ferroelectric.

8.4 TEM characterisation

Unlike XRD which samples an area average and AFM based methods which sample the surface response preferentially, TEM allows the atomic structure to be directly probed. As the dominant cause of ferroelectricity in $BiFeO_3$ is the displacement of the Bi ions it is possible to effectively map the polarisation by considering the relative shift between the Bi A-site sublattice and the Fe B-site sublattice. In other words, $-\mathbf{D}_{FB} \propto \mathbf{P}$ where $\mathbf{D}_{FB}$ is the displacement vector of the Bi A-site sublattice relative to the Fe B-site sublattice and $\mathbf{P}$ is the polarisation vector. It is important to remember that the output of this analysis is really the relative shift of these two sublattices. By assigning Born effective charges and assuming the in-plane component is the same in both in-plane directions it is possible to calculate polarisation from the ionic displacement, but due to the complex structures here it is not appropriate to make these approximations so so all discussions of polarisation should be considered as qualitative only.

The $BiFeO_3$ layer was found to mainly consist of $(001)_{pc}$ type domain walls, however in this projection the angle made with the horizontal axis was typically lower than the value of 45° which would be observed in an unstrained layer. There were also a low density of $(101)_{pc}$ type domain walls across which the polarisation appears to be reversed. These two architectures are as expected for a rhombohedral-like M_B phase, and are consistent with the PFM data. Specifically, the mesoscopic domain structure can be interpreted as bundles of 109°-like domain walls with 180° domain walls at superdomain boundaries.

In addition to these structures there were a number of regions where polarisation appeared significantly more aligned with either the in-plane or the out-of-plane direction. The purely in-plane orientation was far more often seen, and this is consistent with the symmetry of an orthorhombic or orthorhombic-like unit cell. With this information it is possible to propose that the structure of the $BiFeO_3$ layer here is dominated by a rhombohedral-like M_B phase but contains a significant volume of regions with other structures too.

In this section detailed structural investigations of the domains and domain walls are presented.

8.4.1 $(001)_{pc}$ type 109°-like domain walls

Polarisation, strain and rotation mapping

Fig. 8.6 shows polarisation, strain, and rotation maps for a region with two $(001)_{pc}$ type 109°-like domain walls. It also includes a histogram showing the angular distribution the polarisation. Components of strain and rotation matrices are calculated by geometric phase analysis as introduced in section 3.7.2. For all strain and rotation maps presented in this chapter the same scale (-0.05 to 0.05) is used.

From the polarisation map it is clear that there are two domain walls in this region. The domain walls are very narrow and in this image appear to be almost atomically sharp. Interestingly within each domain the polarisation appears to be textured, i.e. it is not homogenous. This is not normal. From the polarisation map there seems to be two dominant types of region: areas where polarisation makes an angle slightly less than 45° offset from that of the horizontal and areas where the polarisation makes an angle of $\approx \pm 20°$ with the horizontal. These two angles may be associated with the two M_B structures predicted from the XRD characterisation. The presence of a polarisation texture is indicative of a polar instability, which is normally associated with a phase transition. For the case of La-doped $BiFeO_3$ a phase transition from rhombohedral to an orthorhombic as the La doping level is increased. At this phase transition the polarisation loses its alignment within each domain and a texture like the one observed here is predicted but not observed directly [204].

The strain maps indicate that across the domain wall there is a strain field which has a maximum of around 2%. The component in x-y plane is much larger than the component in the x-x or y-y plane. This is expected as the angle of the polarisation is closer to 45° than 0° or 90°. The width of the regions where there is significant strain and rotation appears to be 2-3 u.c.. This is slightly larger than the length scale on which the polarisation appears to be is rotated.

From the histogram it is clear that the two peaks are not centred on multiples of 45°. From Gaussian peak fitting the centre of these peaks can be found to be around 32° on average offset from the horizontal, however from the edge of these fits it is clear that there are additional components towards 135° and 225° which are not fully accounted for.

In order to more quantitatively analyse the data here it is necessary to carry out a more detailed analysis.

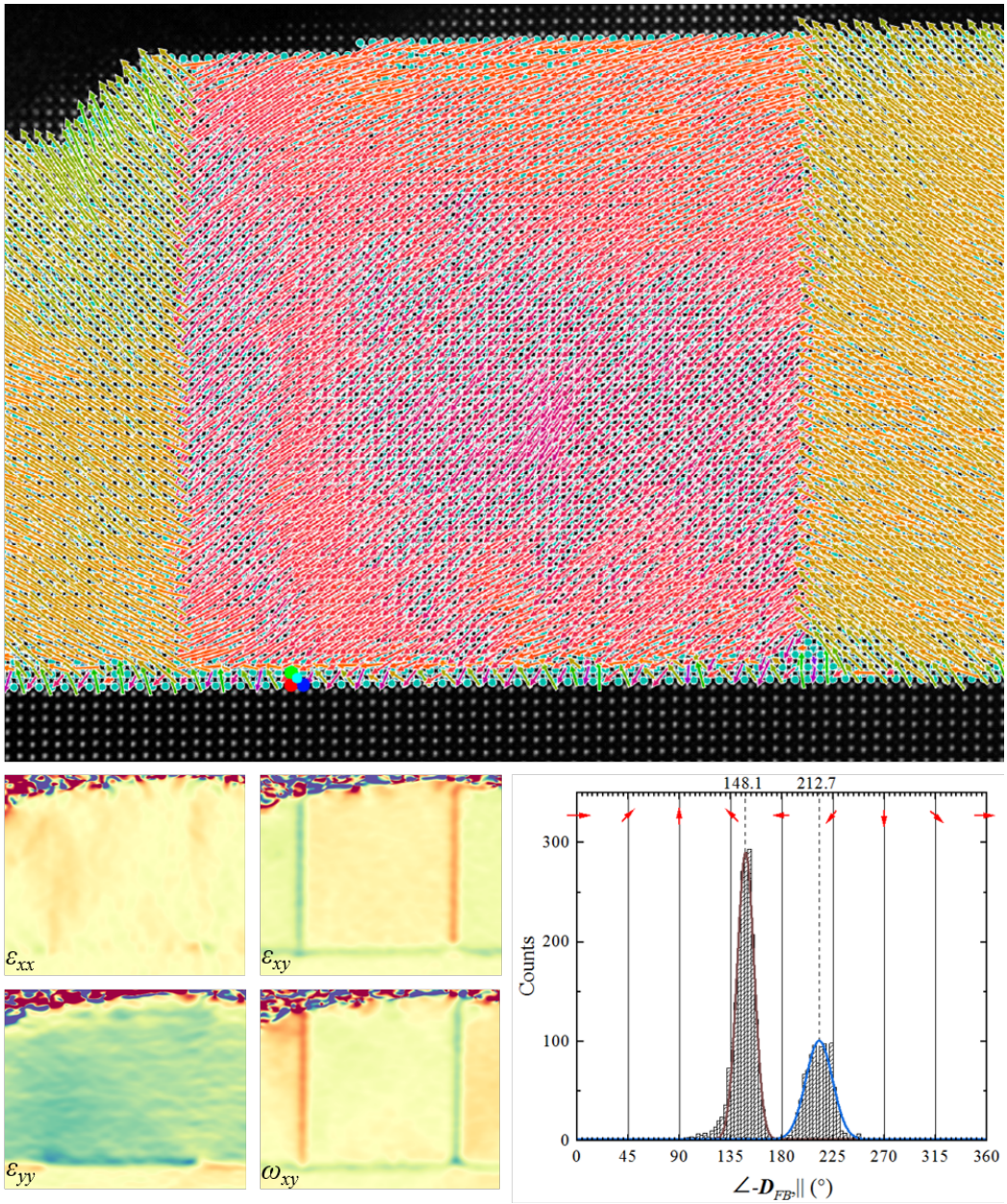

Figure 8.6: Polarisation, strain and rotation maps for a region of the BFO/NSO sample containing two 109°-like domain walls. Arrows indicate the polarisation direction and magnitude. The angular distribution of ionic displacement is shown in the histogram.

Structural features of domains close to and far from the substrate interface

Fig. 8.7 shows the evolution of several structural parameters as a function of the film thickness. These parameters are the out-of-plane lattice parameter L_y, the in-plane lattice parameter L_x, the rotation of the unit cell away from the value of 90° a cubic structure would exhibit δ (2δ can be considered as the domain mismatch angle), the magnitude of the ionic displacement vector $|-\mathbf{D}_{FB}|$, the angle the ionic displacement vector makes with the horizontal $\angle -\mathbf{D}_{FB,||}$, the out-of-plane component of the ionic displacement vector $\mathbf{D}_{FB}|_{\perp}$ and the in-plane component of the ionic displacement vector $\mathbf{D}_{FB}|_{||}$. Two area averages are considered. The first of these is the central domain which has polarisation pointing down and left. The second of these is the right hand domain which has polarisation pointing up and left.

In both domains the out-of-plane lattice spacing L_y can be seen to change significantly near the interface before it reaches an equilibrium value. The width of this transition layer is around 20 Å. Further to this, it can be seen that in this region the sign of the structural change is determined by the polarisation orientation. In contrast, the in-plane lattice spacing L_x and the rotation 2δ vary on a longer length scale with an interface layer of around 70 Å. It is interesting to note that despite both domains having essentially the same out-of-plane lattice spacing beyond the interface layer (within measurement uncertainty) the values of in-plane lattice spacing L_x they adopt are not the same. The right domain has a lower value of L_x than the mid domain. The explanation for these observations lies with the lattice rotation 2δ. Close to the interface the lattice rotation is suppressed such that it is almost zero and $BiFeO_3$ layer is driven to adopt a structure much closer matched to that of the substrate than that of bulk $BiFeO_3$. The strength of this effect is largest at the interface and decreases further away from the interface. A schematic of this and the effect on L_y, compression in the polarisation down domain and expansion in the polarisation up domain, is shown in Fig. 8.8.

It is interesting to compare the results of obtained here against those of Wang et al. [205] who undertook a study of the structural distortions in M_B $BiFeO_3$ films on $GdScO_3(110)_o$ (essentially unstrained, GSO) and $PrScO_3(110)_o$ (+1.5% tensile strain, PSO). Their samples only contain 109° stripe domains. For both unstrained and strained films they measure a transition layer of around 60 Å for 2δ. This is consistent with the data here, however the values of 2δ in the films here and that study are different. In both domains of the film here far from the interface the magnitude of 2δ is around 0.6°. In contrast, in the study of Wang et al. they measure 2δ values of 1.0° for their BFO/GSO sample and 0.8-0.9° for their BFO/PSO

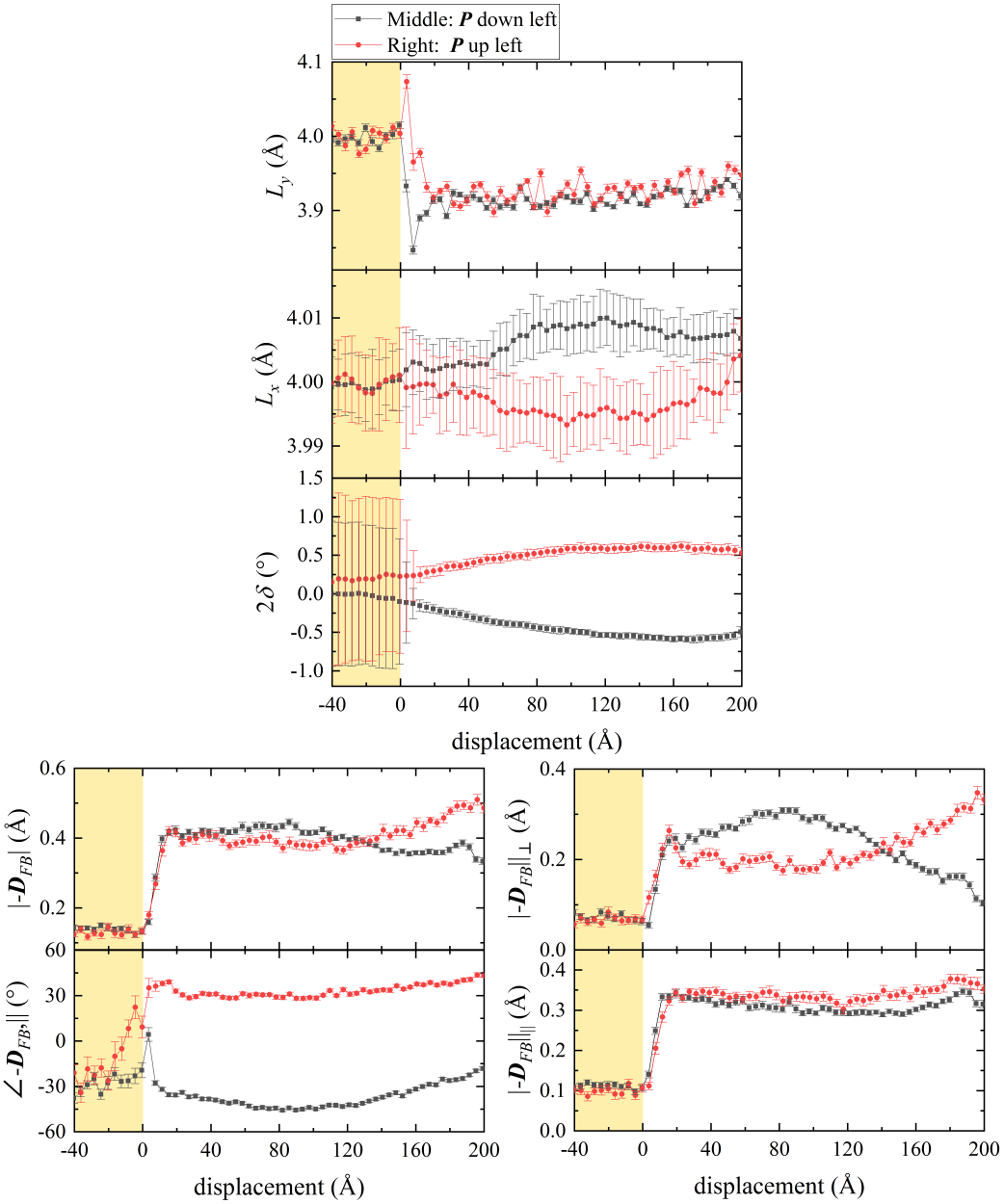

Figure 8.7: Vertical area averaged line profiles showing the lattice and polarisation structure as a function of the distance from the substrate-film interface for the middle and right domains in Fig. 8.6. The pale yellow region highlights the substrate.

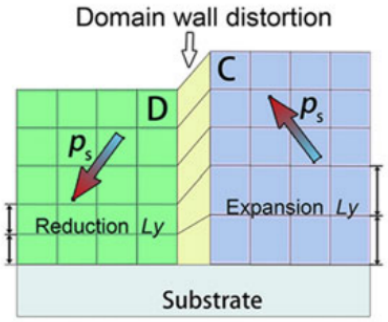

Figure 8.8: The effect of the epitaxial constraints of the substrate on the structure of the $BiFeO_3$ layer. Figure from Ref. [205].

sample. They also measure transition layer thicknesses in L_y of 20 Å and 8 Å in for these two samples respectively. Here the transition layer is around 15 Å. The differences between these values can be assigned to the strain imposed by the substrate, layer thickness, and processing conditions.

Transition layer thicknesses at or near interfaces are measures of the local structural distortions, and these are strongly linked to novel interface effects, especially those where different order parameters are coupled, ferroelectricity and ferroelasticity for example. In $BiFeO_3$ thin films a large amount of information is contained in the transition region for L_y, including that about the octahedral rotations [206], concentration of oxygen vacancies [207], and abnormal ferroelectric dipoles [208]. Tuning transition layer thicknesses is one method of controlling the novel emergent properties found at interfaces in these materials.

The magnitude of the ionic displacement vector $|-\mathbf{D}_{FB}|$ is similar in both domains. Near the interface it is suppressed, but it rapidly increases to its maximum value of around 0.4 Å within the same transition layer that L_y experiences. These two parameters go hand-in-hand, and the compression or expansion of L_y in the transition region does not significantly effect the magnitude of this quantity, which is an effective measure of polarisation. The angle which the ionic displacement vector makes with the horizontal is clearly different in both domains, and this difference between them can be measured to be in the range 60-65°. This is consistent with the histogram result in Fig. 8.6. This is very different to the case of unstrained $BiFeO_3$ where a value of 90° is expected. There are two reasons for this. The first is that each domain contains regions where the polarisation has a larger in-plane component than expected for the pure rhombohedral-like M_B phase which is predicted. These are correlated with the regions where the polarisation is oriented more in-plane than

out-of-plane. The second reason is due to the tensile strain of the substrate causing a distortion the unit cell such that the out-of-plane lattice spacing is significantly lower than the in-plane lattice spacing.

The out-of-plane component of the ionic displacement vector $-\mathbf{D}_{FB}|_{\perp}$ shows opposite trends for the two different domains after the interface region. In contrast, beyond the interface region the in-plane component of polarisation is effectively the same for each domain. The difference in the behaviour of $-\mathbf{D}_{FB}|_{\perp}$ can be linked to the asymmetrical lattice distortions in each of the 109°-like domains which result from the different polarisation orientations on the $BiFeO_3$ structure, which is quite strongly clamped to the substrate.

Structure of 109°-like domain walls

Fig. 8.9 shows a detailed structural analysis of 109°-like domain walls. The region considered is that shown in Fig. 8.6. Three area averaged regions are considered.

The structural deformation across the domain wall here is very different to that of the substrate-film interface. Close to the substrate L_y clearly has different values in each domain. This is a result of the polarisation induced structural deformation. Further from the substrate, where the clamping effect is weaker the variation of L_y is smaller and the signal is dominated by the polarisation texture in each domain. at the domain walls L_x clearly increases, which is consistent with the observation that the polarisation at the domain walls has a large in-plane component. The value of 2δ at the domain walls is very large, around 6°. This is comparable to the value of 7° Wang et al. obtain for a BFO/GSO sample [205]. Unlike the substrate-film interface the transition layer of the domain wall in 2δ is just around 10 Å thick. Close to the substrate-film interface there is a clear transition region in L_y which is large around 35 Å in width, which is significantly larger. The data for L_x does not show a transition layer clearly. The difference between the transition layer widths in 2δ and L_y shows that the length scale on which the out-of-plane lattice spacing adopts its equilibrium value is significantly larger than that on which the unit cell rotation changes. For this case the in-plane lattice spacing is quite strongly clamped to the substrate throughout the $BiFeO_3$ layer, meaning that the structural changes are mostly in the out-of-plane component.

The magnitude of the ionic displacement vector is similar in each domain but noticeably does decrease at the domain wall. This is compatible with the discussion of the ferroelectric switching pathway presented in Chapter 6 and existing literature [166]. The amount by which $|-\mathbf{D}_{FB}|$ decreases at the domain walls seems to

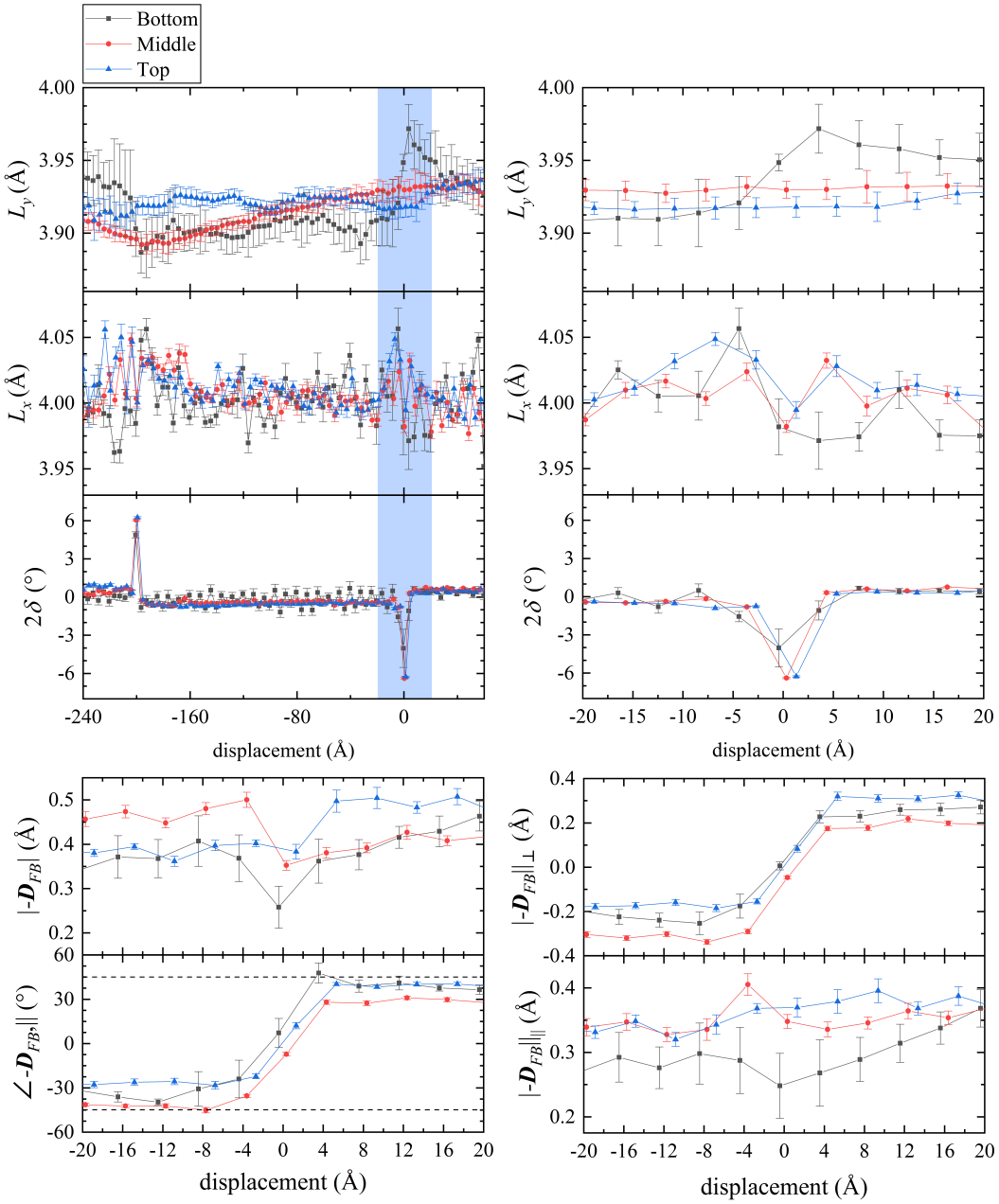

Figure 8.9: Horizontal area averaged line profiles showing lattice and polarisation structures across 109°-like domain walls for the region shown in Fig. 8.6. The blue highlighted region is the right hand domain wall, and zooms of this region showing the fine domain wall structure are presented.

be strongly linked to the distance from the substrate-film interface. Close to the interface the difference is stronger, and further away it is less prominent. The clamping effect of the substrate is clearly related to the magnitude of polarisation at the 109°-like domain wall. Across the domain wall the angle the ionic displacement vector makes with the horizontal is around 70°, a larger value than is measured from Fig. 8.7. This either indicates that near domain walls the rhombohedral-like M_B structure is preferentially found or that it is favourable to have structural variants each side of the domain wall which are relatively perpendicular. It is clear that the in-plane component of polarisation close to the substrate is suppressed. This is because it includes the transition layer region. Further away from the substrate-film interface this quantity adopts a higher value. In contrast, the out-of-plane component of polarisation at the domain wall does not seem to be affected by the clamping effect. The length scale on which the polarisation varies is the same as that of 2δ, and the fact that this is different to the width of the transition layer for L_y does not seem to affect the polarisation structure.

8.4.2 $(101)_{pc}$ type 180° domain walls

Polarisation, strain and rotation mapping

Fig. 8.10 shows polarisation, strain and rotation maps for an area consisting one 109°-like domain wall and one 180° domain wall.

The structure of the 109°-like domain wall in this area is similar to those in Fig. 8.6. There are a few interesting features to note in this image beyond the 180° domain wall though. In the domains either side of the 109°-like domain wall the polarisation is textured and almost entirely consists of two variants, one with polarisation making a roughly 40° angle with the horizontal and the other making a smaller angle. In contrast, the domain on the right hand side of this region shows a richer structure which features regions with purely in-plane polarisation (indicating a orthorhombic structure) as well as regions with purely out-of-plane polarisation (indicating a tetragonal-like structure) are also present. The region with out-of-plane polarisation resembles that shown in the work of Li et al. [102] who demonstrate that the polarisation bound charge at charged domain walls may act to stabilise a tetragonal-like structure in relatively unstrained rhombohedral-like $BiFeO_3$ thin films on $TbScO_3(110)_o$. The appearance of a similar feature here suggests that even in the presence of a large tensile strain a tetragonal-like $BiFeO_3$ structure can still be stabilised. The same study showed that small regions with in-plane polarisation may also coexist, however the form of the so-called 'unusual

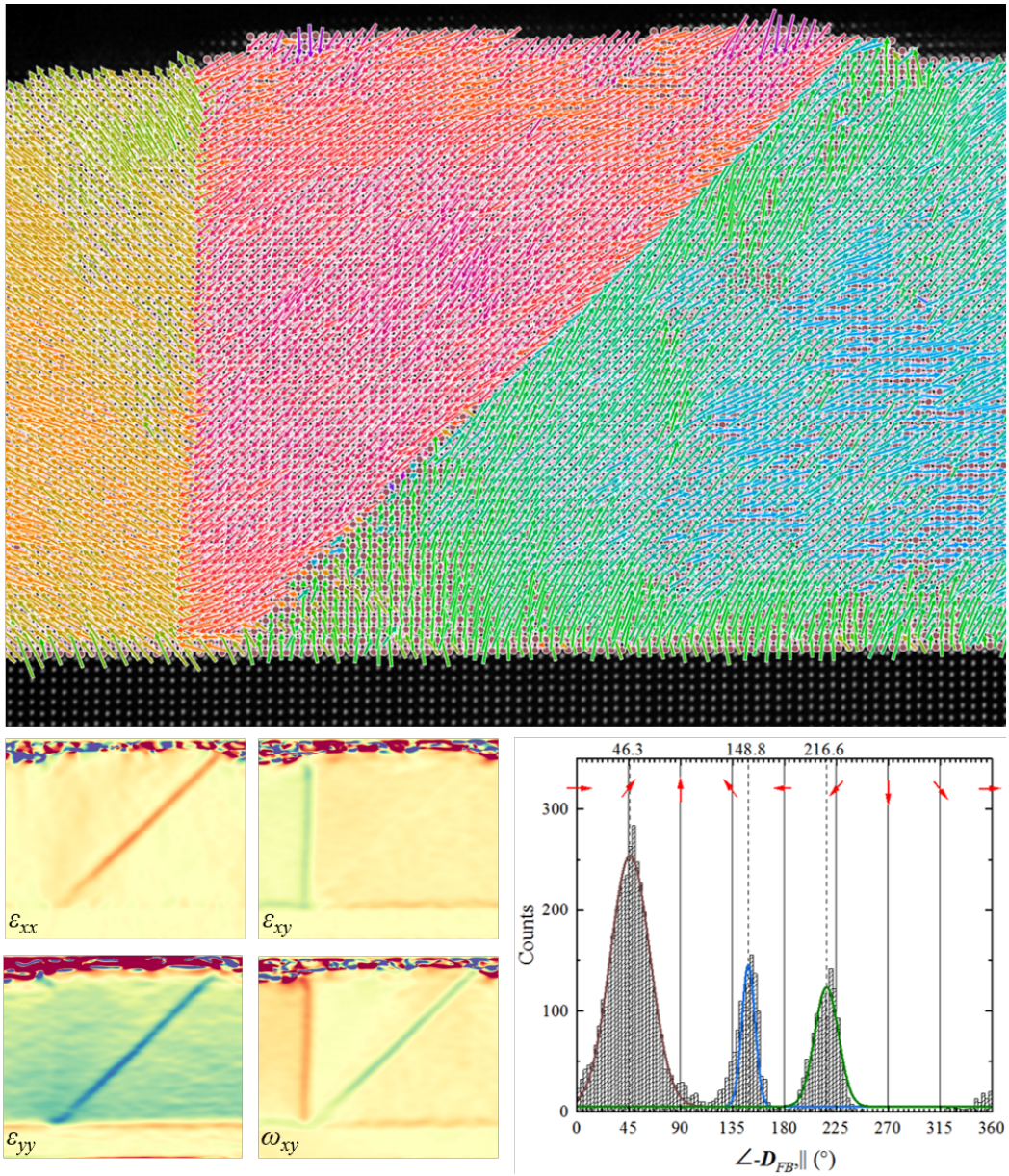

Figure 8.10: Polarisation, strain and rotation maps for a region of the BFO/NSO sample containing one 180° domain wall and one 109°-like domain wall. Arrows indicate the polarisation direction and magnitude. The angular distribution of ionic displacement is shown in the histogram.

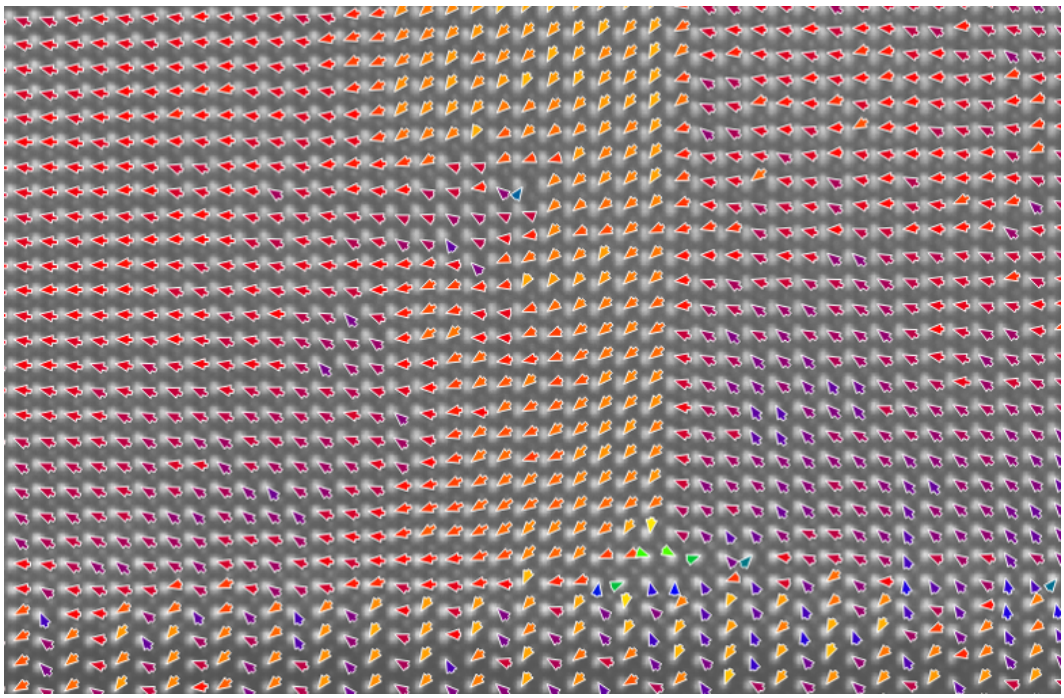

Figure 8.11: Ionic displacement map of BFO/NSO film near the substrate-film interface. The thickness of the BFO layer shown is around 9.6 nm, which is around half the film thickness. Unlike all other polarisation maps presented here these arrows indicate the polarisation direction but not magnitude.

nanodomains' here are quite different to in that work. Here they are more prevalent and are not found near the domain boundary, but are instead found within what would in the unstrained case be untextured domains. This indicates they may be stabilised strain instead of bound charge. It also possible that they may be stabilised by another mechanism though, as the regions with purely in-plane polarisation are only found directly above areas where the $BiFeO_3$ near the substrate has purely out-of-plane polarisation, i.e. on top of the tetragonal like regions, but observations of another region in this sample, show in in Fig. 8.11 prove this is not the case. This figure, where the ionic displacements of the $NdScO_3$ substrate are mapped along with the $BiFeO_3$ layer, proves that the polarisation texture does not originate from drift during data acquisition. The origin of the ionic displacements in the substrate crystal lie with the monoclinic distortion of the pseudocubic unit cell

Despite the rich polarisation structure it is of note that the only regions to clearly give contrast in strain and rotation maps are the main 109°-like and 180° domain walls which span the entire film thickness. From the contrast in the strain maps it is clear that the structural deformation at the 180° domain wall is larger

than that of the 109°-like domain wall.

The Gaussian fits on the histogram clearly show that it is not sufficient to only fit three main polarisation orientations here. The features at 0°/360° and 90° are clearly not well fitted by these. Interestingly the peaks are consistent with there being components aligned well with 45° and 225°, which is consistent with a rhombohedral-like structure. From this observation and the polarisation map it may be concluded that it is favourable for the structure at the 180° domain wall to adopt a rhombohedral like phase. This is consistent with the data in Fig. 8.6.

Structure of 180° domain walls

As for the 109°-like domain wall, in order to carry out a quantitative analysis it is necessary to consider line profiles. Fig. 8.12 shows a detailed structural analysis across the 180° domain wall. It is important to note that in this case the cross section is perpendicular to the domain wall, i.e. is inclined at a diagonal instead of along the horizontal. Two area averages are considered. These are labelled 'top' and 'bottom'

The structure of this domain wall is very different to that of the 109° domain walls. In this case the domain wall is similarly sharp in both L_y and 2δ and there appears to be no transition layer anywhere to be seen. Across the domain wall the out-of-plane lattice spacing is dramatically reduced, but the amount by which it is reduced is larger further away from the substrate-film interface. This is because the clamping effect in this region is strong and the unit cell rotation is smallest. The effect of this is that the amount by which L_x may be changed across the domain wall is restricted close to the substrate-film interface, which in turn affects the variation of L_y. The amount by which L_y and L_x change across the domain wall is far larger than the case of 109° walls. In fact, the effective local tensile strain associated with this structural deformation in the domain wall region can be calculated to be around 5%. This is significant. Like the 109°-like domain wall the spacial extent of the domain wall region is just a few unit cells. The value of 2δ is smaller for the 180° domain wall than the 109°-like domain wall because despite the structural variation the two domains share a common polar axis, hence the domain wall is not ferroelastic. Interestingly Wang et al. [166] observe no change in L_x across 180° domain walls in their BFO/TSO thin films, which were prepared by MBE and have an effectively rhombohedral structure.

Across the domain wall the magnitude of the ionic displacement vector changes significantly. Due to the the presence of the tetragonal-like region near the substrate-film interface it is most informative to consider the top region only when looking for the effect of the 180° domain wall structure. From the data it

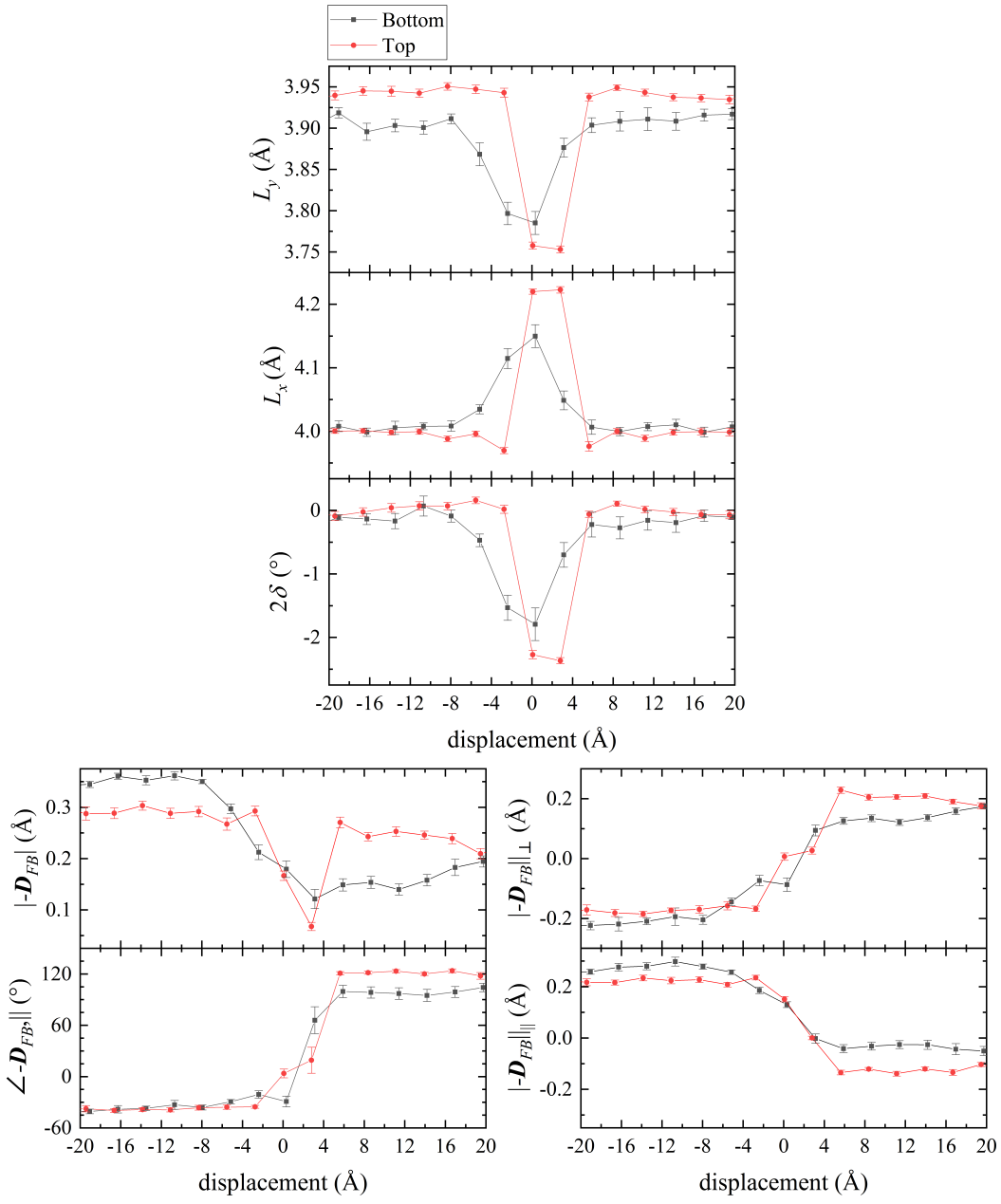

Figure 8.12: Area averaged line profiles perpendicular to the 180° domain wall showing lattice and polarisation structures. The domain wall analysed here is shown in Fig. 8.10.

can be concluded that the polarisation at the domain wall is suppressed by around 70%. This is significantly more than for the 109° case where the suppression is around 20%. The angular difference between the two domains is measured to be around 160°. This is again below the expected value because this measurement is area-averaged and includes regions where the polarisation is textured, including regions where the in-plane component is larger than that of the majority expected rhombohedral-like M_B structure. Each side of the domain wall the perpendicular components of the ionic displacement vector are roughly equal and opposite.

Although the sample here has a clear stripe domain pattern, the TEM characterisation so far has demonstrated that the structural make up of the sample is more complex than it may initially appear. So far regions with tetragonal-like, orthorhombic-like, and rhombohedral-like structures have all been shown to coexist and the polarisation within each domain is surprisingly inhomogeneous. This lends support to the hypothesis that the complex structure here is a result of strain imposed by the substrate and is a sign that this sample is the vicinity of the predicted morphotropic phase boundary like- strain-induced phase boundary.

8.5 Photoelectric characterisation

In the previous section the structure of the BFO/NSO sample has been investigated. Although it contains a range of interesting features, it mostly consists of 109°-like stripe domains. For this reason it is interesting to compare its photoelectric response against the essentially unstrained but otherwise similar 109° stripe domain BFO/TSO samples of Bhatnagar et al. [209]. Those films showed no polarisation instabilitiy (i.e. textured polarisation and multiphase structure). Au top electrodes (deposited by e-beam evaporation) with a length of 700 μm and a gap of 80 μm were used to form the devices.

8.5.1 Abnormal photovoltaic effect

To gain some insight into the effect of the polarisation structure and domain walls on the photovoltaic effect two device geometries are considered here. In the first geometry, referred to as PPDW the domain walls are aligned perpendicular to the electrode edge. In the other, referred to as PLDW, the domain wall are aligned parallel to the domain wall edge. The sample was photoexcited using linearly polarised illumination from a 405 nm (3.06 eV) laser which was aligned with the electrode gap in such a way that the photocurrent was maximised. To

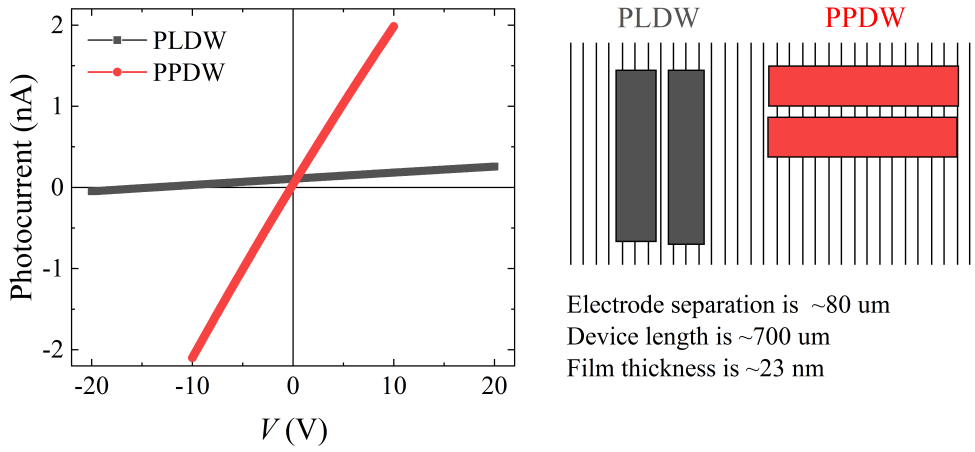

Figure 8.13: Left: photocurrent-voltage behaviour of PLDW and PPDW devices at 300 K. Right: schematic of PLDW and PPDW device geometries.

probe the photovoltaic effect I-V curves were measured with and without the laser illumination. A schematic of each device geometry along with the photocurrent response at 300 K is shown in Fig. 8.13.

The response of this sample resembles that of the 109° stripe domain samples of Bhatnagar et al. [209]. In the PLDW device geometry a very large open circuit voltage (V_{oc}) of 13.8 V was measured. This larger than the 2.5-2.7 eV band gap of $BiFeO_3$. In contrast, the open circuit voltage for the PPDW case is just 0.02 V. In order to further compare the behaviour of this sample against the case of relatively unstrained films with 109° stripe domains similar measurements were made at a range of temperatures between 85 K and 400 K.

8.5.2 Temperature dependent measurements

The open circuit voltage of a device is dependent on the photo-induced current J_{sc}, the dark conductivity σ_{dark}, the photoconductivity σ_{ph} and the device length L. The photoconductivity is defined by the gradient of the current-voltage curve under illumination. This can be expressed as $\frac{I_{sc}}{V_{oc}}\frac{L}{A}$ where A is the cross sectional area of the device as $I_{sc}V_{oc}$ defines the gradient of the current-voltage curve under illumination. The temperature dependence of V_{oc} is given [77, 210] by

$$V_{oc} = \frac{J_{ph}L}{\sigma_{dark} + \sigma_{ph}}. \tag{8.1}$$

Fig. 8.14 shows the temperature dependence of the open circuit voltage, short circuit current and photoconductivity. As can be expected due to the

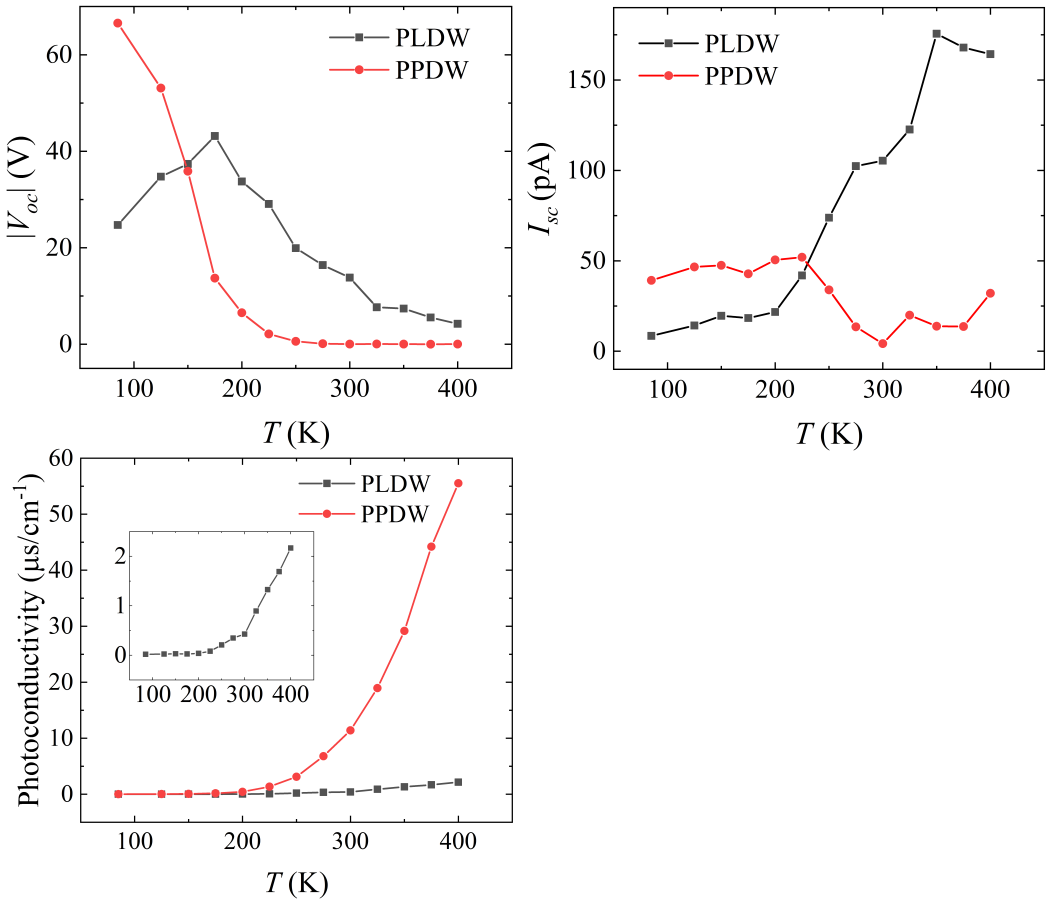

Figure 8.14: Temperature dependence of V_{oc}, I_{sc} and photoconductivity. The inset shows a zoom of the PLDW data series.

conducting nature of domain walls the PPDW geometry has a significantly higher photoconductivity than the PLDW geometry. As the dark conductivity was consistently at least two orders of magnitude lower than the photoconductivity it was excluded from the analysis as its effect on other parameters was negligible.

The PPDW case closely resembles the results of Bhatnagar et al. [209] indicating the stripe domains dominate the behaviour in this device geometry. For this case V_{oc} is low as the number of potential barriers charge carriers experience as they traverse the lattice while travelling towards an electrode is effectively small. In contrast, the PLDW case is different to what has been observed previously as the open circuit voltage features a maximum at around 200 K. It is normally expected to increase monotonically as temperature is decreased. To meaningfully discuss this feature it is necessary to consider the theory. As $\sigma_{dark} < \sigma_{ph}$ by at least a factor of 10^2 in these measurements the term σ_{dark} can be neglected. Similarly, L is a constant, and can be dropped when re-expressing Eqn. 8.1 as

$$V_{oc}(T) \propto \frac{J_{ph}}{\sigma_{ph}(T)}. \tag{8.2}$$

For the case of BFO/TSO films with 71° or 109° stripe domains it has been demonstrated by comparing the temperature dependence of σ_{dark} and σ_{ph} with that of V_{oc} that J_{ph} is essentially temperature independent and constant for a given device [77]. If that is true, it is possible to further simplify Eqn. 8.2 to

$$V_{oc}(T) \propto \frac{1}{\sigma_{ph}(T)}. \tag{8.3}$$

Clearly for the PLDW case of the BFO/NSO film here this relationship does not hold as there a maximum V_{oc} occurs at a temperature of 200 K whereas the temperature dependence of σ_{ph} is monotonic. This means that some other effect is at play. In order to discern whether this information comes from a temperature dependence of J_{ph} we can test the validity of Eqn. 8.3. If it is true for a pair of temperatures which are far apart then the temperature dependence of J_{ph} may indeed be neglected, proving the origin of the effect is the σ_{ph} term. Consider the ratio of V_{oc} and σ_{ph} at 85 K and 200 K. The result of this analysis for the PLDW case is $V_{oc}|_{200K}/V_{oc}|_{85K} = 1.746$ and $\sigma_{ph}|_{200K}/\sigma_{ph}|_{85K} = (1.873)^{-1}$. There is a 7% difference between these two ratios which is within measurement uncertainty. The dominant cause of measurement error was the recentering of the laser spot onto the electrode gap before at each temperature. Due to thermal drift in the cryostat used this was necessary. The agreement of these values establishes that J_{ph} can be

considered to be temperature independent (or at most, very weakly dependent on temperature), meaning that the maximum in V_{oc} at 200 K for the PLDW case arises purely from the temperature dependence of σ_{ph}. In order to gain insight into the physical mechanism behind the emergence of this effect it is necessary to consider this term in more detail.

The term σ_{ph} is a bulk property, the magnitude of which is determined by the geometrical parameters of the device, the open circuit voltage and the short circuit current. The physical interpretation of V_{oc} is that it is a measure of the potential that can be realised when photo-excited charge carriers are separated and no current is allowed to flow in the device. The physical interpretation of I_{sc} is that it is a measure of the current flow that can is realised when that same device is connected to a circuit. When considering carrier effects in the material the intuitive parameter to consider is the current as it describes the flow of charge carriers. At 200 K the temperate dependence of I_{sc} shows a clear elbow, which is indicative of a regime change. The short circuit current is dependent on the lifetime of carriers (which is inversely proportional to the recombination rate) and this is known to be dependent on lattice structure. For example, in the BFO/LAO system the relaxation processes are significantly different between the T-like phase and the mixed T-R phase due to structural strain, symmetry breaking, and built-in electric fields at phase boundaries [211]. In the sample here, with its polarisation texture and multiple phase variants, it is reasonable to expect that the structural makeup of the sample varies with temperature. This is known to occur in the BFO/LAO system where increasing temperature decreases the proportion of the sample that is made up by the R-phase in the T-phase matrix [212]. Fig. 8.15 shows strain-temperature, strain-polarisation and pressure-temperature phase diagrams for $BiFeO_3$ taken from the literature. From the structural investigations of the BFO/NSO film here and these phase diagrams it is reasonable to predict that as temperature is decreased the extent of the polarisation instability (i.e. polarisation texture) and amount of non-rhombohedral like M_B phases will decrease. The I_{sc} data can be interpreted as a prediction that in this sample at around 200 K the sample undergoes a transition to a structure which is single single phase, or at least does not exhibit the same polarisation instability and mixed phase structure.

It is relevant that it has been recently measured that the giant strain gradient at phase boundaries between T and R like phases in BFO/LAO exhibit a significant flexophotovoltaic effect, with one side of the boundary showing an enhanced photoconduction and the other showing a negative photoconduction [214]. In the BFO/LAO system, which has significantly more strain than the BFO/NSO case,

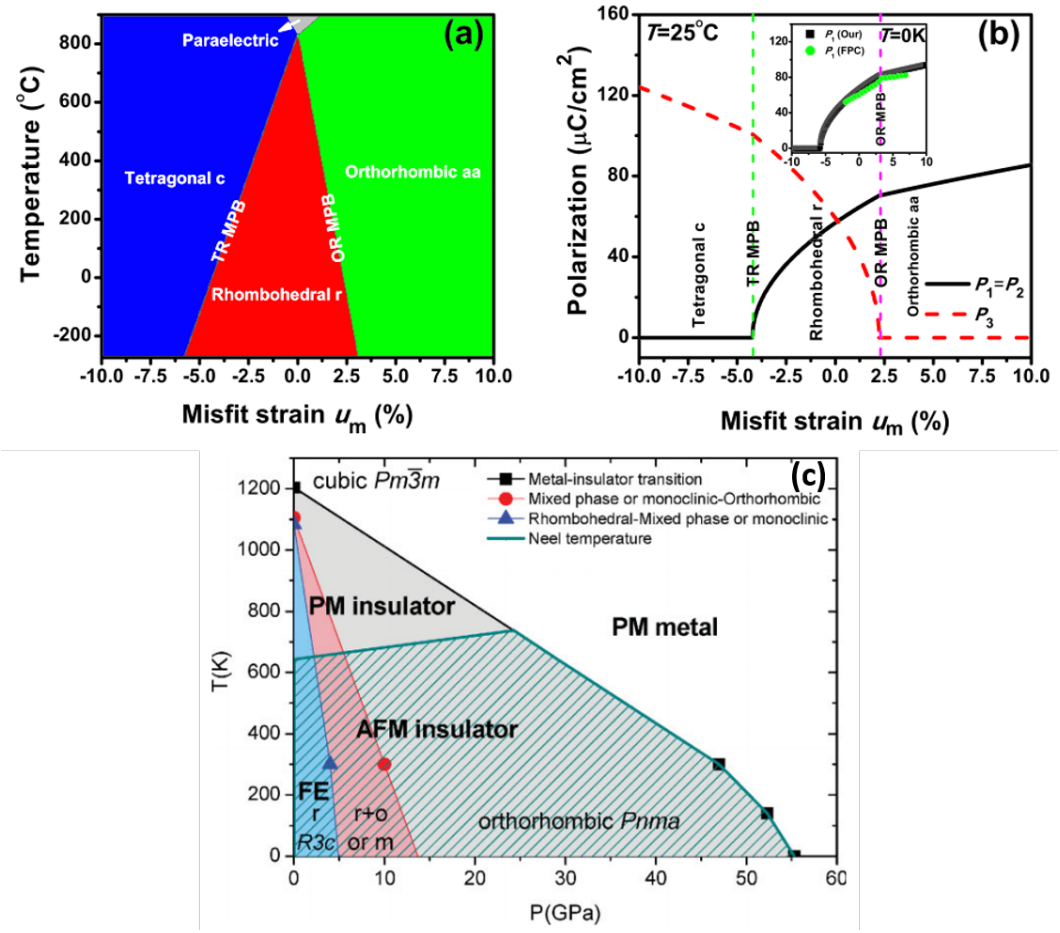

Figure 8.15: Phase diagrams of $BiFeO_3$. Figures from Ref. [193] and Ref. [213].

the mixed-phase nature of the sample has a significant effect on the photoexcited carrier dynamics. It stands to reason that the polar instability and emergence of a mixed phase in BFO/NSO may bring about in a similar effect which could explain the unexpected behaviour of I_{sc} and V_{oc} here. In order to further elucidate this temperature dependent structural or dielectric measurements of the BFO/NSO sample here are required.

It is important to note that in a mixed phase structure the BPV tensor will be much more complicated than the case of single phase essentially unstrained rhombohedral $R3c$ $BiFeO_3$ considered by Bhatnagar et al. [209]. To start with, the strained M_B phase has Cc symmetry instead of $R3c$ symmetry, so inevitably the components of the bulk photovoltaic effect tensor, and also the photocurrent and structural dynamics, will be different in the more complex case here.

8.6 Chapter summary

In this work a mixed-phase $(001)_{pc}$ oriented $BiFeO_3$ film with a regular domain pattern has been stabilised for the first time under tensile epitaxial strain. Unlike similar films in the literature by both advanced XRD and TEM characterisation methods this sample features both the theoretically expected M_B phase and more orthorhombic-like phases. The instability in polarisation and coexistence of structural phases suggests that this sample is near the strain-induced phase boundary. Detailed structural investigation of the domains, regular 109°-like domain walls and 180° domain walls have been made and compared against those in the literature. This sample features an anomaly in its photoelectric response which indicates that at a temperature of approximately 200 K the film undergoes a phase transition and moves into a single phase structural state.

Chapter 9

Conclusions and future work

In this thesis a number of investigations studying the motion, structure and properties of domain walls have been presented.

In Chapter 4 it was demonstrated that PFM and dielectric characterisation are complementary methods which together provide a more complete understanding of the dynamical behaviour of domain wall motion. The hyperbolic law has been shown to be an appropriate framework to analyse the domain wall motion in $PbZr_{0.2}Ti_{0.8}O_3$ and the frequency and temperature dependence of the motion of 90° domain walls to the dielectric permittivity have been systematically studied. It was even possible to calculate the activation energy required to depin these domain walls. The value obtained, 70 ± 10 meV, is consistent with theoretical predictions. It would be interesting to apply the methodology employed here to other simple systems such as $BaTiO_3$ and $PbTiO_3$ but also more complex systems like $BiFeO_3$. In particular, it would be interesting to compare the domain wall motion in BFO/LSMO/DSO capacitor devices with either 71° stripe domains or 109° stripe domains, or even the $BiFeO_3$ sample studied in Chapter 5 where the domain configuration at different switching states can be probed directly with PFM. In order to further understand the defect structure it would be informative to carry out detailed NMR, EPR, and TEM measurements. That would help clarify the exact physical process with which the depinning energy is calculated.

In Chapter 5 the evolution of the domain pattern in $BiFeO_3$ capacitor devices with an initial 71° stripe domain pattern in various switching states has been determined for the first time. As previously reported, this switching process was repeatable. In the down and up states the domain pattern consists purely of 71° stripe domains. In the half switched state 109° domain walls emerge, mostly at the boundaries of bundles of 71° domain walls. This is consistent with and extends the

observations of the AFM based measurements of Yang et al. [163]. The length of 109° walls was found to be closely connected to the device conductivity and by the combination of PFM and electrical data the resistivity of each type of domain wall present was directly evaluate. The data here elucidates the conclusions of reports in the literature of the low temperature magnetotransport properties of domain walls and strongly suggests that the ferromagnetism associated with the magnetic moment of domain walls in the study of Lee et al. [160] are specifically associated with the 109°. Further to this the resistivity of the domain walls in undoped $BiFeO_3$ have been calculated at 80 K, and the value obtained is in reasonably consistent with the value predicted previously by Lee et al. [160] for Li-doped $BiFeO_3$. The combination of methods used here is demonstrated to provide a pathway to probe the electrical properties of domain walls in $BiFeO_3$ in temperature regimes where this information is otherwise inaccessible. There is no reason why this methodology cannot be extended to other systems. It would be interesting in future to measure the electrical response of domain walls in $BiFeO_3$ in this experimental geometry and compare the results against those of Domingo et al. [121] whose C-AFM based measurements at room temperature show that the orientation of domains has a significant effect.

In Chapter 6 a number of aspects of the polarisation switching dynamics in $(001)_{pc}$ oriented $BiFeO_3$ were revealed. Firstly, it was been demonstrated that the time-resolved experiments used here are not appropriate to probe the domain dynamics of $BiFeO_3$ with, as after significant cycling the as-grown domain structure is effectively erased and a more monodomain structure is stabilised. It is however possible to extract the dynamics at the unit cell level. The ferroelectric switching was been found to consist of an initial in-plane rotation, after which the value of polarisation is temporarily suppressed, followed by the polarisation flipping upwards to complete its reorientation to an end state which is offset from its start state by 71°. Further to this, the strain imposed by the substrate is found to have a significant effect on the timescale of the switching dynamics. When the $BiFeO_3$ layer is deposited on $SrRuO_3$ buffered $DyScO_3$ it is essentially strain free and ferroelectric switching proceeds quickly, unhindered by the relatively slow processes of creep motion or the oxygen octahedral dynamics. These processes are present when an $SrRuO_3$ buffered $SrTiO_3$ substrate, which exerts a compressive strain, is used. This investigation followed on from similar measurements on $PbZr_{0.2}Ti_{0.8}O_3$ films where the switching pathway was similarly revealed [174]. It would interesting in the future to further investigate the effect epitaxial strain has on the switching dynamics at the unit cell level and continue applying the method used here to other systems.

In Chapter 7 was demonstrated that it is possible to accelerate and enhance ferroelectric switching in both $BiFeO_3$ and $BaTiO_3$ metal-ferroelectric-metal capacitor structures by launching a compressive acoustic strain wave through the ferroelectric layer during polarisation reversal. This mechanism effectively allows the fundamental speed limit on the ferroelectric switching process, the domain wall velocity to be broken. The fluence, arrival time of the laser pulse with respect to the applied field and pulse duration are all shown to be important factors. By measuring the enhancement of polarisation reversal with pulses of different duration it was possible to distinguish the strain wave effect from simple heating. In the future it would be interesting to carry out investigations at higher fluence which would hopefully reveal a stronger effect. Also it would be informative to carry out a more systematic study with a series of samples with different bottom oxide electrode thickness, as that parameter will affect the strength and dynamics of the laser-induced strain wave experienced by the ferroelectric layer.

Finally in Chapter 8 detailed structural measurements on a mixed-phase $BiFeO_3$ sample with $(001)_{pc}$ orientation and highly ordered stripe domains is studied. This is the first report of a mixed-phase sample with this kind of ordering under tensile epitaxial strain. Two main phases are present, a rhombohedral-like M_B phase and a more orthorombic-like M_B phase. Detailed structural measurements with XRD and TEM are presented. The existence of a mixed-phase structure was associated with being in the proximity of the predicted strain-induced phase boundary, a region where the piezoelectric and dielectric responses are predicted to become very large. The clear polarisation instability observed with TEM supports this analysis. Interestingly the photovoltaic response of the BFO/NSO sample here shows a shoulder in I_{sc} and a peak in V_{oc} at around 200 K. It is predicted that this may be associated with a phase transition to a single-phase M_B structure with a significantly reduced polarisation instability. In order to verify this, temperature dependent dielectric, XRD or TEM measurements are required. Given the novel structure stabalised here it would be interesting to deposit a similar sample on $PrScO_3$, a substrate which is isostructural to $NdScO_3$ but has larger lattice parameters so applies a larger tensile strain, in the exact same conditions. This sample would be expected to show even more exotic behaviour than the sample studied here.

As a final word, domain walls in ferroelectric and multiferroic systems continue to present a fascinating playground for fundamental physics. There are still many unanswered questions and it is my hope that the contributions of this thesis has contributed towards answering some of these. It will be exciting to see

how this field continues to develop, especially as it increasingly moves to focus towards applying the physics of domain walls in novel devices which are suitable for real-world applications.

References

[1] Salje, E. K. Multiferroic domain boundaries as active memory devices: trajectories towards domain boundary engineering. *ChemPhysChem* **11,** 940–950 (2010).

[2] Catalan, G., Seidel, J., Ramesh, R. & Scott, J. F. Domain wall nanoelectronics. *Reviews of Modern Physics* **84,** 119 (2012).

[3] Seidel, J. *et al.* Conduction at domain walls in oxide multiferroics. *Nature Materials* **8,** 229 (2009).

[4] Chiu, Y.-P. *et al.* Atomic-scale evolution of local electronic structure across multiferroic domain walls. *Advanced Materials* **23,** 1530–1534 (2011).

[5] Farokhipoor, S. & Noheda, B. Conduction through 71 degrees Domain Walls in $BiFeO_3$ Thin Films. *Physical Review Letters* **107** (2011).

[6] Guyonnet, J., Gaponenko, I., Gariglio, S. & Paruch, P. Conduction at domain walls in insulating $Pb(Zr_{0.2}Ti_{0.8})O_3$ thin films. *Advanced Materials* **23,** 5377–5382 (2011).

[7] Kim, D. J., Connell, J. G., Seo, S. S. A. & Gruverman, A. Domain wall conductivity in semiconducting hexagonal ferroelectric $TbMnO_3$ thin films. *Nanotechnology* **27** (2016).

[8] Sluka, T., Tagantsev, A. K., Bednyakov, P. & Setter, N. Free-electron gas at charged domain walls in insulating $BaTiO_3$. *Nature Communications* **4** (2013).

[9] Meier, D. *et al.* Anisotropic conductance at improper ferroelectric domain walls. *Nature Materials* **11,** 284–288 (2012).

[10] Wu, W., Horibe, Y., Lee, N., Cheong, S.-W. & Guest, J. R. Conduction of Topologically Protected Charged Ferroelectric Domain Walls. *Physical Review Letters* **108** (2012).

[11] Schroeder, M. *et al.* Conducting Domain Walls in Lithium Niobate Single Crystals. *Advanced Functional Materials* **22,** 3936–3944 (2012).

[12] Jiang, J. *et al.* Temporary formation of highly conducting domain walls for non-destructive read-out of ferroelectric domain-wall resistance switching memories. *Nature Materials* **17,** 49+ (2018).

[13] Bai, Z. L. *et al.* Hierarchical domain structure and extremely large wall current in epitaxial $BiFeO_3$ thin films. *Advanced Functional Materials* **28,** 1801725 (2018).

[14] Kittel, C. *Introduction to solid state physics* (Wiley New York, 1996).

[15] Robertson, J. High dielectric constant gate oxides for metal oxide Si transistors. *Reports on Progress in Physics* **69,** 327 (2005).

[16] Von Hippel, A., Breckenridge, R., Chesley, F. & Tisza, L. High dielectric constant ceramics. *Industrial & Engineering Chemistry* **38,** 7–1109 (1946).

[17] Ribes, G. *et al.* Review on high-k dielectrics reliability issues. *IEEE Transactions on Device and materials Reliability* **5,** 5–19 (2005).

[18] Shim, J. *et al.* Process–property relationship in high-k ALD $SrTiO_3$ and $BaTiO_3$: a review. *Journal of Materials Chemistry C* **5,** 8000–8013 (2017).

[19] Maex, K. *et al.* Low dielectric constant materials for microelectronics. *Journal of Applied Physics* **93,** 8793–8841 (2003).

[20] Volksen, W., Miller, R. D. & Dubois, G. Low dielectric constant materials. *Chemical Reviews* **110,** 56–110 (2009).

[21] Tagantsev, A., Sherman, V., Astafiev, K., Venkatesh, J. & Setter, N. Ferroelectric materials for microwave tunable applications. *Journal of Electroceramics* **11,** 5–66 (2003).

[22] Kong, L. B. *et al.* Electrically tunable dielectric materials and strategies to improve their performances. *Progress in Materials Science* **55,** 840–893 (2010).

[23] Lines, M. E. & Glass, A. M. *Principles and applications of ferroelectrics and related materials* (Oxford University Press, 2001).

[24] Nye, J. F. *et al. Physical properties of crystals: their representation by tensors and matrices* (Oxford university press, 1985).

[25] Martin, L. *et al.* Multiferroics and magnetoelectrics: thin films and nanostructures. *Journal of Physics: Condensed Matter* **20,** 434220 (2008).

[26] Hill, N. A. Why are there so few magnetic ferroelectrics? *Journal of Physical Chemistry B Publications* **104,** 6694 (2000).

[27] Setter, N. *et al.* Ferroelectric thin films: Review of materials, properties, and applications. *Journal of Applied Physics* **100,** 051606 (2006).

[28] Scott, J. Applications of modern ferroelectrics. *Science* **315,** 954–959 (2007).

[29] Dawber, M., Rabe, K. & Scott, J. Physics of thin-film ferroelectric oxides. *Reviews of Modern Physics* **77,** 1083–1130 (2005).

[30] Tagantsev, A. K., Cross, L. E. & Fousek, J. *Domains in ferroic crystals and thin films* (Springer, 2010).

[31] Streiffer, S. *et al.* Domain patterns in epitaxial rhombohedral ferroelectric films. I. Geometry and experiments. *Journal of Applied Physics* **83,** 2742–2753 (1998).

[32] Panda, P. K. & Sahoo, B. PZT to Lead Free Piezo Ceramics: A Review. *Ferroelectrics* **474,** 128–143 (2015).

[33] Mangalam, R., Karthik, J., Damodaran, A. R., Agar, J. C. & Martin, L. W. Unexpected Crystal and Domain Structures and Properties in Compositionally Graded $PbZr_{1-x}Ti_xO_3$ Thin Films. *Advanced Materials* **25,** 1761–1767 (2013).

[34] Jaffe, B., Cook, W. & Jaffe, H. *Piezoelectric Ceramics* (Academic Press, 1971).

[35] Noheda, B. *et al.* Tetragonal-to-monoclinic phase transition in a ferroelectric perovskite: The structure of $PbZr_{0.52}Ti_{0.48}O_3$. *Physical Review B* **61,** 8687–8695 (2000).

[36] Cross, E. Materials science - Lead-free at last. *Nature* **432,** 24–25 (2004).

[37] Vijatovic, M. M., Bobic, J. D. & Stojanovic, B. D. History and Challenges of Barium Titanate: Part II. *Science of Sintering* **40,** 235–244 (2008).

[38] KWEI, G., LAWSON, A., BILLINGE, S. & CHEONG, S. Structures of the ferroelectric phases of barium titanate. *Journal of Physical Chemistry* **97,** 2368–2377 (1993).

[39] Choi, K. J. *et al.* Enhancement of ferroelectricity in strained $BaTiO_3$ thin films. *Science* **306,** 1005–1009 (2004).

[40] Pradhan, S. & Roy, G. Study the crystal structure and phase transition of $BaTiO_3$–A pervoskite. *Researcher* **5,** 63–67 (2013).

[41] Moreau, J., Muchel, C., Gerson, R. & James, W. Ferroelectric $BiFeO_3$ x-ray and neutron diffraction study. *Journal of Physical Chemistry and Solids* **32,** 1315–& (1971).

[42] Neaton, J., Ederer, C., Waghmare, U., Spaldin, N. & Rabe, K. First-principles study of spontaneous polarization in multiferroic $BiFeO_3$. *Physical Review B* **71** (2005).

[43] Bucci, J. D., Robertson, B. K. & James, W. J. The precision determination of the lattice parameters and the coefficients of thermal expansion of $BiFeO_3$. *Journal of Applied Crystallography* **5,** 187–191 (1972).

[44] KUBEL, F. & SCHMID, H. Structure of a ferroelectric and ferroelastic monodomain crystal of the perovskite $BiFeO_3$. *Acta Crystallographica Section B: Structural Science* **46,** 698–702 (1990).

[45] Biswas, A., Yang, C.-H., Ramesh, R. & Jeong, Y. H. Atomically flat single terminated oxide substrate surfaces. *Progress in Surface Science* **92,** 117–141 (2017).

[46] Kawasaki, M. *et al.* Atomic control of the $SrTiO_3$ crystal surface. *Science* **266,** 1540–1542 (1994).

[47] Okazaki, A. & Kawaminami, M. Lattice constant of strontium titanate at low temperatures. *Materials Research Bulletin* **8,** 545–550 (1973).

[48] Müller, K. A. & Burkard, H. SrTi O 3: An intrinsic quantum paraelectric below 4 K. *Physical Review B* **19,** 3593 (1979).

[49] Leca, V., Rijnders, G., Koster, G., Blank, D. H. & Rogalla, H. Wet etching methods for perovskite substrates. *MRS Online Proceedings Library Archive* **587** (1999).

[50] Uecker, R. *et al.* Properties of rare-earth scandate single crystals (Re= Nd-Dy). *Journal of Crystal Growth* **310,** 2649–2658 (2008).

[51] Geller, S. Crystal structure of gadolinium orthoferrite, $GdFeO_3$. *The Journal of Chemical Physics* **24,** 1236–1239 (1956).

[52] Pintilie, L., Vrejoiu, I., Hesse, D. & Alexe, M. The influence of the top-contact metal on the ferroelectric properties of epitaxial ferroelectric $PbZr_{0.2}Ti_{0.8}O_3$ thin films. *Journal of Applied Physics* **104,** 114101 (2008).

[53] Bouchard, R. & Gillson, J. Electrical properties of $CaRuO_3$ and $SrRuO_3$ single crystals. *Materials Research Bulletin* **7,** 873–878 (1972).

[54] Callaghan, A., Moeller, C. W. & Ward, R. Magnetic interactions in ternary ruthenium oxides. *Inorganic Chemistry* **5,** 1572–1576 (1966).

[55] Jonker, G. & Van Santen, J. Ferromagnetic compounds of manganese with perovskite structure. *Physica* **16,** 337–349 (1950).

[56] Hwang, H., Cheong, S., Ong, N. & Batlogg, a. B. Spin-polarized intergrain tunneling in $La_{2/3}Sr_{1/3}MnO_3$. *Physical Review Letters* **77,** 2041 (1996).

[57] Urushibara, A. *et al.* Insulator-metal transition and giant magnetoresistance in $La_{1-x}Sr_xMnO_3$. *Physical Review B* **51,** 14103 (1995).

[58] Razak, N. A. A., Zabidi, N. A. & Rosli, A. N. *A first principle study of band structure of tetragonal barium titanate* in *AIP Conference Proceedings* **1875** (2017), 020017.

[59] Sando, D. *et al.* Revisiting the Optical Band Gap in Epitaxial $BiFeO_3$ Thin Films. *Advanced Optical Materials* **6,** 1700836 (2018).

[60] Pintilie, L. & Alexe, M. Metal-ferroelectric-metal heterostructures with Schottky contacts. I. Influence of the ferroelectric properties. *Journal of Applied Physics* **98,** 124103 (2005).

[61] Sze, S. M. & Ng, K. K. *Physics of semiconductor devices* (John Wiley & sons, 2006).

[62] Lee, J. H. *et al.* A strong ferroelectric ferromagnet created by means of spin–lattice coupling. *Nature* **466,** 954 (2010).

[63] He, Q. *et al.* Electrically controllable spontaneous magnetism in nanoscale mixed phase multiferroics. *Nature Communications* **2,** 225 (2011).

[64] Zhang, L. *et al.* Giant polarization in super-tetragonal thin films through interphase strain. *Science* **361,** 494–497 (2018).

[65] Yang, C.-H., Kan, D., Takeuchi, I., Nagarajan, V. & Seidel, J. Doping $BiFeO_3$: approaches and enhanced functionality. *Physical Chemistry Chemical Physics* **14,** 15953–15962 (2012).

[66] Bassiri-Gharb, N. *et al.* Domain wall contributions to the properties of piezoelectric thin films. *Journal of Electroceramics* **19,** 49–67 (2007).

[67] Jones, J. L., Hoffman, M., Daniels, J. E. & Studer, A. J. Direct measurement of the domain switching contribution to the dynamic piezoelectric response in ferroelectric ceramics. *Applied Physics Letters* **89,** 092901 (2006).

[68] Hall, D. Review nonlinearity in piezoelectric ceramics. *Journal of Materials Science* **36,** 4575–4601 (2001).

[69] Ascher, E., Rieder, H., Schmid, H. & Stössel, H. Some Properties of Ferromagnetoelectric Nickel-Iodine Boracite, Ni3B7O13I. *Journal of Applied Physics* **37,** 1404–1405 (1966).

[70] Aird, A. & Salje, E. K. Sheet superconductivity in twin walls: experimental evidence of. *Journal of Physics: Condensed Matter* **10,** L377 (1998).

[71] Rojac, T. *et al.* Domain-wall conduction in ferroelectric $BiFeO_3$ controlled by accumulation of charged defects. *Nature Materials* **16,** 322+ (2017).

[72] Zavaliche, F. *et al.* Polarization switching in epitaxial $BiFeO_3$ films. *Applied Physics Letters* **87,** 252902 (2005).

[73] Chu, Y.-H. *et al.* Electric-field control of local ferromagnetism using a magnetoelectric multiferroic. *Nature Materials* **7,** 478 (2008).

[74] Velez, J. H. *et al.* Fabrication Parameter Optimization for a Multilayer Photovoltaic Cell Based on the Heterojunction: Zinc (II)-Meso-Tetrakis (4-Bromophenyl) Porphyrins/Fullerenes. *Open Journal of Applied Sciences* **3,** 136 (2013).

[75] Yang, M.-M., Luo, Z.-D., Kim, D. J. & Alexe, M. Bulk photovoltaic effect in monodomain $BiFeO_3$ thin films. *Applied Physics Letters* **110,** 183902 (2017).

[76] Kim, D. *et al.* Polarization relaxation induced by a depolarization field in ultrathin ferroelectric $BaTiO_3$ capacitors. *Physical Review Letters* **95,** 237602 (2005).

[77] Bhatnagar, A. *Electronic and photoelectronic processes in multiferroic materials* 2014.

[78] Yang, M. *Photoelectric processes in ferroelectric/multiferroic materials* PhD thesis (University of Warwick, 2018).

[79] Binnig, G., Quate, C. F. & Gerber, C. Atomic force microscope. *Physical Review Letters* **56,** 930 (1986).

[80] Binnig, G., Gerber, C., Stoll, E., Albrecht, T. & Quate, C. Atomic resolution with atomic force microscope. *EPL (Europhysics Letters)* **3,** 1281 (1987).

[81] Leatherman, G. *et al.* Carotene as a molecular wire: Conducting atomic force microscopy. *The Journal of Physical Chemistry B* **103,** 4006–4010 (1999).

[82] Martin, Y., Abraham, D. W. & Wickramasinghe, H. K. High-resolution capacitance measurement and potentiometry by force microscopy. *Applied Physics Letters* **52,** 1103–1105 (1988).

[83] Maivald, P. *et al.* Using force modulation to image surface elasticities with the atomic force microscope. *Nanotechnology* **2,** 103 (1991).

[84] Saenz, J. *et al.* Observation of magnetic forces by the atomic force microscope. *Journal of Applied Physics* **62,** 4293–4295 (1987).

[85] Soergel, E. Piezoresponse force microscopy (PFM). *Journal of Physics D: Applied Physics* **44,** 464003 (2011).

[86] Zavaliche, F. *et al.* Multiferroic $BiFeO_3$ films: domain structure and polarization dynamics. *Phase Transitions* **79,** 991–1017 (2006).

[87] Zavaliche, F. *et al.* Ferroelectric domain structure in epitaxial $BiFeO_3$ films. *Applied Physics Letters* **87,** 182912 (2005).

[88] Kholkin, A., Kalinin, S., Roelofs, A. & Gruverman, A. in *Scanning Probe Microscopy* 173–214 (Springer, 2007).

[89] Borderon, C., Renoud, R., Ragheb, M. & Gundel, H. Description of the low field nonlinear dielectric properties of ferroelectric and multiferroic materials. *Applied Physics Letters* **98,** 112903 (2011).

[90] Boser, O. Statistical theory of hysteresis in ferroelectric materials. *Journal of Applied Physics* **62,** 1344–1348 (1987).

[91] Fewster, P. F. *X-ray Scattering from Semiconductors* (World Scientific, 2000).

[92] Béa, H. *et al.* Influence of parasitic phases on the properties of $BiFeO_3$ epitaxial thin films. *Applied Physics Letters* **87,** 072508 (2005).

[93] Dedon, L. R. *et al.* Nonstoichiometry, structure, and properties of $BiFeO_3$ films. *Chemistry of Materials* **28,** 5952–5961 (2016).

[94] Folkman, C. *et al.* Stripe domain structure in epitaxial (001) $BiFeO_3$ thin films on orthorhombic $TbScO_3$ substrate. *Applied Physics Letters* **94,** 251911 (2009).

[95] Kwamen, C. L. T. *Investigating the dynamics of polarization reversal in ferroelectric thin films by time-resolved X-ray diffraction* PhD thesis (University of Potsdam, 2019).

[96] Navirian, H. *et al.* Synchrotron-based ultrafast x-ray diffraction at high repetition rates. *Review of Scientific Instruments* **83,** 063303 (2012).

[97] Kriegner, D. & Wintersberger, E. *xrayutilities: python library* [Online; accessed <10/08/2019>]. 2019.

[98] Newville, M., Stensitzki, T. *et al. Non-Linear Least-Squares Minimization and Curve-Fitting for Python: python library* [Online; accessed <10/08/2019>]. 2019.

[99] Riedl, T. 2019.

[100] Pennycook, S. J., David, B., Williams, C. B. *et al.* Transmission electron microscopy: a textbook for materials science. *Microscopy and Microanalysis* **16,** 111 (2010).

[101] Peters, J. J., Apachitei, G., Beanland, R., Alexe, M. & Sanchez, A. M. Polarization curling and flux closures in multiferroic tunnel junctions. *Nature Communications* **7,** 13484 (2016).

[102] Li, L. *et al.* Atomic scale structure changes induced by charged domain walls in ferroelectric materials. *Nano Letters* **13,** 5218–5223 (2013).

[103] Peters, J. *Strain++* [Online; accessed <10/08/2019>]. 2019.

[104] Giannuzzi, L. A. *et al. Introduction to focused ion beams: instrumentation, theory, techniques and practice* (Springer Science & Business Media, 2004).

[105] Kawasaki, M. *et al.* Atomic control of $SrTiO_3$ surface for perfect epitaxy of perovskite oxides. *Applied Surface Science* **107,** 102–106 (1996).

[106] Koster, G., Kropman, B. L., Rijnders, G. J., Blank, D. H. & Rogalla, H. Quasi-ideal strontium titanate crystal surfaces through formation of strontium hydroxide. *Applied Physics Letters* **73,** 2920–2922 (1998).

[107] Koster, G., Rijnders, G., Blank, D. H. & Rogalla, H. Surface morphology determined by (001) single-crystal $SrTiO_3$ termination. *Physica C: Superconductivity* **339,** 215–230 (2000).

[108] Dirsyte, R. *et al.* Thermal-induced change in surface termination of $DyScO_3$(110). *Surface Science* **604,** L55–L58 (2010).

[109] Schwarzkopf, J., Braun, D., Hanke, M., Uecker, R. & Schmidbauer, M. Strain Engineering of Ferroelectric Domains in $K_xNa_{1-x}NbO_3$ Epitaxial Layers. *Frontiers in Materials* **4,** 26 (2017).

[110] Johann, F., Morelli, A., Biggemann, D., Arredondo, M. & Vrejoiu, I. Epitaxial strain and electric boundary condition effects on the structural and ferroelectric properties of $BiFeO_3$ films. *Physical Review B* **84,** 094105 (2011).

[111] Kleibeuker, J. E. *et al.* Atomically Defined Rare-Earth Scandate Crystal Surfaces. *Advanced Functional Materials* **20,** 3490–3496 (2010).

[112] Kleibeuker, J. *et al.* Structure of singly terminated polar $DyScO_3$ (110) surfaces. *Physical Review B* **85,** 165413 (2012).

[113] Fujino, S. *et al.* Ferroelectric properties of multiphase Bi–Fe–O thin films. *Solid State Ionics* **178,** 1257–1261 (2007).

[114] Toupet, H. *et al.* Growth and thermal stability of epitaxial $BiFeO_3$ thin films. *Journal of Magnetism and Magnetic Materials* **321,** 1702–1705 (2009).

[115] Guo, R. *et al.* Influence of target composition and deposition temperature on the domain structure of $BiFeO_3$ thin films. *AIP Advances* **2,** 042104 (2012).

[116] Jaber, N. *et al.* Laser fluence and spot size effect on compositional and structural properties of $BiFeO_3$ thin films grown by Pulsed Laser Deposition. *Thin Solid Films* **634,** 107–111 (2017).

[117] Yun, Y., Ramakrishnegowda, N., Park, D.-S. & Bhatnagar, A. Long range ordering of 71 degree domain walls in epitaxial $BiFeO_3$ thin films. *Applied Physics Letters* **113,** 042901 (2018).

[118] Jiang, Z.-Z. *et al.* Epitaxial growth of $BiFeO_3$ films on $SrRuO_3/SrTiO_3$. *Materials Characterization* **131,** 217–223 (2017).

[119] Sando, D. personal communication.

[120] Bea, H. *et al.* Unravelling the origin of the controversial magnetic properties of $BiFeO_3$ thin films. *arXiv preprint cond-mat/0606441* (2006).

[121] Domingo, N., Farokhipoor, S., Santiso, J., Noheda, B. & Catalan, G. Domain wall magnetoresistance in $BiFeO_3$ thin films measured by scanning probe microscopy. *Journal of Physics: Condensed Matter* **29,** 334003 (2017).

[122] Yang, M.-M., Bhatnagar, A., Luo, Z.-D. & Alexe, M. Enhancement of local photovoltaic current at ferroelectric domain walls in $BiFeO_3$. *Scientific Reports* **7,** 43070 (2017).

[123] Li, M. *et al.* Controlling resistance switching polarities of epitaxial $BaTiO_3$ films by mediation of ferroelectricity and oxygen vacancies. *Advanced Electronic Materials* **1,** 1500069 (2015).

[124] Hong, W. *et al.* Persistent step-flow growth of strained films on vicinal substrates. *Physical Review Letters* **95,** 095501 (2005).

[125] Weber, D., Vőfély, R., Chen, Y., Mourzina, Y. & Poppe, U. Variable resistor made by repeated steps of epitaxial deposition and lithographic structuring of oxide layers by using wet chemical etchants. *Thin Solid Films* **533,** 43–47 (2013).

[126] Garcia, J. *et al.* Evaluation of domain wall motion in lead zirconate titanate ceramics by nonlinear response measurements. *Journal of Applied Physics* **103,** 054108 (2008).

[127] Bolten, D., Böttger, U. & Waser, R. Reversible and irreversible piezoelectric and ferroelectric response in ferroelectric ceramics and thin films. *Journal of the European Ceramic Society* **24,** 725–732 (2004).

[128] Eitel, R., Shrout, T. & Randall, C. Nonlinear contributions to the dielectric permittivity and converse piezoelectric coefficient in piezoelectric ceramics. *Journal of Applied Physics* **99,** 124110 (2006).

[129] Trolier-McKinstry, S., Bassiri Gharb, N. & Damjanovic, D. Piezoelectric nonlinearity due to motion of 180 degree domain walls in ferroelectric materials at subcoercive fields: a dynamic poling model. *Applied Physics Letters* **88,** 202901 (2006).

[130] Li, X. *et al.* Domain Wall Motion in Perovskite Ferroelectrics Studied by the Nudged Elastic Band Method. *The Journal of Physical Chemistry C* **122,** 3091–3100 (2018).

[131] Vrejoiu, I. *et al.* Intrinsic ferroelectric properties of strained tetragonal $PbZr_{0.2}Ti_{0.8}O_3$ obtained on layer–by–layer grown, defect–free single–crystalline films. *Advanced Materials* **18,** 1657–1661 (2006).

[132] Morioka, H., Yokoyama, S., Oikawa, T., Funakubo, H. & Saito, K. Spontaneous polarization change with Zr/(Zr+Ti) ratios in perfectly polar-axis-orientated epitaxial tetragonal $Pb(Zr,Ti)O_3$ films. *Applied Physics Letters* **85,** 3516–3518 (2004).

[133] Nagarajan, V. *et al.* Size effects in ultrathin epitaxial ferroelectric heterostructures. *Applied Physics Letters* **84,** 5225–5227 (2004).

[134] Pintilie, L., Vrejoiu, I., Hesse, D., LeRhun, G. & Alexe, M. Structure, structural phase transitions, mechanical properties, defects-Ferroelectric polarization-leakage current relation in high quality epitaxial $Pb(Zr,Ti)O_3$ films. *Physical Review-Section B-Condensed Matter* **75,** 104103–104103 (2007).

[135] Taylor, D. & Damjanovic, D. Evidence of domain wall contribution to the dielectric permittivity in PZT thin films at sub-switching fields. *Journal of Applied Physics* **82,** 1973–1975 (1997).

[136] Taylor, D., Damjanovic, D., Colla, E. & Setter, N. Fatigue and nonlinear dielectric response in sol-gel derived lead zirconate titanate thin films. *Ferroelectrics* **225,** 91–97 (1999).

[137] Bharadwaja, S., Damjanovic, D. & Setter, N. Analysis of the non linear domain wall response in ferroelectric thin films. *Ferroelectrics* **303,** 59–63 (2004).

[138] Damjanovic, D. Ferroelectric, dielectric and piezoelectric properties of ferroelectric thin films and ceramics. *Reports on Progress in Physics* **61,** 1267 (1998).

[139] Nadaud, K., Borderon, C., Renoud, R. & Gundel, H. W. Decomposition of the different contributions to permittivity, losses, and tunability in $BaSrTiO_3$ thin films using the hyperbolic law. *Journal of Applied Physics* **119,** 114101 (2016).

[140] Xu, F. *et al.* Domain wall motion and its contribution to the dielectric and piezoelectric properties of lead zirconate titanate films. *Journal of Applied Physics* **89,** 1336–1348 (2001).

[141] Jonscher, A. K. Dielectric relaxation in solids. *Journal of Physics D: Applied Physics* **32,** R57 (1999).

[142] Nadaud, K., Borderon, C., Renoud, R. & Gundel, H. W. Effect of manganese doping of $BaSrTiO_3$ on diffusion and domain wall pinning. *Journal of Applied Physics* **117,** 084104 (2015).

[143] Kartawidjaja, F., Sim, C. & Wang, J. Heterolayered PZT thin films of different thicknesses and stacking sequence. *Journal of Materials Science* **44,** 5375–5382 (2009).

[144] Lou, X. *et al.* Effect of polarization fatigue on the Rayleigh coefficients of ferroelectric lead zirconate titanate thin films: Experimental evidence and implications. *Applied Physics Letters* **105,** 102907 (2014).

[145] Garcia, J., Pérez, R. & Albareda, A. Contribution of reversible processes to the non-linear dielectric response in hard lead zirconate titanate ceramics. *Journal of Physics: Condensed Matter* **17,** 7143 (2005).

[146] Garcia, J., Pérez, R., Albareda, A. & Eiras, J. Non-linear dielectric and piezoelectric response in undoped and Nb5+ or Fe3+ doped PZT ceramic system. *Journal of the European Ceramic Society* **27,** 4029–4032 (2007).

[147] Merz, W. J. Domain Formation and Domain Wall Motions in Ferroelectric $BaTiO_3$ Single Crystals. *Physical Review* **95,** 690 (1954).

[148] Tybell, T., Paruch, P., Giamarchi, T. & Triscone, J.-M. Domain Wall Creep in Epitaxial Ferroelectric $Pb(Zr_{0.2}Ti_{0.8})O_3$ Thin Films. *Physical Review Letters* **89,** 097601 (2002).

[149] Shin, Y.-H., Grinberg, I., Chen, I.-W. & Rappe, A. M. Nucleation and growth mechanism of ferroelectric domain-wall motion. *Nature* **449,** 881 (2007).

[150] Meyer, B. & Vanderbilt, D. Ab initio study of ferroelectric domain walls in $PbTiO_3$. *Physical Review B* **65,** 104111 (2002).

[151] Nelson, C. T. *et al.* Domain dynamics during ferroelectric switching. *Science* **334,** 968–971 (2011).

[152] Gao, P. *et al.* Direct observations of retention failure in ferroelectric memories. *Advanced Materials* **24,** 1106–1110 (2012).

[153] Hong, L., Soh, A., Du, Q. & Li, J. Interaction of O vacancies and domain structures in single crystal $BaTiO_3$: Two-dimensional ferroelectric model. *Physical Review B* **77,** 094104 (2008).

[154] He, L. & Vanderbilt, D. First-principles study of oxygen-vacancy pinning of domain walls in $PbTiO_3$. *Physical Review B* **68,** 134103 (2003).

[155] Duiker, H. *et al.* Fatigue and switching in ferroelectric memories: Theory and experiment. *Journal of Applied Physics* **68,** 5783–5791 (1990).

[156] Brennan, C. Model of ferroelectric fatigue due to defect/domain interactions. *Ferroelectrics* **150,** 199–208 (1993).

[157] Chandrasekaran, A., Damjanovic, D., Setter, N. & Marzari, N. Defect ordering and defect–domain-wall interactions in $PbTiO_3$: A first-principles study. *Physical Review B* **88,** 214116 (2013).

[158] Sharma, P. *et al.* Nonvolatile ferroelectric domain wall memory. *Science Advances* **3** (2017).

[159] He, Q. *et al.* Magnetotransport at Domain Walls in $BiFeO_3$. *Physical Review Letters* **108** (2012).

[160] Lee, J. H. *et al.* Spintronic Functionality of $BiFeO_3$ Domain Walls. *Advanced Materials* **26,** 7078+ (2014).

[161] Baek, S. *et al.* Ferroelastic switching for nanoscale non-volatile magnetoelectric devices. *Nature Materials* **9,** 309 (2010).

[162] Baek, S.-H. *et al.* The nature of polarization fatigue in $BiFeO_3$. *Advanced Materials* **23,** 1621–1625 (2011).

[163] Yang, S. *et al.* Electric Field Writing of Ferroelectric Nano-Domains Near 71 degrees Domain Walls with Switchable Interfacial Conductivity. *Annalen der Physik* **530** (2018).

[164] Johann, F., Morelli, A. & Vrejoiu, I. Stability of 71 degrees stripe domains in epitaxial $BiFeO_3$ films upon repeated electrical switching. *Physica Status Solidi B* **249,** 2278–2286 (2012).

[165] Johann, F. Control of ferroelectric domains in epitaxial $BiFeO_3$ thin films and submicron structures (2013).

[166] Wang, Y. *et al.* $BiFeO_3$ domain wall energies and structures: a combined experimental and density functional theory+ U study. *Physical Review Letters* **110,** 267601 (2013).

[167] Martin, L. W. *et al.* Nanoscale control of exchange bias with $BiFeO_3$ thin films. *Nano Letters* **8,** 2050–2055 (2008).

[168] Gareeva, Z., Diéguez, O., Íñiguez, J. & Zvezdin, A. K. Complex domain walls in $BiFeO_3$. *Physical Review B* **91,** 060404 (2015).

[169] Fatuzzo, E. Theoretical considerations on the switching transient in ferroelectrics. *Physical Review* **127,** 1999 (1962).

[170] Scott, J. A review of ferroelectric switching. *Ferroelectrics* **503,** 117–132 (2016).

[171] Tagantsev, A. K., Stolichnov, I., Setter, N., Cross, J. S. & Tsukada, M. Non-Kolmogorov-Avrami switching kinetics in ferroelectric thin films. *Physical Review B* **66,** 214109 (2002).

[172] Scott, J. *et al.* Switching kinetics of lead zirconate titanate submicron thin-film memories. *Journal of Applied Physics* **64,** 787–792 (1988).

[173] Grigoriev, A. *et al.* Nanosecond domain wall dynamics in ferroelectric $Pb(Zr,Ti)O_3$ thin films. *Physical Review Letters* **96,** 187601 (2006).

[174] Kwamen, C. *et al.* Simultaneous dynamic characterization of charge and structural motion during ferroelectric switching. *Physical Review B* **96,** 134105 (2017).

[175] Kwamen, C., Rössle, M., Leitenberger, W., Alexe, M. & Bargheer, M. Time-resolved X-ray diffraction study of the structural dynamics in an epitaxial ferroelectric thin $Pb(Zr_{0.2}Ti_{0.8})O_3$ film induced by sub-coercive fields. *Applied Physics Letters* **114,** 162907 (2019).

[176] Lee, J. T., Damodaran, A., Ramesh, R., Martin, L. & Abbamonte, P. X-ray diffraction studies of stripelike ferroelectric domains in thin films of $BiFeO_3$. *Physical Review B* **89,** 214104 (2014).

[177] Kawae, T., Terauchi, Y., Tsuda, H., Kumeda, M. & Morimoto, A. Improved leakage and ferroelectric properties of Mn and Ti codoped $BiFeO_3$ thin films. *Applied Physics Letters* **94,** 112904 (2009).

[178] Baek, S. H. & Eom, C. B. Reliable polarization switching of $BiFeO_3$. *Philosophical Transactions of the Royal Society A: Mathematical, Physical and Engineering Sciences* **370,** 4872–4889 (2012).

[179] Marton, P., Rychetsky, I. & Hlinka, J. Domain walls of ferroelectric $BaTiO_3$ within the Ginzburg-Landau-Devonshire phenomenological model. *Physical Review B* **81,** 144125 (2010).

[180] Li, M., Gu, Y., Wang, Y., Chen, L.-Q. & Duan, W. First-principles study of 180 degree domain walls in $BaTiO_3$: Mixed Bloch-Néel-Ising character. *Physical Review B* **90,** 054106 (2014).

[181] Do, D.-H. *et al.* In situ X-ray probes for piezoelectricity in epitaxial ferroelectric capacitors. *Integrated Ferroelectrics* **101,** 174–181 (2008).

[182] Damjanovic, D. Stress and frequency dependence of the direct piezoelectric effect in ferroelectric ceramics. *Journal of Applied Physics* **82,** 1788–1797 (1997).

[183] Grigoriev, A. *et al.* Nonlinear piezoelectricity in epitaxial ferroelectrics at high electric fields. *Physical Review Letters* **100,** 027604 (2008).

[184] Gorfman, S. *et al.* Simultaneous resonant x-ray diffraction measurement of polarization inversion and lattice strain in polycrystalline ferroelectrics. *Scientific Reports* **6,** 20829 (2016).

[185] Shin, Y. *et al.* Suppression of creep-regime dynamics in epitaxial ferroelectric $BiFeO_3$ films. *Scientific Reports* **5,** 10485 (2015).

[186] Jo, J. Y. *et al.* Nonlinear dynamics of domain-wall propagation in epitaxial ferroelectric thin films. *Physical Review Letters* **102,** 045701 (2009).

[187] Li, J. *et al.* Ultrafast polarization switching in thin-film ferroelectrics. *Applied Physics Letters* **84,** 1174–1176 (2004).

[188] Fahy, S. & Merlin, R. Reversal of ferroelectric domains by ultrashort optical pulses. *Physical Review Letters* **73,** 1122 (1994).

[189] Mankowsky, R., von Hoegen, A., Först, M. & Cavalleri, A. Ultrafast reversal of the ferroelectric polarization. *Physical Review Letters* **118,** 197601 (2017).

[190] Schick, D. *et al.* Ultrafast lattice response of photoexcited thin films studied by X-ray diffraction. *Structural Dynamics* **1,** 064501 (2014).

[191] Yang, Y., Ren, W., Stengel, M., Yan, X. & Bellaiche, L. Revisiting properties of ferroelectric and multiferroic thin films under tensile strain from first principles. *Physical Review Letters* **109,** 057602 (2012).

[192] Fan, Z. *et al.* Structural instability of epitaxial (001) $BiFeO_3$ thin films under tensile strain. *Scientific Reports* **4,** 4631 (2014).

[193] Liu, Y., Yang, L. & Li, J. Strain-engineered orthorhombic-rhombohedral phase boundary in epitaxial bismuth ferrite films. *Journal of Applied Physics* **113,** 183524 (2013).

[194] Dupé, B., Prosandeev, S., Geneste, G., Dkhil, B. & Bellaiche, L. $BiFeO_3$ films under tensile epitaxial strain from first principles. *Physical Review Letters* **106,** 237601 (2011).

[195] Chen, Z. *et al.* Large tensile-strain-induced monoclinic M_B phase in $BiFeO_3$ epitaxial thin films on a $PrScO_3$ substrate. *Physical Review B* **88,** 054114 (2013).

[196] Sando, D. *et al.* Large elasto-optic effect and reversible electrochromism in multiferroic $BiFeO_3$. *Nature Communications* **7,** 10718 (2016).

[197] Yang, J.-C. *et al.* Orthorhombic $BiFeO_3$. *Physical Review Letters* **109,** 247606 (2012).

[198] Yang, J.-C. *et al.* Conduction control at ferroic domain walls via external stimuli. *Nanoscale* **6,** 10524–10529 (2014).

[199] Heo, Y. *et al.* Enhanced conductivity at orthorhombic–rhombohedral phase boundaries in $BiFeO_3$ thin films. *NPG Asia Materials* **8,** 297 (2016).

[200] Geng, W. *et al.* Rhombohedral–Orthorhombic Ferroelectric Morphotropic Phase Boundary Associated with a Polar Vortex in $BiFeO_3$ Films. *ACS Nano* **12,** 11098–11105 (2018).

[201] Sando, D., Xu, B., Bellaiche, L. & Nagarajan, V. A multiferroic on the brink: Uncovering the nuances of strain-induced transitions in $BiFeO_3$. *Applied Physics Reviews* **3,** 011106 (2016).

[202] Gebhardt, U. *et al.* Formation and Thickness Evolution of Periodic Twin Domains in Manganite Films Grown on $SrTiO_3$ (001) Substrates. *Physical Review Letters* **98,** 096101 (2007).

[203] Vanderbilt, D. & Cohen, M. H. Monoclinic and triclinic phases in higher-order Devonshire theory. *Physical Review B* **63,** 094108 (2001).

[204] You, L. *et al.* Enhancing ferroelectric photovoltaic effect by polar order engineering. *Science Advances* **4,** eaat3438 (2018).

[205] Wang, W.-Y. *et al.* Atomic mapping of structural distortions in 109 degree domain patterned $BiFeO_3$ thin films. *Journal of Materials Research* **32,** 2423–2430 (2017).

[206] Borisevich, A. Y. *et al.* Suppression of octahedral tilts and associated changes in electronic properties at epitaxial oxide heterostructure interfaces. *Physical Review Letters* **105,** 087204 (2010).

[207] Kim, Y.-M. *et al.* Direct observation of ferroelectric field effect and vacancy-controlled screening at the $BiFeO_3/La_xSr_{1-x}MnO_3$ interface. *Nature Materials* **13,** 1019 (2014).

[208] Huang, R. *et al.* Atomic-Scale Visualization of Polarization Pinning and Relaxation at Coherent $BiFeO_3$/$LaAlO_3$ Interfaces. *Advanced Functional Materials* **24,** 793–799 (2014).

[209] Bhatnagar, A., Chaudhuri, A. R., Kim, Y. H., Hesse, D. & Alexe, M. Role of domain walls in the abnormal photovoltaic effect in $BiFeO_3$. *Nature Communications* **4,** 2835 (2013).

[210] Fridkin, V. M. *Photoferroelectrics* (Springer Science & Business Media, 2012).

[211] Li, P., Dong, X., Gao, Y., Ren, L. & Jin, K. Photocarrier transport and dynamics in mixed-phase $BiFeO_3$ films. *Optics Express* **24,** 9119–9129 (2016).

[212] Damodaran, A. R., Lee, S., Karthik, J., MacLaren, S. & Martin, L. W. Temperature and thickness evolution and epitaxial breakdown in highly strained $BiFeO_3$ thin films. *Physical Review B* **85,** 024113 (2012).

[213] Catalan, G. & Scott, J. F. Physics and applications of bismuth ferrite. *Advanced Materials* **21,** 2463–2485 (2009).

[214] Yang, M.-M., Iqbal, A. N., Peters, J. J., Sanchez, A. M. & Alexe, M. Strain-gradient mediated local conduction in strained bismuth ferrite films. *Nature Communications* **10,** 2791 (2019).